

REU AT MINNESOTA



June 5-August 11, 2006

Proceedings of the Summer 2006 University of Minnesota
Physics Research Experiences for Undergraduates

School of Physics and Astronomy
University of Minnesota
Minneapolis, MN 55455

www.physics.umn.edu/outreach/reu



It is once again a great pleasure to issue this, the fourth in a series of proceedings of the University of Minnesota Physics Research Experiences for Undergraduates.

This program was made possible in the summer of 2006 by the support of the National Science Foundation under grant NSF/PHY-0139099, and by the support of the University of Minnesota.

The research projects summarized here span a wide range of topics, reflecting the breadth of interests represented within the School of Physics and Astronomy: From observational astronomy and cosmology, including space and planetary physics, through biophysics, condensed matter physics, astroparticle and high energy physics, all of the proposed investigations were chosen for their immediate interest and accessibility to the participants of the program.

The research performed over the summer often leads to published journal articles: Andrew Larkoski's theoretical investigation of quantum mechanics in extra dimensions has already appeared in extended form on the arXiv as hep-th/0610218.

We are very grateful to all participants for their enthusiasm, and to all of those who contributed their time and expertise to the success of the program.

Serge Rudaz
Professor of Physics and Director of Undergraduate Studies

Kenneth Heller
Professor and Associate Head of Physics

For more information regarding the REU program at the University of Minnesota, please visit our website at
<http://www.physics.umn.edu/outreach/reu/>

The research reported herein was supported by NSF grant NSF/PHY-0139099.

TABLE OF CONTENTS

Biomimetics & Evolution	1
Nicholas apRoberts-Warren, Wheaton College, Norton, MA	
Advisor: Professor Vincent Noireaux	
EBX: The E and B Experiment, Detecting Polarization modes	9
in the Cosmic Microwave Background	
Elizabeth A. Beckel, Colorado College, Colorado Spring, CO	
Advisor: Professor Shaul Hanany	
Mapping the Asymmetry of the Milky Way:.....	19
CCD Imaging and Star Counts	
Laura A. Broaded, Butler University, Indianapolis, IN	
Advisor: Dr. Roberta Humphreys	
An Analysis of CME-Magnetosphere Interactions	31
Jennifer Collier, Carthage College, Kenosha, WI	
Advisor: Professor John Wygant	
Supercontinuum Generation in Photonic Crystal Fibers	39
Sean Krzyzewski, Marquette University, Milwaukee, WI	
Advisor: Professor Joachim Mueller	
A Schrödinger Approach to Holography.....	49
Andrew Larkoski, University of Washington, Seattle, WA	
Advisors: Tony Gherghetta and Brian Battell	
Nuclear Recoil Band Definitions and CDMS Simulations	63
Katrina Legursky, Benedictine College, Atchison, KS	
Advisor: Professor Priscilla Cushman	
Looking for Signatures of Superconductivity in	
Laser-Processed Strontium Ruthenate	71
Gustav E. Rustan, University of Minnesota, Morris, MN	
Advisor: Dr. Allen Goldman	
Measuring Noble Gases in Coma Samples from Comet Wild 2	81
Jacob Simones, Minnesota State University, Mankato, MN	
Advisor: Dr. Russell Palma and Dr. Robert Pepin	

Table of Contents (cont.)

Research and Development of Magnetic tunnel Junctions	89
Jonathan Sperling, University of Wisconsin-Madison, Madison, WI	
Advisor: Professor E. Dan Dahlberg	
Neutrino Oscillations	101
Alexander Tenenbaum, Connecticut College, New London, CT	
Advisor: Professor Daniel Cronin-Hennessy	
Magnetic Reconnection and Its Effect on Earth's Aurora	111
Pamela Vo, Baylor University, Waco TX	
Advisor: Professor Cynthia Cattell	
Spin Ejection using External Cavity Tunable Diode Laser in Ferromagnet-Semiconductor Heterostructures	127
Claire Weiss, Lawrence University, Appleton, WI	
Advisor: Professor Paul Crowell	



Nicholas apRoberts-Waren

University of Minnesota 2006 Physics R.E.U.



Elizabeth Beckel



Laura Broaded



Jennifer Collier



Sean Krzyzewski



Andrew Larkoski



Katrina Legursky



Gustav Rustan



Jacob Simones



Jonathan Sperling



Alexander Tenenbaum



Pamela Vo



Claire Weiss

Biomimetics & Evolution

Undergraduate Student

Nicholas apRoberts-Warren
Wheaton College
Norton, MA

Advisor

Professor Vincent Noireaux
University of Minnesota
Minneapolis, MN

Biomimetics and Evolution

Nick apRoberts-Warren
Wheaton College, MA
Advisor: Professor Vincent Noireaux
UMN Physics REU 2006

We investigated the idea of using robotics as a conveyor of information – an imitation of DNA in cells. We started to build two different devices of approximately one centimeter scale and both using solar cells as a source of energy. Our first idea was to make a robot that can exhibit phototaxis; it can guide and propel itself along a gradient of light, and be power-independent. The second system was to see how a group of small, vibrating robots (approximating Brownian motion) will behave under a selection pressure. This involves in seeing if their bonding would be a positive or negative adaptation via the pressure.

I. Biomimetics & Evolution

Motivation

The idea of biomimetics is an old one – draw inspiration from the natural world. It has long been a part of human engineering and design, as many problems that come in modern design are problems that nature has itself addressed. To draw inspiration from such a source is understandable. Also, the forces of evolution have had many millions of years to respond to such pressures, so usually the solutions it presents are often inspired.

Examples

There are countless of examples of biomimetics in action. We can look in almost any area of engineering and see examples. In civil engineering, we dam up rivers in a style not dissimilar to beavers. In aeronautics, extendable flaps are inspired by the different shapes and inclinations of bird's wings. There is, of course, Velcro, the classic example of biomimetics imitating nature.

There is an issue of scale in these projects. Imitating biological engineering with inorganic substitutes is one thing, but can

we really imitate cellular life? The cell is an incredibly complex piece of machinery, it can self-reproduce, move, and adapt to a host of environmental changes.

Using Evolution

We can think of evolution via self-reproduction as the zenith of biomimetics – a system that will adapt itself through successive generations to whatever pressures are applied to it. Though we cannot yet build a self-reproducing synthetic, we can apply the ideas of survival-of-the-fittest to robotics and biomimetics and see how the emergent properties of our system respond to a selection pressure.

II. Our System

Examples

Chemotaxis refers to the behavioral response of an organism to the concentration of chemicals in its environment. This trait is evident all along the length and complexity of organisms. Humans are obviously able to navigate ourselves to food and away from poisons. Fish can detect fouled water. Even down to

microorganisms, such as E. Coli, whose genome is 600 times smaller than the human genome, can detect concentrations of glucose and navigate itself towards them and can flee high levels of carbolic acid.

While humans ambulate and fishes swim, bacteria have another interesting method of movement. It can be summed up in three movements: swim-tumble-swim. When spinning their flagella counter-clockwise, they “swim” forward. After some amount of time, they spin their flagella clockwise and let Brownian motion “tumble” them around to a new orientation, and then they swim again. Their movement closely resembles a random walk, the only difference being that E. Coli will swim in one direction for longer when it senses it is moving in the right direction.

a. DNA As Software

The DNA of an organism is more than just a blueprint to their construction - it provides the library of proteins and enzymes that keep an organism alive and functioning. We can think of the DNA as a library of response for the organism to access not only for its regular function, but also in situations of stress. This is especially evident in bacteria: very simple and self-contained organisms. E. Coli is one of the most understood and studied bacteria (4400 genes, and it is supposed that only about 400 are essential for reproduction) and we can use it as an example. When UV light grows too intense, E. Coli activates genes to increase its DNA repair rate. If salinity grows too low, then osmotic pressure is not balanced, E. Coli produces proteins designed to regulate the difference of osmotic pressure. We can see that DNA ends up functioning as the bacteria's software programming – stimulus and response. Since DNA can

mimic software, why can't software mimic DNA for robots?

b. Phototaxis

Chemotaxis is clearly a real-world example of common cell motility. We have decided to try and mimic a similar behavior. Phototaxis is the ability of an organism to guide itself along a gradient of light, either towards or away from the light source concentration. Light is a very useful quantity for taxis because of its ability to be easily sensed and converted into current via photovoltaics. It is also a very abundant and cheap power source to simulate, so it easily lends itself to this experiment.

III. The Experiments

Methodology

Our primary focus in both of these projects was to keep the size small; around the centimeter. We were investigating the basic functions of cell motility and cooperation, so the closer we could come to mimicking their size the better. We also want our designs, especially for the phototaxis robot, to be *scalable*.

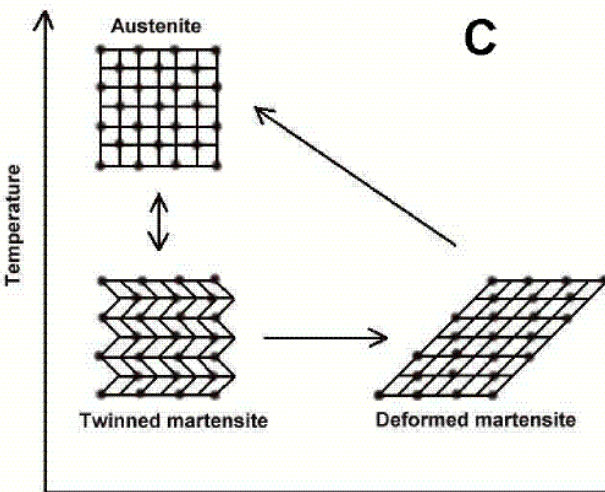
The last over-riding idea was that our experiments should mimic not only what was physical, but what was *biological* – real cell behavior.

Biomimetics

We first had to deal with the issue of size. Bacterial movement relies on Brownian motion to create the tumble part of the swim-tumble-swim cycle, and we couldn't get our size down to that size, so we would simply give the robot a steering- and navigation set-up.

After we set-up the size target, we considered various mechanisms for propulsion and sensing. We decided a

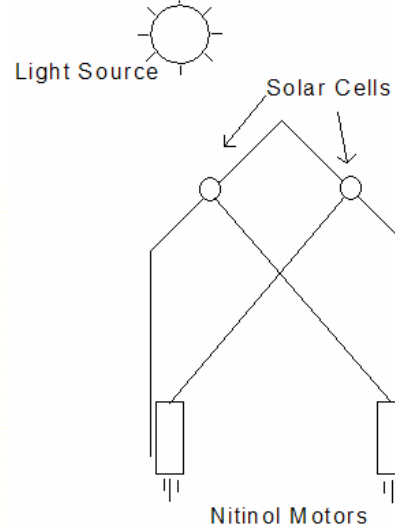
water medium would be best so as to reduce our friction and thus propulsion requirements. Our first idea was a negative-feedback loop using the memory shape alloy Nitinol¹.



The phase diagram of Nitinol with its two different phases
[<http://herkules.oulu.fi/isbn9514252217/html/x317.html>]

There have been other robots² made with Nitinol, as it is very useful for many engineering designs. In our case, the Nitinol would be attached to a flexible paddle, so when in the martensite phase, it would be flat along the paddle. Using the energy from solar cells placed around the motors, we would joule heat the Nitinol so that it would curl up into its austenite phase, and then would break the circuit. As it would relax back into its martensite phase, it would push the robot forward and then reconnect the circuit, starting the joule heating all over again.

We were very focused on having the power supply not be battery-based, and the idea of combining sensing and power supply into one circuit was very attractive.



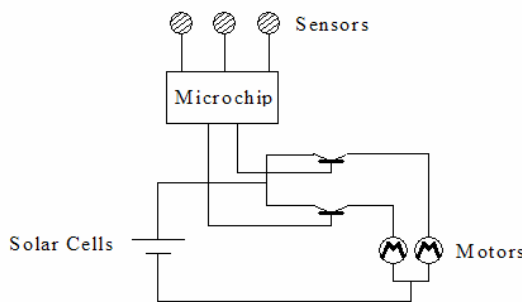
This way, the robot would always be reorienting itself towards the light by virtue of the difference in frequency of the joule heating, which leads to a larger propulsive push on that side. Unfortunately that idea turned out to have very high power demands, at least relative to what we could provide.

Using a 1 cm piece of 0.2 mm diameter Nitinol wire as an example, to heat it up from room temperature (~25 C) to its austenite phase (~60 C) in 1 one second would require on the order of 300 mA. Even allowing a 4 second response time, it would take 100 mA. Our solar cells can provide on the order of 30-40 mA, so we simply don't have the power to use Nitinol efficiently as a motor³.

We experimented with a couple of variants on the same idea, but ran into the same deficient power supply problem. So we decided to shelve that idea and try small motors.

With the solar cells we ended up deciding on (around 1.25 cm by 1.25 cm) from Silicon Solar. We tried many different cylindrical motors but settled on some from Jinlong Motors; they have a minimum starting current of ~20 ma, and the solar

cells could run them at decent speed. We now needed a sensor system to steer the robot.



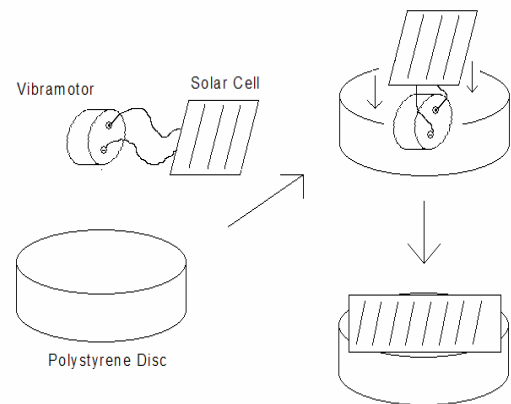
We decided to use a small MCU (microcontroller unit) to do the logic in evaluating the sensor data. The eventual choice was the PIC12CE673 made by Microchip⁴. It was picked because it had fairly low power requirements ($\sim 15 \mu\text{A}$), an internal Analog to Digital Converter (needed for reading sensor data), and relatively small size (8mm x 9.5 mm x 6mm). For the sensors, we will use solar cells from Hobby Engineering⁵ which are much smaller than the big solar cells used for power supply. Their output voltage varies on the strength of the received light, and the pins on the MCU can read voltage difference. Its program is a fairly simple Basic routine, weighing the converted voltage differences from the sensors, and turning on one or both of the available motors. There are many tutorials on how to create such a program using a PIC MCU⁶. We are programming it with a compiler and programmer bought from MicroEngineering Labs⁷. The way the code runs, it samples the voltages from the sensors, determines which motor to run, and then runs that motor for some pre-set amount of time. It then samples the voltages again. This is a recreation of the swim-tumble-swim method employed by E. Coli, though the random “tumble” is replaced by a more purposeful steering process.

Constructing the physical robot and wiring it will be a goal for the future.

Evolution

We wanted a simulation that would approximate a group of cells moving around randomly (vis a vis Brownian motion). This random motion would lead to association between the cells and would be positive – that is, help them to survive whatever selection pressure. The idea here was to imitate the way that prokaryotic cells started the process of symbiosis which led to our modern-day eukaryotic cells.

Approaching the evolution aspect, we knew that to simulate the selection there would need to be some avenue for the robots to “mutate”. For biological organisms, this mutation happens to their DNA and results in physical and behavioral changes in the next generation. Having no way to reproduce, the mutation would have to occur in the here-and-now. The easiest mutation would be something involving the only thing these robots could do at the moment – move. Their fairly random movement would be significantly altered by coupling with another robot, as their vibrational modes would severely interfere, hopefully creating a new movement pattern for the linked robots.



To mimic the random motion, we bought vibrator motors from Jinlong, much akin to the kind used in mobile phones for their

vibrate function. We embedded them in polystyrene discs with ~2.3 cm diameter and ~11 mm thickness. The motors were placed so that the plane of their vibration was normal to the surface they move on, with the 2 cm x 2 cm solar cells on top:



To create a powerful association between the robots, we glued very strong magnets from K & J Magnetics to the outside of the discs. Magnets were picked over Velcro, springs, and hook-loop-style bonding because the magnetic bond was very strong and rigid, which we needed in order for the association to alter the movement of the robots. Pliancy in the bond would absorb much the vibration from the robots, thereby canceling the coherent interference we had been hoping to see.

The “selection pressure” would need to choose for these bonded robots in such a fashion that they would garner a benefit from associating. At the time of this paper, no selection pressure has yet been settled upon.

IV. Discussion

Future Goals and Perspectives

Putting together the phototaxis robot will be the obvious next step. We only roughly outlined the architecture of the robot, so that will be an interesting design challenge

for the future. Another avenue of possible experimentation would be to make the code more complex and nuanced – different combinations of voltage sampling and swimming times could lead to pronounced differences in performance. There is still the idea of scalability, so future experiments could try to decrease the size of the robot, through more lower-energy propulsion and better quantum efficiency in the solar cells.

A future aspect would be to have a chip on the robots carrying some information relevant to their survival, and then the differences in that information would determine which robots would “survive”. Perhaps that code could even be rewritten by the robot, either purposefully or more like the random processes which alter biological DNA.

A selection pressure that would be viable would be to use the robot’s own Brownian-esque motion against. Setting up a sheet of polystyrene at a slight angle to the ground with no railings on the borders, the robots could be all (be) set at the same latitude on the sheet, and then released. The single robots would be at a disadvantage due to their random motion. Since a random walk will eventually touch every point in the plane, it’s significantly more likely that the single ‘bots will fall off the sides or fall down the slope of the sheet, thereby “losing”.

Conclusion

Though the work on the projects will continue past summer, we’ve shown how adapting robotics to imitate biological situations can give us a unique perspective on how organisms function and interact. Power supply for such small robotic system to have them autonomous can often be a large problem, should one desire to have an

independent system. In such projects, defining what “evolution” and “adaptation” is often half the battle, as this is a relatively new field.

This is just the beginning of exploring the idea of DNA as information, as cells as carriers of that information, and that this very basic building block of life can be mimicked with software and inorganic components.

Acknowledgements

I’d like to thank Dr. Vincent Noireaux and everyone in his lab for all their patience and instruction, and Serge Rudaz and Wendy Tschampl for coordinating and running an excellent REU. I’d also like to thank the University of Minnesota for hosting the REU and letting us into their labs. Lastly, I’d like to thank the NSF for funding this experience, in particular for grant no. NSF/PHY-0139099.

References

- [1] <http://herkules.oulu.fi/isbn9514252217.html/x317.html>
- [2] Young Pyo Lee, Byungkyu, Moon Gu Lee, Jong-Oh Park. “Locomotive Mechanism Design and Fabrication of Biomimetic Micro Robot Using Shape Memory Alloy”: 2004 IEEE, 5007-5012.
- [3] <http://www.tiniaerospace.com/sma.html>
- [4] www.microchip.com
- [5] <http://www.hobbyengineering.com/>
- [6] <http://www.rentron.com/pic.htm>
- [7] <http://www.melabs.com/>

EBEX: The E and B Experiment

Undergraduate Student

Elizabeth A. Beckel

Colorado College
Colorado Spring, CO

Advisor

Professor Shaul Hanany

University of Minnesota

Minneapolis, MN

EBEX: the E and B Experiment

Detecting Polarization modes in the Cosmic Microwave Background

Elizabeth A. Beckel

Colorado College, Colorado Spring CO

Advisor: Shaul Hanany

University of Minnesota, Minneapolis MN

Observing the Cosmic Microwave Background (CMB) radiation allows us to see over 13 billion years into the history of the universe. By studying the anisotropies in temperature and polarization, we can start to recreate some of the earliest moments in the universe. EBEX is a balloon-borne experiment to measure polarization of the CMB. EBEX will further our understanding of the epoch of inflation, during which the universe expanded exponentially for 10^{-33} second. Most importantly, EBEX may provide experimental confirmation of the inflationary paradigm. Additionally, EBEX will gather new and valuable information about galactic lensing, dust polarization, and cosmological parameters. I worked to model the cryostat and interior optical elements and performed impact testing to determine durability of adhesive greases. Results from each project will assist in preparation for device construction.

INTRODUCTION

EBEX is designed as a long duration balloon-borne experiment aimed to measure the polarization of the Cosmic Microwave Background radiation (CMB). With the use of a specially-designed telescope and optical equipment we hope to significantly increase our knowledge of the CMB and correspondingly, the universe in which we live. This experiment will work to better establish and further the results of the WMAP satellite mission [1] and others, and use the materials and knowledge from MAXIPOL, MAXIMA and APEX studies. Specifically, EBEX aims to detect the B-mode inflationary gravitational wave background signal, measure polarization of dust emission and other Galactic foreground, detect lensing of CMB polarization, and improve upon existing limits for several cosmological parameters. Although past projects have covered some similar research areas, EBEX will have unprecedented sensitivity as a CMB polarimeter, making it the first such instrument capable of detecting

the faint inflationary B-mode polarization signals.

EBEX has been funded since early 2004 and aims to fly late in 2008. The final design phase is currently underway and construction has begun. Preliminary design has been done with 3D-CAD model drawings, but as of June 2006, no physical models of the experiment's interior structure had been made. A physical model will be crucial for planning electrical wiring and support and for checking accuracy and feasibility of the cryostat design. I have constructed a scale model of the cryostat, as well as tested pieces of the experimental set-up for durability.

I will begin by giving an overview of the theory behind the EBEX experiment that will be necessary to understand the results and implications. I will then explain the workings of the cryostat set-up, telescope, and optics equipment, focusing on their relevance to my model construction. I will outline the experimental phase and flight

and describe my testing procedure and results. I will conclude by proposing some possible results and implications of the data.

THEORY

Big Bang theory outlines a relatively gradual expansion of space over time. Based on observations of the CMB, a new theory of accelerated expansion preceding the Big Bang expansion was introduced 25 years ago. Known as the epoch of inflation, it refers to a period during which space-time itself expanded faster than the speed of light (Figure 1).

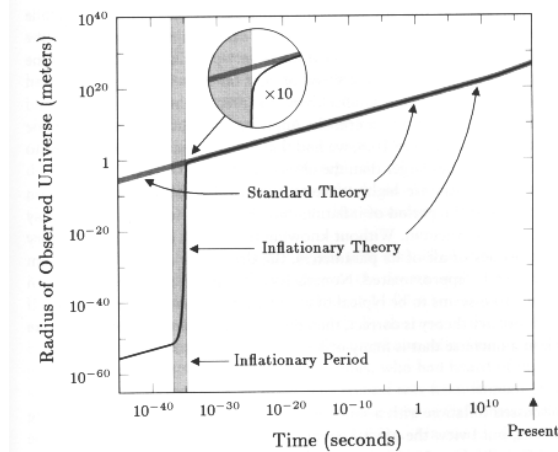


Figure 1: inflationary growth rate compared to standard theory of Big Bang inflation. [2]

The theory of inflation explains why the universe contains structure and appears flat (no over-all curvature) and isotropic. Presently there is no direct evidence that inflation occurred. During inflation, the fabric of space-time incurred “ripples” known as gravitational waves. Such waves should leave a signature on the polarization of the CMB.

13.7 billion years ago (± 0.2 billion years) the universe was an optically thick plasma of free protons and electrons. This immensely hot and dense universe was also

full of highly energetic photons, which, through collisions with any bonded atoms, maintained the ionized state of the particles. As the universe continued to expand and cool, the photons became less energetic, until they were no longer able to ionize hydrogen atoms. 300,000 years after the Big Bang, there were so few highly energetic photons that electrons could begin bonding, forming neutral hydrogen atoms. This period is known as the “epoch of recombination”. During this time, the universe became transparent, as it is today, marking the limit of our vision into the past. The photons scattering off of the last free electrons during the epoch of recombination traveled through the newly transparent universe, and after much continued expansion and redshifting, reach us today as the CMB. Because of the complete internal reflection before the epoch of recombination, the CMB spectrum is an almost perfect example of a blackbody.

In the four decades since the discovery of the CMB radiation, it has been recognized to hold an abundance of information concerning the origins and structure of our universe. By studying the anisotropies in temperature and polarization, researchers have gathered detailed information about the shape of the universe, dark matter, and early star and galaxy formation.[3] In recent studies, the focus has turned to the polarization modes of the CMB, and the differences between two types of polarization: the E-mode and B-mode.

Only a small fraction of the CMB is polarized. Thomson scattering of photons in an anisotropic radiation field caused linear polarization. Anisotropies in the early universe were created by both density fluctuations and gravity waves, though each of these would lead to different modes of polarization. While the curl-free E-mode

polarization was created by both density and gravitational fluctuation, curled B-mode polarization was produced only by gravity waves. This implies that if such B-mode polarization were to be observed, it would be a direct indication of gravity waves and therefore inflation.

A potential source of error and confusion is introduced by the fact that we cannot view the CMB as it was 13 billion years ago. It has traveled as many light years to reach us today, and in doing so has experienced numerous perturbations. When passing near large mass and energy structures, the CMB is distorted in a process known as gravitational lensing. Lensing will deflect the CMB in such a way as to create B-mode polarization where there was previously only E-mode signals. Lensing has been indicated in past experiments, but has been measured to only $\sim 20\%$ uncertainty [4], where, if current theories prove correct, EBEX will constrain the uncertainty in measurements to only 4%. [5] This lensing B-mode polarization should be separable from gravity wave induced B-modes in that the lensing polarization is most prominent in small angular scales ($\ell=1000, \Theta=0.18^\circ$) while gravitational wave B-modes peak at larger ($\ell=100, \Theta=1.8^\circ$) angular scales.

It is predicted that B-mode power scales are ~ 2 orders of magnitude more faint than those of E-mode polarization (Figure 2), making them difficult to detect in any ground based experiments due to atmospherically induced noise levels. At balloon levels (40,000m), however, atmospheric signals are 1000 times smaller, imposing only negligible interference for EBEX measurements.

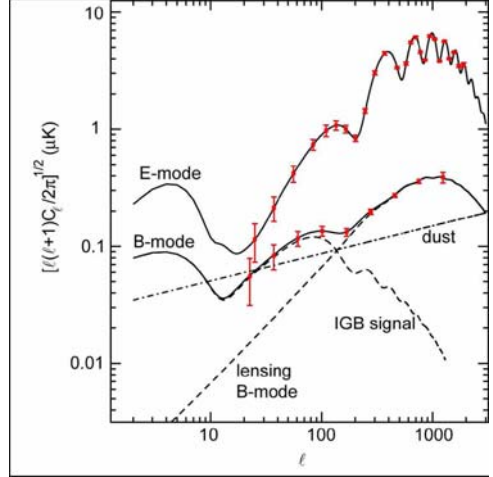


Figure 2: Angular power scale of E-mode and B-mode components of CMB radiation. E-mode has been measured in these regions, while B-mode power has only been theorized. Error bars indicate instrumental sensitivity.

$$\ell = \text{harmonic number} = 180/\Theta .$$

EBEX EXPERIMENTAL APPROACH

EBEX is planned to be flown in a long-duration high altitude balloon over Antarctica in December 2008. There it will circumnavigate the Antarctic continent by means of the circumpolar winds, a unique trait of the summer polar atmosphere. Average flight time is 14 days, during which EBEX will scan and gather data continuously. The main structure of the payload consists of a 1.5m optical telescope that will focus radiation into a cooled sensor array through a series of optical elements as shown in Figure 3. The detectors are designed to measure intensity and angle of the polarization in the CMB.

Upon reaching the EBEX telescope, the radiation will travel the following path: After being captured by the primary and secondary mirrors, radiation will be focused into the cryostat (Figure 4), the interior of which will be cooled to 4.2K by a pumped liquid helium tank layer. Radiation will

enter the cryostat through a series of thermal and low-pass filters, after which it will be focused downward through a field lens into an achromatic Half Wave Plate (HWP).

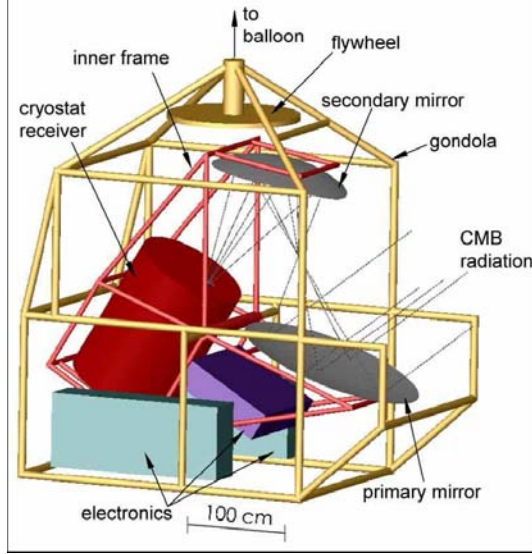


Figure 3: proposed EBEX construction. Gondola will attach equipment to the balloon.

The HWP will be positioned at the Lyot Stop in order to reduce stray radiation and will be coated with anti-reflective material to maximize transmitted radiation. The HWP has two different indices of refraction along orthogonal axes, causing alternate polarizations to move through the structure with differing velocities and creating a phase lag between opposing signals upon exiting the plate. The HWP is cut such that the vector component along the extraordinary axis will be shifted by 2Θ compared to the ordinary axis. The HWP will be connected to a motor causing it to rotate at a few Hz, creating a sinusoidal modulation of a known frequency in the linearly polarized radiation. This rotation will allow each detector to be an independent polarimeter, giving sufficient data to completely reconstruct incident polarization.

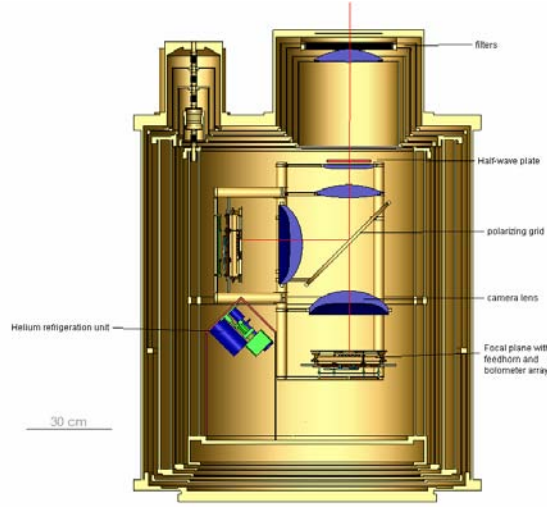


Figure 4: a cross sectional view of the cryostat interior. Lenses focus radiation onto the diagonal polarizing grid (center), which guides radiation to one of two focal planes and detector arrays. He-3 fridge (bottom-left) works to keep focal planes at a constant 300mK.

After being rotated and separated by the HWP, radiation will proceed through two pupil lenses onto a polarizing grid. The grid will contain a series of single-axis electrically conducting wires, making the grid act as a filter: polarization orthogonal to the grid passing straight through and polarization parallel to gridlines reflecting off at a 90° angle. The divided radiation will pass through telecentric camera lenses, which will focus the radiation onto a plane (Fig. 5). At the focal plane are feedhorns acting as a Faraday cage, isolating detector arrays from unwanted electromagnetic radiation.

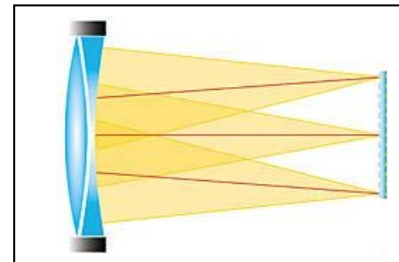


Figure 5: a telecentric camera lens focuses incident rays to come in perpendicular to the focal plane.

Each focal plane will contain approximately 900 feedhorns, each leading to an individual bolometer at its base (Figure 6). Bolometers contain a transition edge sensor (TES) supported by six legs of silicon nitride (N_4Si_3), a material with poor thermal conductance. The interior web is made of gold wire with much higher thermal conductance. In the center of the conducting web is the TES itself. The TES is made of titanium and aluminum, and becomes superconducting at 550mK. The TES will be directly thermally connected to a cold bath, cooled by means of a He-3 refrigeration unit to 300mK. When radiation hits the gold wire web, it will attempt to dissipate its heat through the path of least resistance, flowing through the TES. The TES will register this change in temperature with a corresponding change in resistance as it crosses above its critical temperature. That detection will be read-out through SQuID boards electrically connected to the bolometer and recorded for post-flight analysis.

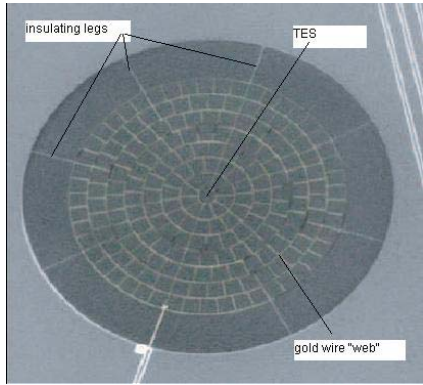


Figure 6: a single TES bolometer. Each focal plane will contain 900 such detectors that register incoming radiation through a change in resistance.

MODEL CONSTRUCTION

As discussed in the previous section, the cryostat design is complex and multi-faceted. 3D-CAD models have proved

helpful for initial plans, but present significant limitations in final designs. Because of the large size and costly components, a scale model makes planning less time consuming and more cost effective than full construction, while more accurate than computer-aided models. Creating a model will allow for hands-on electronics planning, confirmation of model feasibility, and easy troubleshooting of design components. The experience of constructing the scale model will aid in determining techniques for effective mounting of optical elements and assembly of cryostat.

A half-scale was chosen for ease of construction: pieces are large enough to work with but small enough to transport alone. Half-scale also simplifies conversion between drawings and model. Model materials were chosen for ease of machining, cost, and availability. The following materials were used in the model construction:

PVC foam/“Sintra”: a light-weight inflexible foam board that is highly machinable. Sintra was used for the majority of interior support structures and all horizontal components of cryostat shells, and was chosen for its combination of machinability and support capability.

PVC tubing: a hard plastic tubing used to cover metal support beam on interior of cryostat.

Acrylic: clear plastic used to simulate all lenses. Each lens was shaped manually.

Aluminum Sheet Metal: used for cryostat shell layers. Chosen for ability to support upper structures and ease of shaping to appropriate diameter.

Adhesives: simple epoxy was used to bond sheet metal and acrylic to plastic. To fix two sheets of Sintra together, Oatey PVC Cement was used.

Support: four central support columns of threaded brass rod (1/4-20) were used to simulate the four central interior beams and

provide structural integrity. Each layer of the model was secured with brass nuts to prevent shifting and increase accuracy in dimensions.

The level of detail necessary in modeling the cryostat was determined by the stage of design in each component as well as the effectiveness of computer models in that component. Spacing of shells and open space within the cryostat will be crucial for determining location and structure of electrical wiring systems, so these pieces received significant attention and detail. The interior layers of the focal plane assemblies, on the other hand, have been extensively modeled with computer programs and will not have any further pieces added. These were modeled as rough approximations of shape and size. As were lenses, which did not need to function within the model and had precisely determined shapes and sizes without the aid of a physical model.

IMPACT TESTING

Upon conclusion of the balloon flight, all payload elements will be separated from the balloon and fall to earth by means of an attached parachute. As the parachute deploys, elements in the payload will be free falling and possibly tumbling, and must be tested to an acceleration of 10g to prepare for maximum parachute shock. Among the most sensitive elements are the silicon wafers, on which the detectors are mounted. Each wafer is 0.5mm thick and will be mounted on a metal support within the focal plane assembly.

In a series of tests, silicon wafers were fixed to aluminum and invar (Nickel-Iron alloy) supports with Apiezon-N vacuum grease. Apiezon-N was chosen for cryogenic temperatures rating. The wafer-mounting

assembly was cooled to liquid nitrogen temperatures (77K) and was manually accelerated, being stopped by impact with a hard surface at accelerations estimated between 10 and 50g.

It was determined that Apiezon-N application was most effective when base was heated slightly, to allow for a very thin, smooth, even coating of grease. Invar was judged superior to aluminum as a support for the silicon wafers, as its thermal expansion coefficient is much closer to that of silicon. Aluminum had a tendency to contract at a very different rate, snapping the bonding of the vacuum grease. Even when using invar, grease was most effective when allowed to change temperatures slowly, as will be the case in the cryostat assembly. This allowed grease to expand and contract with the surrounding materials and hold the bond firm. When these allowances are made, Apiezon-N was shown to effectively hold silicon wafers to invar supports to maximum manual accelerations. Thus, no other bonding structures should be needed to hold silicon wafers in the cryostat.

EXPECTED RESULTS

EBEX has four primary scientific goals: to detect the B-mode inflationary gravitational-wave background signal; to provide critical information about the polarization of Galactic foregrounds, particularly of dust emission; to measure the yet undetected signature of lensing of the polarization of the CMB; and to improve the determination of several cosmological parameters. [6] Three to four frequency bands will be scanned to accomplish these goals. The primary “science band” will be centered at 150 GHz, at the peak ratio of inflationary B-mode power signal to that of galactic foreground B-modes. As long as

inflationary B-mode polarization exists within the theorized limits (i.e. signals 2 orders of magnitude smaller than corresponding E-mode polarization), the bolometric detectors should be sensitive enough to detect it. If no B-mode polarization is detected by EBEX, we will be able to set an upper bound on the signal power that is a factor of 15 more restrictive than current bounds.

One of the biggest sources of noise will be emissions from galactic dust. Magnetic fields in space align dust particles such that emitted photons will be polarized. The upper frequency bands will be dedicated to gathering data on these dust emissions, as any polarization data gathered there should be dominated by dust rather than the CMB. The behavior of the dust emissions can be extrapolated from these two bands and therefore subtracted from the lower band, allowing a cleaner picture of strictly CMB polarization. Detailed data has never before been taken on dust emissions, making this a useful tool for any further polarization research.

CONCLUSION

EBEX will improve upon previous experiments in the field of observational cosmology, as well as pioneer new areas of investigation. By studying the polarization of the CMB, we hope to clarify some of the many uncertain details of the inflationary period: How fast was the universe expanding? Was the rate constant or did it fluctuate? Most importantly, EBEX hopes to provide the first experimental confirmation for the inflationary paradigm. Even if it falls short of this goal, EBEX will provide valuable information about polarization signals of galactic foreground sources, enhance the existing polarization

maps, and prepare the way for future experiments.

ACKNOWLEDGEMENTS

My deepest thanks to those who have taught me so much this summer: my advisor for accepting me into this research group and guiding me in my work; Clay Hogen-Chin, Johannes Hubmayr, Tomotake Matsumura, Michael Milligan, Kyle Zilic, and all of the graduate students for their willingness to answer my questions and teach me about “doing physics”; Jon Kilgore and all of the School of Physics and Astronomy Machine shop machinists for their advice and assistance. I would also like to extend a thank-you to Serge Rudaz, Wendy Tschaapl, and the University of Minnesota Department of Physics and Astronomy for organizing and hosting the Research Experience for Undergraduates program. Finally, thank you to the National Science Foundation grant #0139099 for funding this experience.

REFERENCES

- [1] L. Page, G. Hinshaw, E. Komatsu. Three-Year Wilkinson Microwave Anisotropy Probe (WMAP) Observations: Polarization Analysis. http://map.gsfc.nasa.gov/m_mm/pub_papers/polarization/wmap_3yr_pol.pdf March 2006.
- [2] Coles, Peter, *Cosmology: A Very Short Introduction* (Oxford University Press, Oxford, 2001), p.93-106.
- [3] D. N. Spergel, R. Bean, O. Dore, M. R. Nolta. Three-Year Wilkinson Microwave Anisotropy Probe (WMAP) Observations: Implications for Cosmology. http://map.gsfc.nasa.gov/m_mm/pub_papers/parameter_s/wmap_3yr_param.pdf, March 2006.
- [4] D. N. Spergel, L. Verde, H. V. Peiris, E. Komatsu, M. R. Nolta. First-Year Wilkinson Microwave Anisotropy Probe (WMAP) Observations: Determination of Cosmological Parameters. *Ap. J. Suppl.*, 148:175-194, September 2003.
- [5] S. Hanany, et al. The EBEX Proposal. http://groups.physics.umn.edu/cosmology/ebex/group/wiki/media/Proposal/ebex04_science.pdf, p 5. July 2006.
- [6] i bid, p. 3.

Mapping the Asymmetry of the Milky Way: CCD Imaging and Star Counts

Undergraduate Student

Laura A. Broaded
Butler University
Indianapolis, IN

Advisor

Dr. Roberta Humphreys
University of Minnesota
Minneapolis, MN

Mapping the Asymmetry of the Milky Way: CCD Imaging and Star Counts

Laura A. Broaded,
Butler University, Indianapolis IN

Advisor: Dr. Roberta Humphreys
University of Minnesota REU Program 2006

ABSTRACT

A significant excess of stars have been identified in the first quadrant of the inner galaxy above and below the galactic disk. In an effort to construct a detailed map of this asymmetry, star count ratios from the first and fourth quadrants will be computed. My research consisted of reducing and analyzing CCD images from several fields in the fourth quadrant in preparation for calculating star count ratios. Creating a map of the asymmetry will help determine how it formed. Possibilities for the origin of the asymmetry include a merger galaxy, a triaxial thick disk and interaction of the inner halo with the stellar bar.

1. Introduction

Past research by Roberta Humphreys, Jeffrey Larsen and Jennifer Parker has identified a significant excess of faint stars in the first quadrant of the Milky Way. This excess was found above and below the galactic disk in quadrant I in the region $l \approx 20$ to 50 degrees and $b \approx 25$ to 50 degrees, where l and b are the respectively galactic longitude and latitude. The asymmetry is not only spatial, but kinematic as well, showing a slower rotation with respect to the galaxy. The lag of these stars was found to be 80 to 90 km/s in the direction of Galactic rotation.[1]

We continue to study this asymmetry to better understand the structure of the inner galaxy. Our goal is to more accurately determine the shape of the feature by doing star count ratios between the first and fourth quadrants. My research consisted of analyzing CCD images of several fields in quadrant IV in preparation for calculating these ratios. A thorough understanding of the shape, distribution, stellar population and kinematics of the asymmetry will point to the origins of the feature. Determining the origin of the asymmetry will help better determine the history and formation of our galaxy, and may have implications for cosmology and dark matter. Some possibilities for the origin of the asymmetry are a merger galaxy, a triaxial thick disk and interaction of the inner halo with the stellar bar. An asymmetry caused by the stellar bar requires a lag of stars behind the bar. These stars would then have a slower velocity in the “wake” of the bar, which was found in past research. Additional spectra for metallicities and spectral classifications will be obtained for further kinematic analysis.

2. CCD Reduction with IRAF

The CCD Images

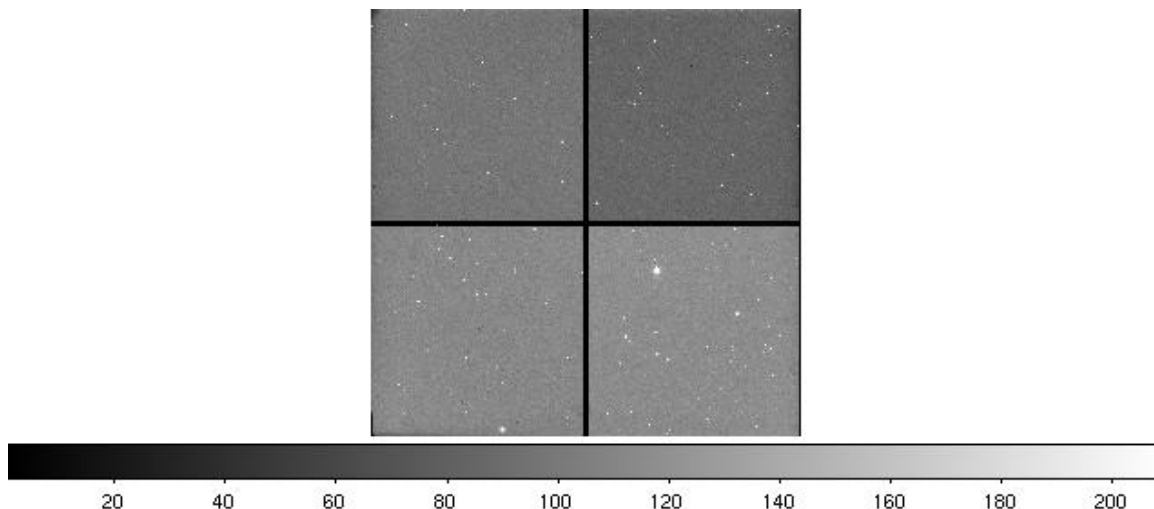
Charge-coupled devices are commonly referred to as CCDs, and are the same type of instrument as a commercial digital camera. CCDs have revolutionized astronomy, making it possible to see deeper into the universe and therefore farther back in time. A wonderful property of CCDs is that they respond linearly to light. This feature is very convenient when analyzing the data collected from a CCD image. The CCDs read out in terms of ADUs, or analog-to-digital units. ADUs are proportional to the electrons collected by each pixel, and are proportional by a factor referred to as the gain.[2]

Astronomical Observation

Dr. Roberta Humphreys, along with colleague Dr. Juan Cabanela, collected roughly two hundred CCD images a night between April 5th and 10th, 2006 at the Cerro Tololo Inter-American Observatory in Chile. They used the one meter Yale telescope at CTIO with the Y4K camera, and took images that span approximately one degree of the sky. The CCDs images were taken through U, B, V and R filters. CCD images of fields in the first quadrant were taken by collaborator Jeff Larsen at Steward Observatory between May 20th and June 2nd, 2006. I analyzed the fourth quadrant data from CTIO's one meter telescope with a program called IRAF, Image Reduction and Analysis Facility, and scripts written by Juan Cabanela.

2.1 The First Step: Trimming the Images

The CCD detector was divided into four quadrants which were read out separately. Consequently, there are “dead” regions on the CCD which are shown in the following image. The scale is in terms of ADU counts.



I used the script *y4ktrim* to correct for these “dead” regions. This script breaks the CCD image apart into four quadrants, fits each quadrant’s overscan region with a fifteenth order cubic spline. It then removes this overscan region from each quadrant and trims the image. The final step is to paste the four quadrants back together into a new trimmed image.

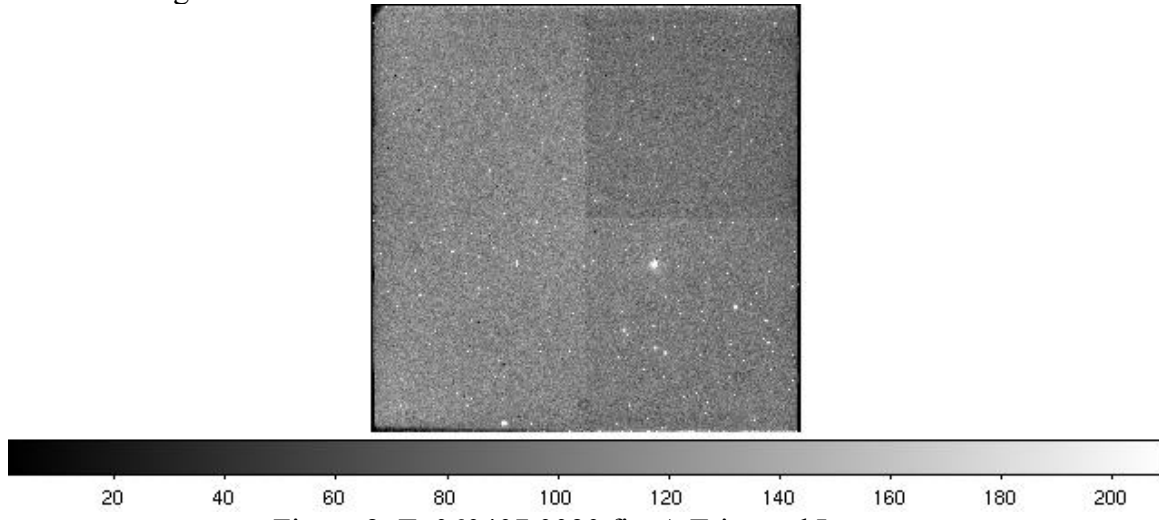


Figure 2: Ty060407.0090.fits A Trimmed Image

2.2 Bias Subtraction

The next reduction step is to subtract the bias, or background of the CCD, from all of the images. Some pixels in the CCD will always readout a value even when they are not exposed to light. To correct for this, zero-second exposures are taken from the CCD to take a reading of this bias. Our script *y4kzero* median combines the trimmed zero-second exposure frames into one median bias frame called Zero.fits. Then the script uses the IRAF command *imarith* to subtract Zero.fits from all of the object frames and flat frames.

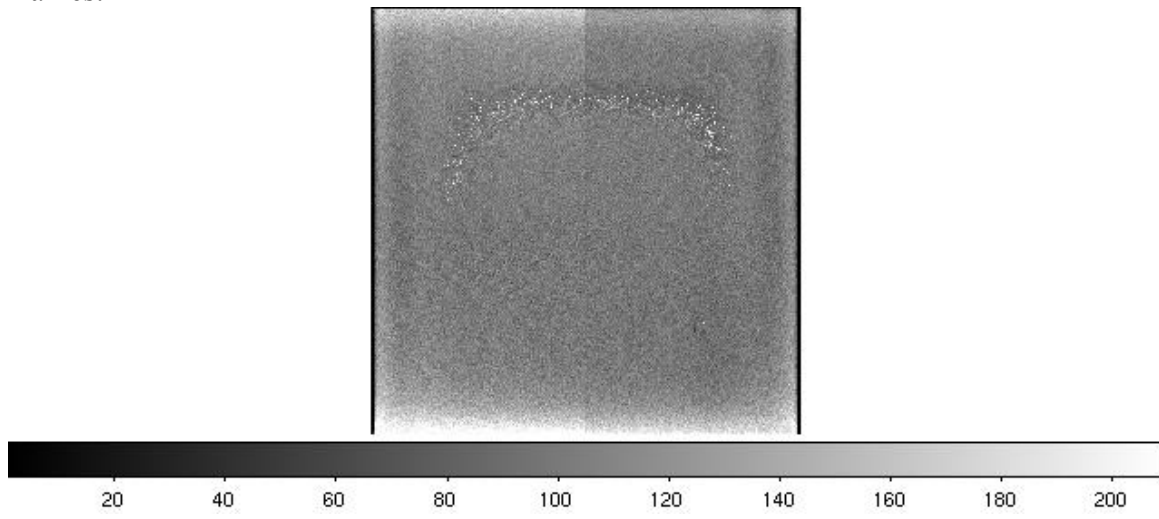


Figure 3: Zero.fits A bias frame

2.3 Flat Fielding

A flat field exposure is used to correct for variations between the pixels' response to light. Some pixels are more sensitive than others, so CCDs do not have a "flat" response to the sky. In order to correct for this, flat fields, images from a uniformly illuminated source, are taken through each filter. These flat fields can then be divided into our object frames to correct for the uneven response. The ratio of the two images will "flatten" our object frames and make all of the pixels effectively equally sensitive to light. There are several types of flats.

A domeflat is a flat field that is taken inside the telescope dome. The telescope is pointed to a flat, white spot in the dome that is illuminated uniformly by a lamp. The frames are taken in each filter separately, like any observation. There is a problem with these fields, however, because the wavelength distribution of a white dot is very dissimilar to the actual sky. These flats are not the ideal option, but are sometimes the only type of flat that time will allow for.[2]

A skyflat is a flat field taken of the sky. This is the preferred type of flat because the wavelength distribution is the same as our image frames. Median combination can be used to eliminate stars, thus many frames are needed.

We decided to use skyflats on all of our images, but ran into a predicament. There was a moving anomaly on most of our flats. We discovered that a piece of the filter holder had come loose and was randomly blocking parts of the frame. Some images had the anomaly in one spot or another, but most did not. We moved anomalous images into a separate directory and applied anomalous flats to them.

Then we had to address how to flat field the images without the anomaly. Dividing non-anomalous images by anomalous flats would leave a mark on our images. In order to create a master that did not have the anomaly, we took advantage of the fact that it was in different places on different flats. We spliced two sides from different master flats together to create an anomaly-free master skyflat. The following table presents which master skyflats were applied to our images.

Date	U	B	V	R
5	6B-8 splice	5-6A	5-6A	6B-10
6A	6B-8 splice	5-6A	5-6A	6B-10
6B	6B-8 splice	6B-10 splice	6B-10	6B-10
7 #66-78	6B-7	6B-7	6B-7	6B-10
7 the rest	6B-8 splice	6B-10 splice	6B-10	6B-10
8 #77-80	No images	8	8	6B-10
8 the rest	6B-8 splice	6B-10 splice	6B-10	6B-10
9	6B-8 splice	6B-10 splice	6B-10	6B-10
10	6B-8 splice	6B-10 splice	6B-10	6B-10

Table 1: Master flat fields applied to images
Spliced flats are made from the right half of 6B-7 and the left half of 8.

To apply these flats to the images, I used a script called *y4kapplyflat*. All images with the same filter are divided by the corresponding flat. This process is repeated for each filter.

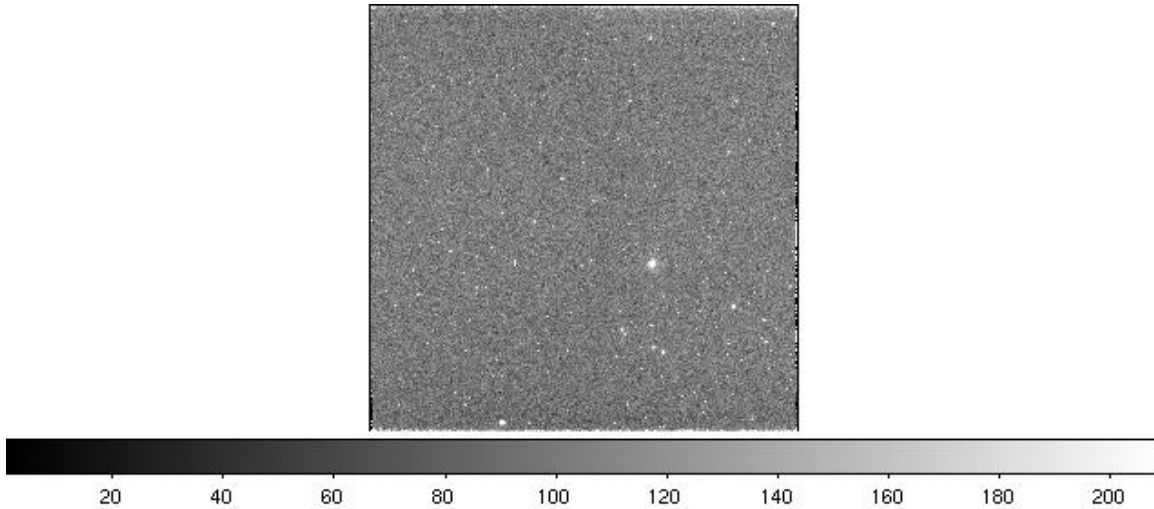


Figure 4: Fy060407.0090.fits: Flat-fielded image
Notice that the quadrants are all the same shade of grey after flat-fielding.

2.4 Cosmic Ray Removal

Cosmic Rays hits contaminate the images and can be falsely identified as stars. These cosmic rays are rejected by the Laplacian edge detection method. This method relies on the sharpness of the edges of the cosmic ray hits as opposed to the contrast between the rays and their surroundings.[3] I used a script called *y4kCRscrub* to “scrub” the cosmic rays from the images. It was a very long process and took about 30 hours to remove the cosmic rays for a night’s data.

2.5 Final Touches on Reduction

Two more problems need to be addressed before the images are ready for analysis. First, the coordinates of the frames are in terms of ‘x’ and ‘y’ instead of Right Ascension and Declination. To correct this, I used a program in IRAF to scan over the images and identify the 200 brightest sources in the field and match them with the USNO A2.0 astrometric catalog of stars with known RA and Dec. This transformation from ‘x’ and ‘y’ to the coordinate reference frame on the sky is called astrometry. Once the astrometry is performed, bad pixels in the CCD must be flagged and removed. This is because we do not want the bad pixels to interfere with the analysis of data. We use a bad pixel mask that is specific to the CCD and change all of the bad pixel values to 50,000 ADUs. When analyzing the data, we set an upper limit for ADUs that is less than 50,000, so the bad pixels are excluded from analysis.

3. Extinction Correction

All ground based astronomical observations are obtained through the atmosphere which causes extinction of the light. This is dependant on the angle of object from the zenith and is proportional to the secant of z, or airmass. The airmass is therefore proportional to the amount of atmosphere and can be used to correct for the effect of the atmosphere on the brightness of stellar objects. Each wavelength depends on airmass differently: the shorter the wavelength, the higher the extinction. Therefore, each wavelength should be analyzed separately. Two quantities are needed to graph the dependence: airmass and observed magnitude.

Aperture photometry is performed to calculate the observed magnitude of stars. Frames of the same fields at different airmasses are needed in order to graph meaningful data. To obtain observed magnitude I displayed an image and used *imexam* to obtain counts from a star. Counts divided by exposure time is referred to as flux f , which can be used to calculate the observed magnitude of the star. Observed magnitude m is given by:

$$m = -2.5 * \log_{10}(f) \quad (1)$$

Observed magnitude is calculated in Excel for the same stars in multiple frames and graphed against the airmass. Each star in a filter should have a similar slope, but should be graphed separately. The slopes are then averaged for each filter to be used as that filter's extinction coefficient, a value of how the counts depend on airmass.

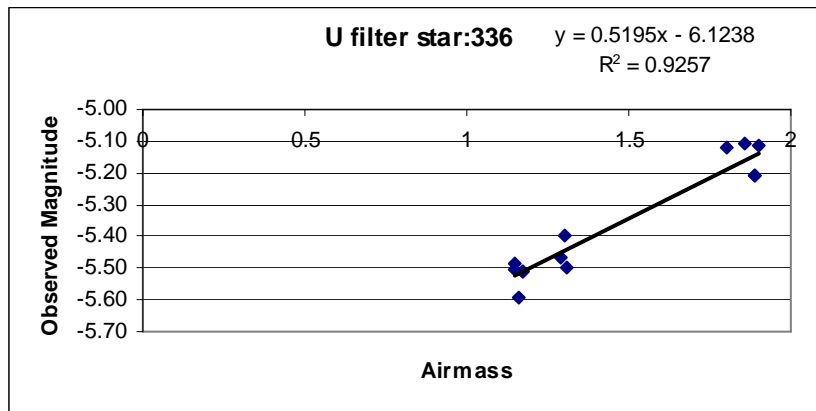


Figure 5: Extinction Graph for U Filter Star 336 in Landolt Field SA104

The results for the extinction coefficients are listing in the following table. Note how the dependence on airmass decreases with wavelength.

Filter	Extinction Coefficient	Sigma
U	0.53	0.09
B	0.26	0.04
V	0.12	0.02
R	0.068	0.007

Table 2: Obtained Extinction Coefficients

Our observed magnitudes are then corrected for airmass using the equation:

$$m = m_0 - kX \quad (2)$$

Where: m_0 is the extinction corrected observed magnitude
 m is the original observed magnitude,
 k is the filter specific extinction coefficient, and
 X is the airmass for the frame.[4]

4. Transformation Equations

We are now ready to transform our data onto the standard photometric system. We will obtain the actual magnitudes of the stars that we will be analyzing by comparing the extinction corrected observed magnitudes with the known magnitudes of standard stars. Transformation equations address these problems and convert data to the standard system. Generally, transformation equations with first order correction terms are as follows:[4]

$$V = v - k_v X + \varepsilon(B - V) + \delta_v \quad (3)$$

$$B - V = \mu[(b - v) - k'_{bv} X] + \delta_{bv} \quad (4)$$

$$U - B = \psi[(u - b) - k'_{ub} X] + \delta_{ub} \quad (5)$$

$$V - R = \rho[(v - r) - k'_{vr} X] + \delta_{vr} \quad (6)$$

Following from these equations, graphing:

$V-v_0$ vs. $B-V$ produces a slope of ε and an intercept of δ_v ,

$B-V$ vs. $(b-v)_0$ produces a slope of μ and an intercept of δ_{bv}

$U-B$ vs. $(u-b)_0$ produces a slope of ψ and an intercept of δ_{ub}

$V-R$ vs. $(v-r)_0$ produces a slope of ρ and an intercept of δ_{vr}

An example of a transformation graph is shown below. All nights were graphed separately for clear detection of outliers. Once a reasonable linear fit was made for each graph, the data from each night was averaged.

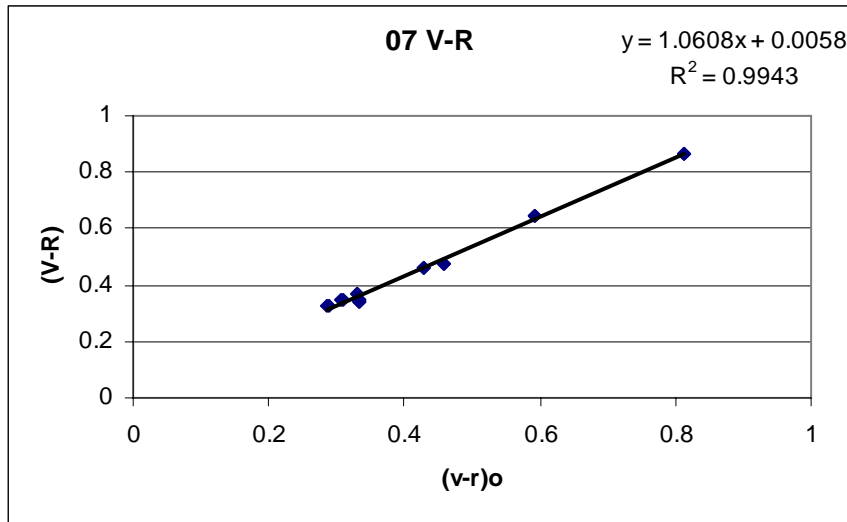


Figure 6: Transformation Graph - V-R graph of magnitudes for April 7th, 2006

The transformation data is as follows:

Day	epsilon	delta(v)	R^2 fit
5	-0.0251	23.075	0.0326
6	0.1161	23.052	0.7544
7	0.0948	23.069	0.5974
8	0.0852	23.072	0.7181
9	0.1484	23.059	0.351
Avg	0.084	23.065	
std dev	0.028	0.009	

day	mu	delta(bv)	R^2 fit
5	0.874	-0.0348	0.9935
6	0.8234	-0.018	0.9602
7	0.8029	-0.0326	0.9819
8	0.8111	-0.0452	0.9923
9	0.7585	-0.0026	0.9762
avg	0.814	-0.027	
std dev	0.028	0.018	

Day	psi	delta(ub)	R^2 fit
5	1.3037	-1.4662	0.991
6	1.0818	-1.0151	0.8705
7	1.0853	-1.0843	0.9158
8	1.1484	-1.2009	0.9766
9	1.1432	-1.1566	0.9408
Avg	1.152	-1.185	
std dev	0.090	0.173	

day	rho	delta(vr)	R^2 fit
5	0.9787	0.1627	0.9583
6	0.9828	0.0255	0.9876
7	1.0608	0.0058	0.9943
8	1.0507	-0.009	0.9945
9	0.996	0.0323	0.9217
avg	1.014	0.043	
std dev	0.039	0.069	

Now that the transformation coefficients have been calculated, extinction corrected observed magnitudes can be converted to the actual magnitudes in the standard system.

5. Future Research and Analysis

Future research on the project will produce valuable information about the shape and extent of the asymmetry of the thick disk. After transforming the data to the standard system, Magnitude vs. Color graphs will be plotted to assess the population of stars. Star counts will be conducted as a function of magnitude and color, and then used in ratios between the first and fourth quadrants. These ratios will give us information about the shape and extent of the asymmetry and help to determine the cause.

6. Conclusion

Reduction and calibration was conducted for CCD images of the 4th quadrant of the galaxy. Image frames were prepared for photometry by using reduction scripts in IRAF for trimming, subtracting the bias, flat fielding, cosmic ray removal, astrometry and bad pixel flagging. Extinction coefficients were calculated to correct for the effect of the atmosphere on the observed magnitudes of each wavelength, and transformation equations were calculated to transform the extinction corrected observed magnitudes to the standard system. Future research will consist of conducting star counts from this data and calculating ratios between star counts from the first and fourth quadrants of the galaxy. These ratios will map the asymmetry, and with the additional kinematic information, we hope to determine the cause of this peculiar feature of our galaxy.

7. Acknowledgements

First and foremost, I would like to thank my advisor Roberta Humphreys. Thank you for including me in your research project. I had a wonderful time working in the lab and learning all about stellar astronomy. Not only did I learn about this specific project, I learned about what it is like to do research at a large research institution. It has made me very excited to continue with my education in graduate school. I would also like to thank our collaborators Juan Cabanela and Josh Swanson. Juan was a second advisor to me and was extremely helpful; thanks for writing all of those scripts! Eric Aver and John Martin were great company in the lab, and answered *many* of my questions. Thanks for putting up with a lost undergraduate! Thanks to Serge Rudaz, Wendy Tschampl, Jennifer Docktor and the University of Minnesota for organizing such a rewarding REU program. Finally, I would like to thank the National Science Foundation for making this program financially possible through funding under grant number NFS/PHY-0139099.

References:

- [1] Parker, J. E., Humphreys, R. M., Larsen, J. A. 2003 The Astronomical Journal 126, 1346-1361.
- [2] Howell, S. B. *Handbook of CCD Astronomy*. New York: Cambridge University Press, 2000.
- [3] van Dokkum, Pieter G., 2001, PASP.
- [4] Hiltner, W. A., Hardie R. H. *Astronomical Techniques*. Chapter 8, “Photoelectric Reductions.” Chicago: University Press, 1962.

An Analysis of CME-Magnetosphere Interactions

Undergraduate Student

Jennifer Collier
Carthage College
Kenosha, WI

Advisor

Professor John Wygant
University of Minnesota
Minneapolis, MN

An Analysis of CME-Magnetosphere Interactions

Jennifer Collier
Carthage College, Kenosha, WI

Advisor: John Wygant
University of Minnesota, Minneapolis, MN

ABSTRACT

A survey of four CME-magnetosphere interactions was conducted using ACE, WIND, and CLUSTER satellite data. The CME-magnetosphere interactions caused magnetic storms in the magnetosphere, in which all had the following properties: sharp peak in the z_{GSE} direction of the magnetic field, similar (but oppositely directed) peak in the E_{dusk} direction of the electric field, and sharp peaks in the ion density and solar wind speeds, making them good candidates for analysis with higher time resolution data.

I. INTRODUCTION

The sun is continuously streaming charged particles towards the earth in what is called the solar wind. The solar wind is extremely hot and tenuous. The earth's magnetic field deflects these charged particles, protecting the earth. The solar wind has a typical ion density of approximately 7 particles per cm^3 and can range in speed from 300-700 km s^{-1} [1]. The solar wind is only disruptive and noticeable when solar flares and coronal mass ejections (CMEs) occur. Solar flares and CMEs occur during the solar maximum in the solar cycle. These events cause geomagnetic storms in the earth's magnetosphere. These storms are known to disrupt earth based communications and power grids. The storms can also wreak havoc on satellites orbiting the earth and cause auroras in the atmosphere. The storms are primarily caused by southward interplanetary magnetic field (IMFs) lines that are threaded within CMEs. These field lines then interconnect with the Earth's magnetic field and permit the transfer of energy, mass, and momentum into the magnetosphere [2].

II. BACKGROUND

A. Solar dipole magnetic fields

Since the earth has a magnetic field, it is generally shielded from the harmful effects of the solar wind. As stated in the introduction, only CMEs and flares cause any damage to the earth. The main reason for this is the orientation of the IMFs. The sun has a dipole magnetic field similar to that of earth, but unlike the earth, the sun's magnetic dipole regularly flips once every eleven years making the magnetic field lines similarly or oppositely oriented to the earth's magnetic field lines. If the IMF is

oriented similarly to the earth's field lines, then it is directed in the northward z_{GSE} direction and there is a closed magnetosphere. This means that any particle from outside the planetary region will remain outside and simply spiral along the IMF lines. If the IMF is oriented oppositely to the earth's field lines, then it is directed in the southward z_{GSE} direction and there is an open magnetosphere. In this case, the field lines from the CME and the earth can interact and magnetic reconnection occurs. This causes there to be three distinct field lines: IMF lines, planetary dipole-like lines, and lines that go through both the sun and the earth. The reconnected magnetic field lines allow for outside particles to enter the earth's atmosphere [3]. It is because of these southward directed field lines that make CMEs such a hazard to earth.

B. Coronal mass ejections

During the solar maximum, the most active phase of the solar cycle, CMEs dominate the solar activity. CMEs are massive flows of plasma (ranging from "5 $\times 10^{12}$ to 5 $\times 10^{13}$ kilograms" [4]) from the corona that are threaded with intense magnetic field lines. The density of CMEs varies throughout them and CMEs can have speeds that reach up to 1000 km s^{-1} . To expel the amount of mass as fast as it does, a CME typically carries approximately 10^{23} to 10^{24} Joules of energy with it. The size of CMEs increases rapidly as soon as they are ejected from the sun. Near the sun the size is "comparable to that of the visible solar disk" [4] and this size increases exponentially as it moves outward from the sun.

There are three key regions within the structure of the CME that contain intense magnetic field lines. The CME is usually fronted by a shock as it travels through interplanetary space towards earth. The CME shock is caused because the flow of the CME is supersonic; meaning the speed differential between the CME and the slower upstream solar wind is greater than the “magnetosonic wave speed ($50\text{-}70 \text{ km s}^{-1}$)” [2]. Following the CME shock is the sheath region. This region is “composed of swept-up, compressed, and accelerated plasma” [1]. Behind this region is the magnetic cloud. The magnetic cloud contains strong, but slowly varying, magnetic fields and essentially “drives” the CME [2]. The magnetic cloud is typically made out of low-beta plasma due to the low temperatures and high-intensity magnetic fields within the cloud. Figure 1 shows a time elapsed progression of a CME leaving the sun and one can easily see the structures described.

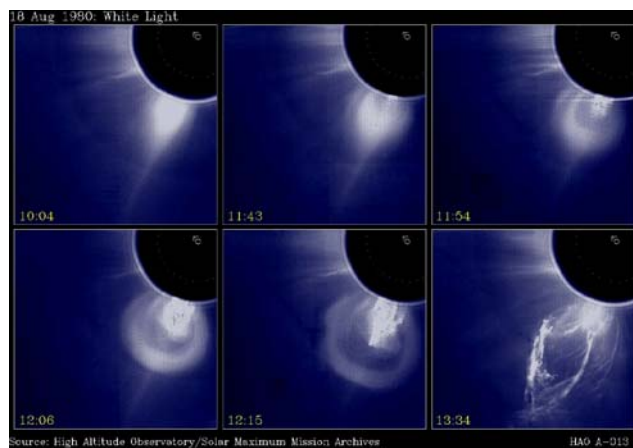


Figure 1. Example of a CME.

Similar terminology is used to describe the event of a CME and magnetosphere interaction. The first thing that happens when the CME comes into contact with the magnetosphere is a bow shock. Again, due to the supersonic nature of the solar wind/CME there has to be this shock. The CME will then hit the magnetosheath which is simply a transitory phase between the shock and the magnetopause. The magnetopause is the boundary between the IMF and the earth’s magnetic field and this is the final thing the CME goes through before actually entering the atmosphere. Figure 2 is a drawing of all the parts of the magnetosphere that were mentioned above.

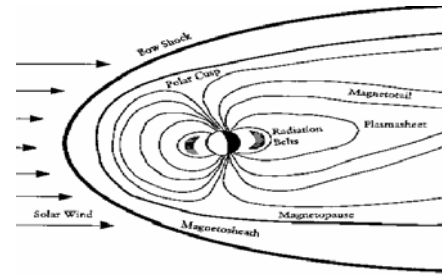


Figure 2. A drawing of the earth’s magnetosphere.

C. Ring current

Located around the earth at about three to five earth radii¹ is the ring current (not shown). The ring current is caused by energetic particles that are trapped in the earth’s magnetosphere and during a geomagnetic storm the number of particles increases, enhancing the ring current. This enhancement is a “prime indicator of a magnetic storm” [1].

Once particles are inside of the magnetosphere, protons will drift from the midnight to dusk directions and electrons will drift oppositely (dusk to midnight). It is this oppositely oriented drifting that causes the ring current. Since the ring current is a diamagnetic one, it will decrease the intensity of the earth’s magnetic field. It is this measurable decrease that “is a measure of the [geomagnetic] storm’s intensity” [1].

III. INITIAL DATA COLLECTION

The simplest way to find CME shocks is to look at D_{st} data provided by Kyoto University in Japan. D_{st} data is an index describing changes in the magnetic field at the surface of the earth, at low latitudes. This measurement of the magnitude of the earth’s magnetic field is organized by month and year. Looking at the graphs compiled by Kyoto University, a storm can be identified. For the most part, the earth’s magnetic field is stable and only has slight variations in magnitude. When a CME hits the magnetosphere, the resulting storm is easily distinguishable by a large dip in the magnitude of the magnetic field. The best storms to look for are ones where the magnitude of the magnetic field dips lower than -100nT .

The best time to look at the D_{st} data is between the months of November and May since this is the time when the satellites are in front of the magnetosphere. Looking at

¹ The radius of the earth is roughly 6400 km.

the D_{st} data between 2001 and 2005,² 27 storms were identified and recorded. Out of these 27, four were picked for further analysis due to their large magnetic field magnitudes. These storms occurred on the following dates: March 30-April 2 2001, April 10-April 12 2001, May 14-May 17 2001, and May 29-June 1 2001. The D_{st} data from May 2005 in which the best storm occurred on May 15, 2005 is shown in Figure A1.

IV. SATELLITE MEASUREMENTS IN THE SOLAR WIND

The next step was to examine the four storms closer using ACE, WIND, and CLUSTER satellite data obtained in the solar wind. These spacecraft were located immediately upstream of the Earth's magnetosphere. This data was gathered from the public CDAWeb provided by NASA. ACE and WIND satellites were used first to identify the storm. These two satellites monitor magnetic field values, solar wind speeds, and solar wind ion densities.

Figure A2 is the ACE data from May 14, 2005 to May 17, 2005 showing clearly the CME shock on May 15. The CME shock arrives at about 2:00 UT and is characterized by a sharp increase in the magnitude of the magnetic field followed by strong fluctuations. The region of strong magnetic fluctuations is called the "sheath" and these waves are believed to be created by the shock. At 5:00 UT there is a smooth increase in the magnetic field. This region of strong magnetic field is the magnetic cloud and lasts for several days.

Figure A3 presents data from the WIND spacecraft. There is a strong correlation between the magnetic field measurements from the three spacecraft because the scale size of the CME is probably about 1 AU and the spacings between the spacecrafat are much smaller. The plasma density measurement from WIND demonstrates that the sheath has a plasma density which is much larger than the solar wind density. This is believed to be the consequence a "snow plow effect" in which plasma is swept up in front of the CME as it moves through the interplanetary medium. These similarities in density peaks were found in all four of the magnetic storms examined.

CLUSTER is the only satellite that not only takes data for the three properties mentioned above, but also takes electric field data. An interesting observation about CMEs when the magnetic storm occurs is that the E_{dusk} component of the electric field and the z_{GSE} (northward) component of the magnetic field have a similar, but oppositely oriented peak (See Figure A4). This phenomenon was found in all four magnetic storms. This anti-correlation is the

consequence of the relation $E = -v \times B$ in the collisionless magnetized solar wind. In this relation, v is the velocity of the solar wind and B is the magnetic field of the solar wind/CME. The measured solar wind velocity (not shown) is about 1000 km/s away from the sun in the $-x_{GSE}$ direction. Given this velocity the peak magnetic field in the z_{GSE} direction inside of the cloud of 40nT is consistent with the electric field in the dawn direction of about -40mV/m. The good anti-correlation of the magnetic field and the electric field results from the constancy of the plasma velocity inside of the cloud. This is one of the first direct measurements of the electric field inside of a magnetic cloud. Notice, there are large fluctuations in the electric and magnetic fields in the sheath region. These fluctuations indicate the waves in the sheath are electromagnetic and many of their properties (including scale size) can be deduced from the ratio of the electric and magnetic fields using Faraday's Law.

V. CONCLUSION

Four magnetic storms were examined with three different satellites to see the effects of CME-magnetosphere interactions. It was found that each storm showed the same characteristics with wind speed, density, B-field, and E-field peaks. Now that these storms have been identified, further work in the space physics group will investigate the small scale structure of the cloud boundary to look for plasma structures similar to those which have previously been observed in the Earth's magnetosphere. The research conducted this summer was also an introduction for further research to be conducted on the effects of CMEs in the magnetosphere.

VI. ACKNOWLEDGEMENTS

I would like to thank Dr. John Wygant, my advisor on this project, for his help and guidance this summer. A special thanks to Scott Thaller for working with me and for being there to answer any questions that I had. Thanks to Serge Rudaz and Wendy Tschampl for keeping this program running smoothly. Thanks to the NSF (NSF/PHY 0139099) for sponsoring this REU program, without which I would never have had the chance to work in space physics.

² 2001 was chosen as a starting point for the data because this was the year that the CLUSTER satellite was launched and the D_{st} data stops in August 2005.

APPENDIX

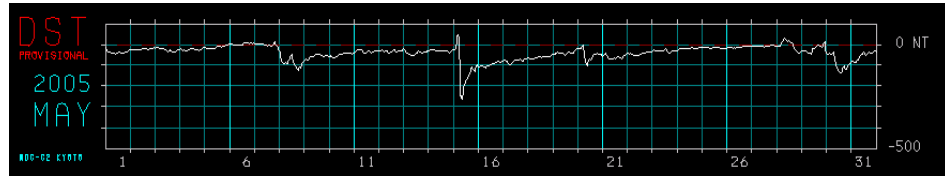


Figure A1. D_{st} data from May 2005 showing variations in the surface magnetic field of the earth due to geomagnetic storms caused by CME impacts.

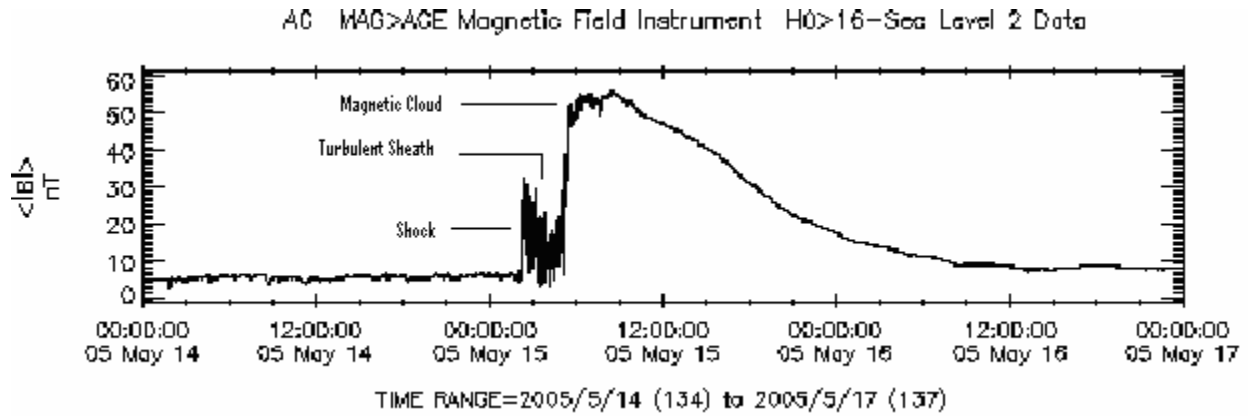


Figure A2. Magnitude of the magnetic field from ACE spacecraft the signature of a CME.

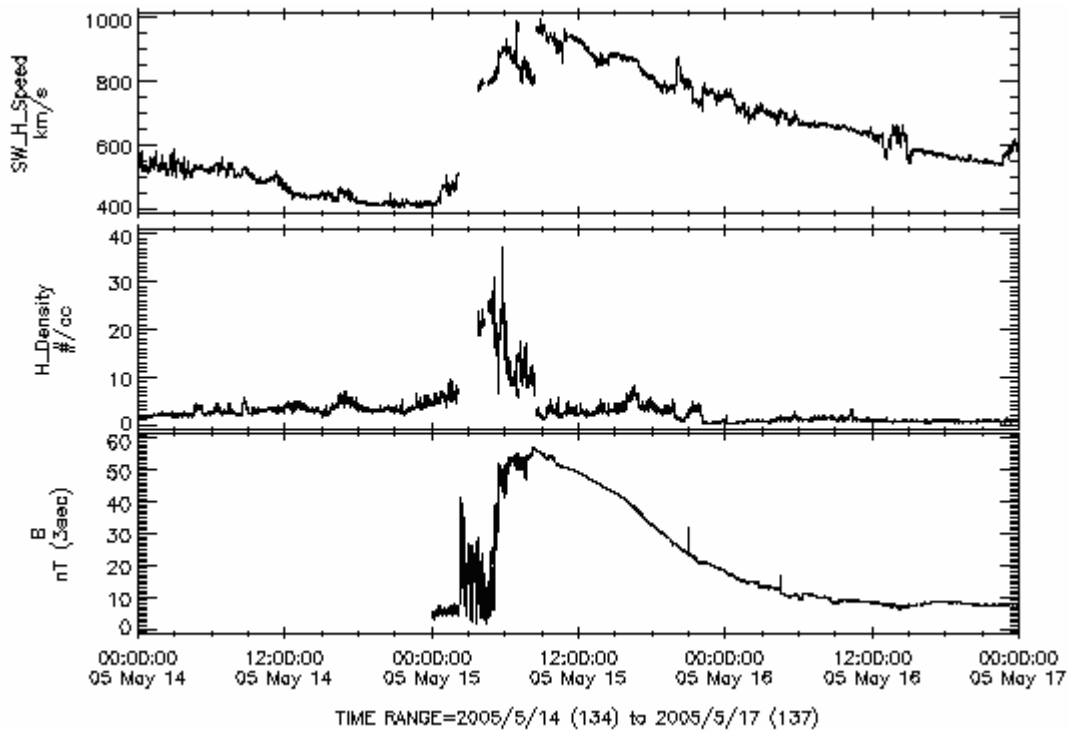


Figure A3. ACE and WIND spacecraft data in the solar wind, from the May 15 storm, showing the simultaneous peak in solar wind speed, ion density and magnetic field magnitude.

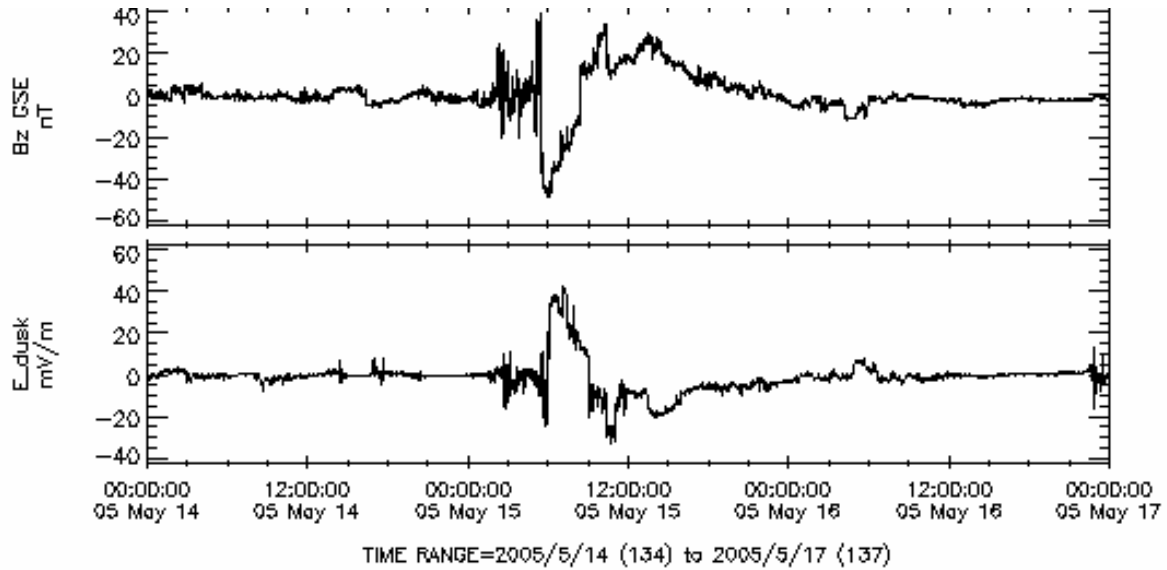


Figure A4. ACE spacecraft data (B_z) and CLUSTER spacecraft data (E_{dusk}), both in the solar wind, from the May 15 storm, showing the similar, but opposite, peaks in the E_{dusk} and B_z data.

VII. REFERENCES

- [1] Tsurutani, Bruce T. and Walter D. Gonzalez. "Magnetic Storms." *From the Sun: Auroras, Magnetic Storms, Solar Flares, and Cosmic Rays*. Ed. Steven Suess and Bruce and Tsurutani. Washington, DC: American Geophysical Union, 1998. 57-65.
- [2] Tsurutani, Bruce T. and Walter D. Gonzalez. *The Interplanetary Causes of Magnetic Storms: A Review*. Washington, DC: American Geophysical Union, 1997.
- [3] Dombeck, John. *Plasma Situations in Outer Space with the Interplanetary Magnetic Field*. Milwaukee: University of Wisconsin—Milwaukee, 1996.
- [4] Lang, Kenneth R. *The Sun from Space*. Germany: Springer, 2000.
- [5] Coronal Mass Ejections. Retrieved July 17, 2006, from http://genesismission.jpl.nasa.gov/science/mod3_Sun_lightSolarHeat/SolarStructure.
- [6] Chen, Francis F. *Plasma Physics and Controlled Fusion. Volume 1: Plasma Physics*. 2nd Ed. New York: Plenum Press, 1984.

Supercontinuum Generation in Photonic Crystal Fibers

Undergraduate Student

Sean Krzyzewski
Marquette University
Milwaukee, WI

Advisor

Professor Joachim Mueller
University of Minnesota
Minneapolis, MN

Supercontinuum Generation in Photonic Crystal Fibers

Sean Krzyzewski
Marquette University, Milwaukee, WI

Advisor: Joachim Mueller
University of Minnesota, Minneapolis, MN

Abstract

Recent advances in photonic crystal fibers allow the generation of supercontinuum at moderate powers with ultrashort laser pulses. We are exploring supercontinuum generation by coupling light from a Ti:Saph laser into a commercially available photonic crystal fiber (Femtowhite 800) and present initial experiments that test its suitability for running multiple wavelength fluorescence spectroscopy experiments. Super continuum was generated; however, a significant amount of light with the input wavelength passed through the fiber and dominates the spectrum, making it difficult to observe other wavelengths without the aid of extremely sensitive detectors. The power output was also too low and could not be compensated for by increasing the power without damaging the fiber. Further tests are being done to improve the power output, stability and spectrum.

Introduction

Supercontinuum generation is the creation of a broad spectrum by passing a laser beam through a non linear medium [1]. By taking this broad spectrum of light and routing it through various optical components, one is able to selectively choose either one or multiple wavelengths for a desired experiment. In the case of fluorescence spectroscopy, one could study fluorescent proteins at various wavelengths simultaneously in order to determine their fluorescence characteristics.

Theory and Background

Supercontinuum Generation

As theorized by Chiao, Kelly and Garmire in 1966, generation of supercontinuum through solid medium can be done through a combination of self-phase modulation along with Raman

scattering [2]. This was first demonstrated experimentally by Alfano and Shapiro in 1970 using borosilicate glass with 4 picoseconds pulses requiring an intensity of roughly 1 GW/cm^2 [2].

Recently supercontinuum generation has been demonstrated with photonic crystal fibers at powers of only 5 kW with 200 fs laser pulses [3]. This discovery opens up the possibility of utilizing supercontinuum light in the lab with short pulsed lasers.

A large number of non-linear effects, such as four-wave mixing and soliton decay, occur in supercontinuum generation [4]. Here, we create supercontinuum while pumping near the zero-dispersion wavelength of the fiber, where self-phase modulation and Raman scattering are the dominant non-linear effects [4]. As light passes through a material, a majority of the photons experience Rayleigh scattering and only their propagation is changed, not their

energy. However, a small number of photons, roughly 1 in 10^7 , do experience what is called Raman scattering [5]. The electric field of a photon comes into contact with the electron cloud surrounding an atom and polarizes it. If the induced dipole is modulated by a lattice vibration mode, the phonon and photon interact in an inelastic fashion. This causes a change in the frequency of the photon and causes a broadening of a spectrum [5,6].

Self-phase modulation begins with what is known as the optical Kerr effect. This is the changing of the index of refraction in a material due to a varying electric field, light, which is proportional to the irradiance of the light [5]. Assuming an initial electric field of a photon as:

$$E = E_{\omega} \cos(\omega t) \quad (1)$$

One is able to express the equation for electric susceptibility of a material in terms of both a linear and non linear susceptibility as given by:

$$\chi = \chi_{\text{lin}} + \chi_{\text{nonlin}} = \chi^{(1)} + \frac{3}{4} \chi^{(3)} |E_{\omega}|^2 \quad (2)$$

where χ is the electric susceptibility, E_{ω} is the amplitude of the electric field caused by the photon, $\chi^{(1)}$ is the linear term and $\frac{3}{4} \chi^{(3)} |E_{\omega}|^2$ is the third-order non linear term. Applying the relation between the index of refraction and the electric susceptibility:

$$n = (1 + \chi)^{\frac{1}{2}} = (1 + \chi^{(1)} + \frac{3}{4} \chi^{(3)} |E_{\omega}|^2)^{\frac{1}{2}} \quad (3)$$

which simplifies to roughly:

$$\approx n_0(1 + (1/2n_0^2) * \chi_{\text{nonlin}}) \quad (4)$$

As $\chi_{\text{nonlin}} \ll n_0^2$, one is able to use a Taylor expansion to derive the following

equation where the index of refraction becomes dependent on the intensity.

$$n = n_0 + (3 \chi^{(3)} / 8n_0) * |E_{\omega}|^2 = n_0 + n_2 I \quad (5)$$

where n_2 is the second order nonlinear refractive index and I is the intensity of the wave. Most materials have small values of n_2 , so large intensities (1GW/cm^2) are needed to create a significant change in the index of refraction [6], as seen in the original Alfano and Shapiro experiment.

When using ultrashort pulses with a Gaussian shape, such as those seen by a Ti:Saph laser, the index of refraction equation (5) which was dependent upon intensity becomes time dependent as well. For an ultrashort Gaussian pulse, the intensity is given as:

$$I(t) = I_0 \exp(-t^2/\tau^2) \quad (6)$$

where I_0 is the peak intensity and τ is half of the pulse duration [6]. Inserting $I(t)$ into equation (5), one sees an index of refraction involving time.

$$n = n_0 + n_2 * I_0 \exp(-t^2/\tau^2) \quad (7)$$

Taking the time derivative of this to see the instantaneous time dependent index of refraction:

$$dn/dt = n_2 * (-2t/\tau^2) * \exp(-t^2/\tau^2) \quad (8)$$

After a series of mathematical steps, one arrives at a instantaneous frequency $\omega(t)$:

$$\omega(t) = \omega_0 + (4\pi L n_2 I_0 / \lambda_0 \tau^2) * t * \exp(-t^2/\tau^2) \quad (9)$$

where ω_0 is the carrier frequency, λ_0 is the wavelength of the pulse and L is the distance the pulse have moved. For a

more detailed explanation of the steps between (8) and (9), see reference [6].

When looking at the direct effects of self modulation on a single wavelength with ultrashort pulses passing through a material, one will see the input peak of the Gaussian begin to drop while the edges become wider and taller. The actual width and height of the broadening is dependent on the input power as it is a non-linear effect.

Photonic Crystal Fibers

Photonic crystal fibers come in a variety of sizes and types, but this paper is only concerned with the femtowhite 800 and its specific type, single mode index guiding.

Index guiding photonic crystal fibers are made from a solid glass high index core with an air filled cladding structure [1]. An example of this can be seen in Figure 2. As the air holes span the entire length of the fiber, the mix of the elements creates an index of refraction which varies based on position.

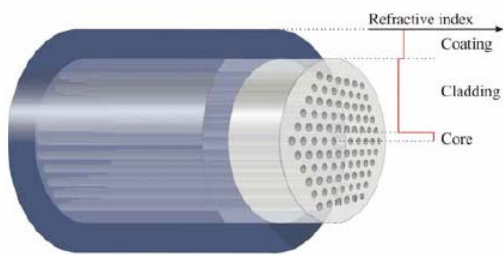


Figure 2 A single core fiber where the light is guided through the solid silica core [1].

Photonic crystal fibers have engineered optical properties. They can be single- or multi-mode, and have, designed zero dispersion wavelengths. An example of the two different core types can be seen in Figure 3.

By using single mode index guiding fibers such as the femtowhite 800, the power requirements to broaden

a single wavelength to an entire spectrum through self-phase modulation and Raman scattering have dropped considerably, allowing for novel experiments to be done in laboratories containing ultrashort laser pulses. A sample spectrum is shown in Figure 4

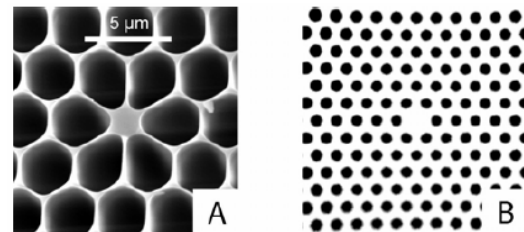


Figure 3 (A) SEM picture of a multimode fiber (B) Optical microscope picture of a single mode fiber [1].

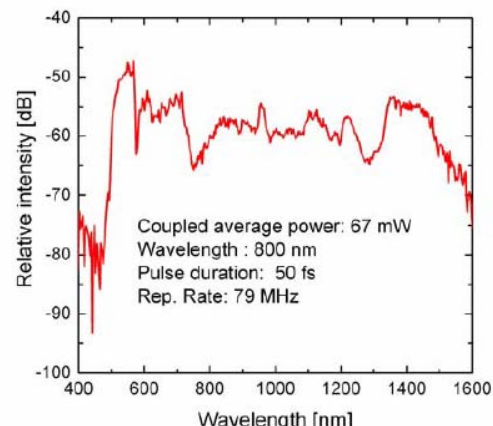


Figure 4 Supercontinuum generated in 1 m NL-PM-750 fiber from Crystal Fibre

Experimental Setup

The experiment was performed with a titanium-sapphire (Ti:Saph solid state laser with pulses of 100 femtoseconds, 760 mW of average power, but immediately went through a neutral density filter that dropped the power 50%. A vertically polarized beam was used that had roughly a 2 mm diameter at $1/e^2$.

Due to an extremely small crystal fiber core of $1.8 \mu\text{m}$, it is necessary to have a perfectly straight and level beam

path. This will help ensure that when focusing into the femtowhite 800, the light does not come into the objective at an angle and cause of a loss of power and incorrect focusing.

To align the beam, two mirrors and a measuring post at two marked spots were used. The beam was aligned to a close point and then a farther point, about a meter back but at the same height and distance in from the table. This had to be done many times over, each time adjusting the mirrors slightly.

The beam was then passed through a series of two neutral density filters to give a better control over the power. Because the generation of supercontinuum is highly dependent on power, it is necessary to have as much control over the power coming in as possible. This also allows for tests to be done to see the relationship between the power and the broadening of the spectrum.

In some cases, the beam was then passed through a $\lambda/4$ plate and a linear polarizer. These two components were installed so that the beam's polarization could be adjusted to match the optical axis of the femtowhite 800. By passing a beam through a $\lambda/4$ plate at the correct angle, the light will become circularly polarized. Then, a linear polarizer is able to select any angle to match the polarization axis of the crystal fiber. To test if the light was circularly polarized, a power meter was placed after the linear polarizer. If the linear polarizer could be rotated to any angle and stay roughly the same power, this is an indication of circularly polarized light.

Next, the beam entered a 2x beam expander and became roughly 5 mm in diameter. This was done in order to completely fill the back aperture of the objective so that the light could be

focused well into the crystal fiber. It then entered a 60x objective and was coupled into the femtowhite 800.

To collect the output beam from the femtowhite 800, a spectrometer was connected to a fiber and ran to a holder which was placed at the end of the crystal fiber. Since the hole for detecting light was so small, the placement of this detector needed to be adjusted for optimal detection. A picture of the set up can be seen below.



Figure 5 A photograph of the experimental setup

Because of the extremely small core size and the necessity to maintain a straight optical axis, the beam expander, objective and femtowhite 800 were all placed on platforms that have control to be less than one micrometer. In the case of the femtowhite 800's stage, it was actually a 5 axis stage to ensure optimal coupling.

To determine if supercontinuum was actually generated, the spectrometer's results were read onto a computer screen in real time. To create supercontinuum, an iterative process of turning each one of the adjustment knobs on the femtowhite 800's stage was done to maximize the output at lower levels, $\sim 8\text{mW}$. When the output was maximized at lower levels, power would be

increased and more adjustments would be done in order to maximize output.

To test the long term stability after generating supercontinuum, the set up would be left running for up to 3 hours. Tests longer than this were not done due to time constraints.

Results

The generation of supercontinuum through the femtowhite 800 was achieved with a spectrum ranging from 400 nm to 1100 nm. However, when the femtowhite 800 was aligned to generate supercontinuum with a pump power of 250 mW, there was only a few mW (1-3 mW) of output. An exact power output was not determined due to the device that can measure a broad spectrum of light was not sensitive enough to pick up the small power. However, a more sensitive detector which assumes a single frequency of light was used to measure the power using a setting of 800 nm. As the 800 nm light saturated the spectrum, using its power as a gauge of the overall power is a reasonable assumption. See Figure 6 and 7 for sample spectrum generated at various powers.

It was suggested by Crystal Fibre to correctly align the polarization of the incoming beam with the fiber as it is a polarization maintaining fiber. To test this, the beam was passed through a $\lambda/4$ wave plate and a linear polarizer so that the polarizer could be rotated to choose any degree of polarization from the circularly polarized light. There was no significant increase in power or change in spectrum when this was done.

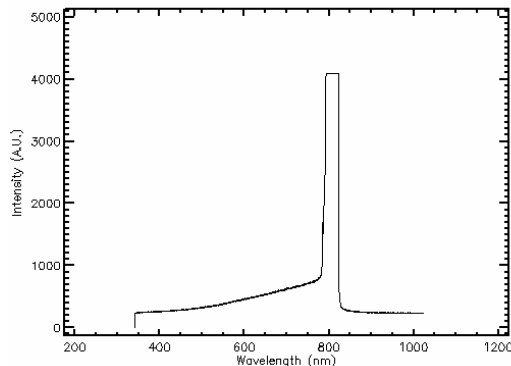


Figure 6 A plot of intensity (A.U.) versus wavelength (nm) by coupling by coupling in 8 mW of light with a 3 sec integration time.

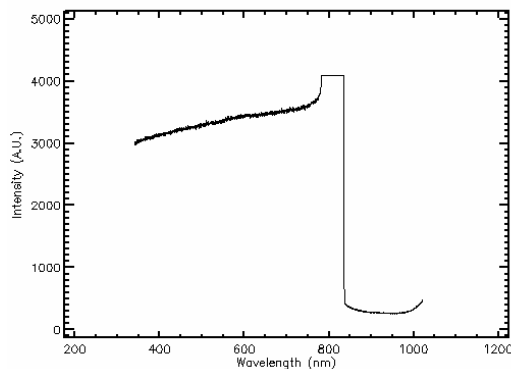


Figure 7 A plot of intensity (A.U.) versus wavelength (nm) by coupling in 30 mW of light with a 3 sec integration time.

The degree of sensitivity of coupling into the crystal fiber was also determined. It was found that movements of less than 1 μm would cause supercontinuum to decrease or vanish altogether. Vibrations transmitted through the floating optical table were also able to temporarily cease supercontinuum generation. This was countered by using increasingly more stable stages to house the fiber. An effort was also made to avoid contact with the table and keep a constant surrounding environment. When testing the stability over time, it was found that supercontinuum could last for at least 3

hours untouched. Tests longer than this were not done due to time constraints.

It was also found that as the beam passed through more optical components, it became increasingly more difficult to generate supercontinuum. Explanations for this will be given in the discussion.

Discussion

Supercontinuum was produced using the photonic crystal fiber; however, it was found that many small changes within the system altered the outcome greatly.

With every component added, the laser beam was forced to go through another medium, causing a lengthening of the duration of the pulse every time. As pulse length is roughly inversely proportional to the power needed to create supercontinuum, a doubling of the pulse length would require twice as much power. Power is also lost due to reflection every time the beam is directed at an optical element, but this was minimized by choosing the appropriate components. This indicates that the generation of supercontinuum is very sensitive to pulse length. When experimenting with the femtowhite 800, components such as beam expanders and polarizers were left out at times to reduce the amount of power needed in fear that increased power may damage the fiber.

Once coupling into the fiber was maximized, the output spectrum displayed an extremely large peak at 800 nm. Normally, this peak is expected to decrease significantly as the power is expected to go into the entire spectrum. Even though the pulse length was longer than that shown in Figure 4, powers less than 100 mW should be enough to create

a similar spectrum. We initially suspected that our failure to achieve this is caused by a misalignment in the polarization. To combat this, a $\lambda/4$ wave plate was used to circularly polarize the beam and then a linear polarizer was used to selectively choose a linear polarization angle. By rotating the polarizer, it should have been possible to align the beam's polarization with the fiber. It was found that the intensity of the 800 nm peak did not drop significantly as the polarization axis was rotated, indicating that the peak was not due to polarization misalignment.

A second theory as to the large spike at 800 nm was that not enough power was being used to create ideal conditions for supercontinuum. Although a broad spectrum was observed, it was not until higher powers on the order of 250 mW that the longer wavelengths broadened. It is possible that if more power was added, the 800 nm peak would have decreased significantly and a strong, more equally distributed spectrum would have appeared. This could not be tested as such powers could damage the fiber.

The other main problem with the output of the fiber was the extreme power loss. According to Crystal Fibre, a power efficiency of ~30-50% should be reached fairly easily if coupling correctly. As this is not seen, a few possible explanations arise.

An initial attempt to counter the power issue was to align the incoming beam's polarization with the polarization axis of the fiber. A slight increase in power was observed, but it amounted to a gain of less than 10%, indicating that the polarization was not the key to high output power.

Another possible reason for the low output power would be incorrect

coupling into the fiber. With a core size of 1.8 μm , extreme precision was needed to couple the beam into the fiber. Before involving the fiber in any measurements, the beam was aligned so that it ran parallel and straight with the optical table, making it easier to align components on the optical axis and help ensure that the beam was entering components straight on. As each piece was added, the output path was measured to make sure that the beam remained on the same path or, in the case of the objective, that the beam went through the back aperture dead on and focused correctly. When the fiber was added, it was mounted on a 5 axis rotation stage to help ensure that near perfect coupling could be achieved. As minimal power output was observed even with extreme precision in coupling, suspicions were raised as to a potential damage of the fiber. Tests are currently being done on the fiber, checking for cracks or abnormalities in the optic using a microscope. What exactly is the source of the problem is currently unknown.

Conclusion

As it stands, coupling a laser beam into the femtowhite 800 and using the output beam to do fluorescence spectroscopy is not possible due to the lack of output power as well as the beam being overpowered with 800 nm light, but a broad spectrum was created. However, other studies have shown a reasonable output power and a broad spectrum, indicating that further tests of the femtowhite 800 may show that either a.) the femtowhite 800 is damaged or b.) coupling into it requires more precise methods. Either way, work will still be done attempting to increase the power

efficiency so that it may be used for fluorescence spectroscopy.

Future Work

Since the generated spectrum is extremely sensitive to pulse duration, a beam compressor is currently being designed so that the pulses could be shortened to 50-60 fs to help compensate for the pulse lengthening due to inserting optical components. With shorter pulses, it would also reduce the power requirements to create supercontinuum.

A beam compressor with a wavelength selector is also being designed so that the output beam can be collected and passed through a compressor to shorten the pulses as well as compensate for the different velocities of the various frequencies of light leaving the end facet. After compressing and straightening the beam, it would pass through a simple or multiple slits that would allow only certain wavelengths. This would enable single or multiple wavelength fluorescence spectroscopy experiments.

Acknowledgements

I would like to thank Professor Joachim Mueller for his patience and guidance throughout the project. I would like to thank Dr. Yan Chen and graduate students Joe Skinner, Bin Wu and Patrick for all their advice and help setting up my experiments. I would also like to thank the University of Minnesota for hosting a great REU program, especially Serge Rudaz and Wendy Tschampl.

Funding for this project was provided in part by the National Science Foundation grant no. NSF/PHY-0139099.

References

- [1] Hansen, K., Kristiansen, R.,
“Supercontinuum Generation in
Crystal Fibers,”
<http://www.crystal-fibre.com/support/Supercontinuum%20-%20General.pdf>
- [2] Alfano, R.R., Shapiro S.L.,
“Emission in the region 4000 to
7000 Å via four-photon coupling
in glass” Physical Review Letters
24, 584 (1970)
- [3] J. K. Ranka, R. S. Windeler, and A.
J. Stenzl, "Visible continuum
generation in air silica
microstructure optical fibers with
anomalous dispersion at 800nm
, " Opt. Lett. **25**, 25-27 (2000)
- [4] R.R. Alfano, “The Supercontinuum
Laser Source,” *Springer-Verlag*,
New York (1989)
- [5] Enoch, J., Van Stryland, E., Wolfe,
W., “Handbook of Optics,” 2nd
ed., McGraw Hill, New York
(2001)
- [6] “Self Phase Modulation.”
Wikipedia.org. 2006. Retrieved
Aug 1st, 2006.
<http://en.wikipedia.org/wiki/Special:Search?search=self+phase+modulation&go=Go>

A Schrödinger Approach to Holography

Undergraduate Student

Andrew Larkoski
University of Washington
Seattle, WA

Advisors

Tony Gherghetta & Brian Battell
University of Minnesota
Minneapolis, MN

A Schrödinger Approach to Holography

Andrew Larkoski

Department of Physics

University of Washington

Seattle, WA 98195

Abstract

The Randall-Sundrum solution to the hierarchy problem has incited much further research into consequences of the model, both motivated by the hierarchy problem and holography. Here, we review scalar and fermion fields in the bulk, studying the Kaluza-Klein modes of both fields. We introduce a Schrödinger approach to studying the fields and the corresponding potential for each. We review the AdS/CFT holography for both fields and find that the Schrödinger potential is an efficient guide to the dual theory.

1 Introduction

Warped extra dimensions, most notably Randall-Sundrum Anti de Sitter (AdS₅) space, has been shown to be a viable solution to the hierarchy problem[1] and has incited much research into further consequences of the model, both theoretical and phenomenological. The well-celebrated solution has also been shown to include the possibility of an infinite extra dimension[2] (RS2) due to the highly warped geometry. The graviton in this situation is localized on the single 3D brane in the 5D bulk. Also, evidence of extra dimensions could be found at the Large Hadron Collider (LHC) in the coming years. Low energy Kaluza-Klein modes could be excited at the LHC and evidence of them could be determined from resonances, possibly even the graviton as a spin-2 resonance.

Here, we consider five-dimensional spacetime with the metric[1]

$$ds^2 = e^{-2k|y|} \eta_{\mu\nu} dx^\mu dx^\nu + dy^2 \quad (1)$$

where k is the AdS curvature scale and $\eta_{\mu\nu} = \text{diag}(-1, 1, 1, 1)$ is the familiar Minkowski metric with $\mu, \nu = 0, 1, 2, 3$ the 4D Lorentz indices. This is the Randall-Sundrum model (RS1) which provides a solution to the hierarchy problem with two 3D branes in 5D spacetime. The branes are located at $y = 0$ and $y = \pi r$, and are referred to as UV and IR branes, respectively. This nomenclature denotes the relative energy scales located on each brane, with the UV (high energy) brane of the order of the Planck scale and the IR (low energy) brane of the order of a TeV. The 5D spacetime exhibits orbifold symmetry in the extra dimension so that the metric is even about the UV brane (that is, $(x, y) = (x, -y)$ for $|y| < \pi r$) and also even about the IR brane ($(x, \pi r + y) = (x, \pi r - y)$ for $|y| < \pi r$). This set-up has important consequences as will be discussed. In the RS1 solution to the hierarchy problem, all Standard Model particles and forces are located on the IR brane as all masses are scaled from m on the UV brane to $me^{-k\pi r}$ on the IR brane. The weakness of gravity on the IR brane is a consequence of the metric (as discussed in [2]) as the graviton is always localized on the UV brane.

Motivations from string theory suggest a correspondence between a weakly-coupled 5D AdS theory and a strongly-coupled 4D conformal field theory (CFT) known as the AdS/CFT correspondence[3]. The AdS/CFT correspondence in the case of the RS1 solution has been well researched and discussed as in [3]. The hierarchy problem solution in light of the AdS/CFT is interpreted as a low cutoff scale (as compared to the Planck scale) associated with the conformal symmetry breaking scale of the CFT, similar to baryons and mesons in

QCD. The power of the AdS/CFT is that while perturbation theory is ineffective for the strongly-coupled CFT, calculations can be performed in the AdS₅ by this method and, by the correspondence, interpreted into the 4D CFT. The AdS/CFT is known as a holography as the information contained in the 5D theory is encoded in its 4D boundary.

In this paper, we study two fields in the 5D bulk, a scalar and a fermion, discussing the equations of motion and their solutions. We introduce a unique method of analyzing the fields via a non-relativistic quantum mechanics problem, which produces many intuitive and interesting results. Finally, we study the holography of the fields and tie the three analyses together by noting important coincidences.

2 Scalar Field in 5D Bulk

2.1 Kaluza-Klein modes

The 5D action of a massive scalar field in the bulk is

$$S = -\frac{1}{2} \int d^5x \sqrt{-g} [(\partial_M \Phi)^2 + m_\Phi^2 \Phi^2], \quad (2)$$

where $d^5x = d^4x dy$ is the 5D measure and $M = \mu$, 5 is the 5D spacetime index. Varying the action with respect to Φ and demanding it be stationary results in the equation of motion

$$\partial^2 \Phi + e^{2k|y|} \partial_5 (e^{-4k|y|} \partial_5 \Phi) - m_\Phi^2 e^{-2k|y|} \Phi = 0, \quad (3)$$

with $\partial^2 \equiv \eta_{\mu\nu} \partial^\mu \partial^\nu$. The boundary condition obtained from the variation is the Neumann constraint that $\partial_5 \Phi|_{y=0,\pi r} = 0$.

We make a separation of variables ansatz and write

$$\Phi(x, y) = \sum_{n=0}^{\infty} \phi_n(x) f_n(y). \quad (4)$$

The ϕ_n are the Kaluza-Klein modes with $\partial^2 \phi_n = m_n^2 \phi_n$ and f_n is the profile of the Kaluza-Klein mode in the bulk. We demand that the f_n satisfy the orthogonality relation

$$\int_0^{\pi r} dy e^{-2k|y|} f_n(y) f_m(y) = \delta_{nm}. \quad (5)$$

Then, the equation of motion reduces to

$$(\partial_5^2 - \text{sgn}(y) 4k \partial_5 + e^{2k|y|} m_n^2 - m_\Phi^2) f_n = 0. \quad (6)$$

The zero mode ($m_0 = 0$) solution is then given by

$$f_0(y) = c_1 e^{(2+\alpha)k} + c_2 e^{(2-\alpha)k}, \quad (7)$$

with $\alpha = \sqrt{4 + \frac{m_\Phi^2}{k^2}}$ and c_1 and c_2 some as-of-yet undetermined constants. Because of its reoccurrence throughout the analysis, we define the bulk scalar mass in terms of the curvature scale as $m_\Phi^2 \equiv ak^2$, with a some dimensionless constant so that $\alpha = \sqrt{4 + a}$. With the current Neumann boundary conditions, however, we observe that this would imply that $c_1 = c_2 = 0$, and thus no zero mode would exist. To assuage this, we introduce boundary mass terms on the branes yielding the boundary action[3]

$$S_{bdy} = -\frac{1}{2} \int d^5x \sqrt{-g} bk [\delta(y) - \delta(y - \pi r)] \Phi^2, \quad (8)$$

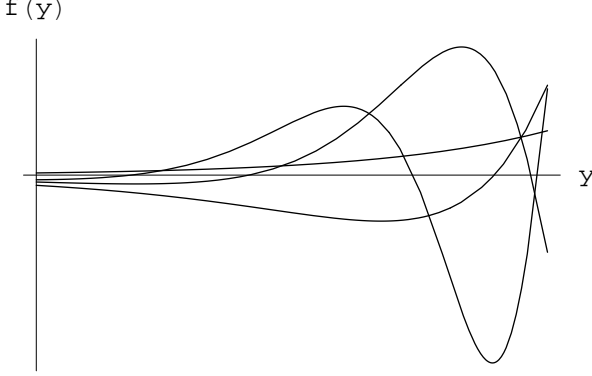


Figure 1: The first four modes of the Kaluza-Klein bulk scalar with $b < 2$. Notice that the massive modes dominate on the IR brane to the right.

where the boundary mass is defined in terms of the curvature scale and b is some dimensionless constant. The Neumann condition is then changed to

$$(\partial_5 - bk)f_n \Big|_{0, \pi r} = 0, \quad (9)$$

which does allow for a non-trivial zero mode. Plugging (7) into (9), we find that for only $b = 2 \pm \alpha$ does a non-trivial zero mode exist, so that

$$f_0(y) = N_0 e^{bk|y|}, \quad (10)$$

with N_0 the normalization constant determined by solving

$$1 = N_0^2 \int_0^{\pi r} dy e^{-2k|y|} e^{2bk|y|}, \quad (11)$$

which is simple in this case. Thus,

$$N_0 = \sqrt{\frac{2(b-1)k}{e^{2(b-1)k\pi r} - 1}}. \quad (12)$$

We note that the domain of b is the entire real axis (as $\alpha \geq 0$), and thus the zero mode can be localized anywhere in the bulk.

For arbitrary m_n , the solutions to Eq. 6 are Bessel functions, that is[5]

$$f_n(y) = N_n e^{2ky} \left[J_\alpha \left(\frac{m_n}{k} e^{ky} \right) + \beta_n Y_\alpha \left(\frac{m_n}{k} e^{ky} \right) \right], \quad (13)$$

where N_n and β_n are constants determined from the boundary conditions and normalization. To determine β_n , we impose the modified Neumann conditions (Eq. 9) on the UV and IR branes which yield

$$\beta_n = - \frac{(2-b)J_\alpha \left(\frac{m_n}{k} x \right) + \frac{m_n}{k} J'_\alpha \left(\frac{m_n}{k} x \right)}{(2-b)Y_\alpha \left(\frac{m_n}{k} x \right) + \frac{m_n}{k} Y'_\alpha \left(\frac{m_n}{k} x \right)}, \quad (14)$$

where $x = 1, e^{k\pi r}$. This can be greatly simplified by noting Bessel function identities as

$$\beta_n = - \frac{J_{\alpha \pm 1} \left(\frac{m_n}{k} \right)}{Y_{\alpha \pm 1} \left(\frac{m_n}{k} \right)} = - \frac{J_{\alpha \pm 1} \left(\frac{m_n}{k} e^{k\pi r} \right)}{Y_{\alpha \pm 1} \left(\frac{m_n}{k} e^{k\pi r} \right)}. \quad (15)$$

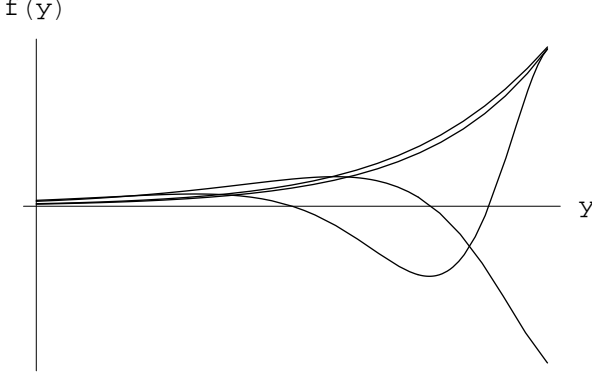


Figure 2: The first four modes of the Kaluza-Klein bulk scalar with $b = 2$. Now, the massless and massive modes couple with the same strength to the IR brane.

The masses m_n are thus found by evaluating this equation, where, in the limits that $\pi kr \gg 1$ and $\frac{m_n}{k} \ll 1$, the masses are approximately

$$m_n \approx \left(n + \frac{1}{2}\alpha - \frac{3}{4} \right) k\pi e^{-\pi kr}. \quad (16)$$

The massless and low-lying massive modes are plotted in Figs. 1-3 for various values of b , and are discussed in more detail in the next section.

2.2 Schrödinger Equation Formulation

It is useful to rewrite the equation of motion of the scalar field as a corresponding non-relativistic Schrödinger equation¹. To do so, we make the change of variables

$$f_n(y) = e^{3/2k|y|} g_n(z), \quad z = \text{sgn}(y) \frac{(e^{k|y|} - 1)}{k}. \quad (17)$$

We note that by orbifold symmetry

$$\partial_5 \text{sgn}(y) = 2[\delta(y) - \delta(y - \pi r)] \quad (18)$$

and the relation that

$$\text{sgn}(y)\partial_5 \text{sgn}(y) = \frac{1}{2}\partial_5 \text{sgn}^2(y) = 0. \quad (19)$$

Using these relations and substituting Eq. (17) into Eq. (6), the equation of motion for $g_n(z)$ is

$$\left(-\frac{1}{2}\partial_z^2 + \frac{15k^2 + 4m_\Phi^2}{8(k|z| + 1)^2} - \frac{3}{2}k \left[\delta(z) - \frac{1}{k|z^*| + 1} \delta(z - z^*) \right] \right) g_n = \frac{m_n^2}{2} g_n, \quad (20)$$

where we define $z^* \equiv (e^{k\pi r} - 1)/k$. This is Schrödinger's equation with potential $V(z)$ defined as

$$V(z) = \frac{15k^2 + 4m_\Phi^2}{8(k|z| + 1)^2} - \frac{3}{2}k \left[\delta(z) - \frac{1}{k|z^*| + 1} \delta(z - z^*) \right]. \quad (21)$$

The boundary conditions (Eq. (9)) for $g_n(z)$ become under this change of variables

$$\left. \left(\partial_z - \frac{k}{k|z| + 1} (b - 3/2 \text{sgn}(z)) \right) g_n \right|_{z=0, z^*} = 0, \quad (22)$$

where we have included the brane masses. The properties of this potential illustrate many features of the Kaluza-Klein modes, as will be discussed.

¹This section is motivated by Randall and Sundrum's analysis of gravitons in [2].

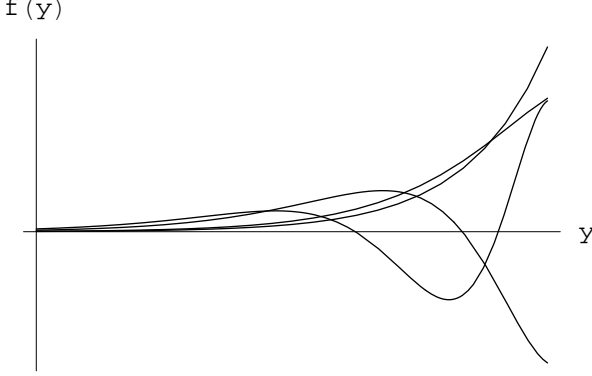


Figure 3: The first four modes of the Kaluza-Klein bulk scalar with $b > 2$. The massless mode now dominates on the IR brane.

2.2.1 Properties of the potential

By including the brane mass potentials and writing $m_\Phi^2 = ak^2 = (b^2 - 4b)k^2$, the complete potential is

$$V(z) = \frac{(15 - 16b + 4b^2)k^2}{8(k|z| + 1)^2} - \left(\frac{3}{2} - b\right)k \left[\delta(z) - \frac{1}{k|z^*| + 1} \delta(z - z^*) \right]. \quad (23)$$

This potential is plotted in Figs. 4-6 for various values of b .

It is useful to apply techniques from quantum mechanics to analyze this potential. The localization of the zero mode (now we're considering the g_n) can be determined by considering the shape and relative strength of the wells located at the UV and IR branes. For example, for $b < 3/2$, we note the δ -well located at the UV brane. A δ -well supports a single bound state, thus we conclude that g_0 will be localized toward the UV brane. The higher energy (massive) modes will be localized in the well bounded by the $\sim 1/z^2$ potential and the δ -barrier located on the IR brane, which is consistent with Eq. 13. To determine the localization of the f_n (specifically f_0) we multiply by the exponential factor in Eq. 17. Thus, we see that for $b < 0$, the zero mode of the f_n is localized on the UV brane and for $0 < b < 3/2$, localized on the IR brane. The massive modes, however, are always localized on the IR brane for $b < 3/2$.

At $b = 3/2$, we find that the potential vanishes, thus g_0 is necessarily completely delocalized, and we recover the correct expression for f_0 localized on the IR brane. Perhaps the most striking feature of the potential is its behavior at $b = 2$. From (23), the $\sim 1/z^2$ piece is minimized at $b = 2$. Calculating the coupling to the IR brane for the massless mode we yield

$$\sqrt{\frac{2(b-1)k}{e^{2(b-1)k\pi r} - 1}} e^{bky} \Big|_{y=\pi r, b=2} = \sqrt{\frac{2k}{e^{2k\pi r} - 1}} e^{2k\pi r}. \quad (24)$$

We take the limit that $k\pi r \gg 1$ so indeed $e^{2k\pi r} \gg 1$. Thus

$$f_0(\pi r)|_{b=2} \approx \sqrt{2k} e^{k\pi r}. \quad (25)$$

The massive mode coupling to the IR brane can be found as well. From (13) and the normalization condition (5), we find the approximate expression for the same assumptions as above that

$$N_n \approx \frac{\pi m_n}{\sqrt{2k}} Y_{\alpha \pm 1} \left(\frac{m_n}{k} e^{k\pi r} \right). \quad (26)$$

Inserting this expression into Eq. (13) and making the necessary cancellations results in

$$f_n(\pi r) = \frac{\pi m_n}{\sqrt{2k}} \left[J_\alpha \left(\frac{m_n}{k} e^{k\pi r} \right) Y_{\alpha \pm 1} \left(\frac{m_n}{k} e^{k\pi r} \right) - J_{\alpha \pm 1} \left(\frac{m_n}{k} e^{k\pi r} \right) Y_\alpha \left(\frac{m_n}{k} e^{k\pi r} \right) \right] e^{2k\pi r}. \quad (27)$$

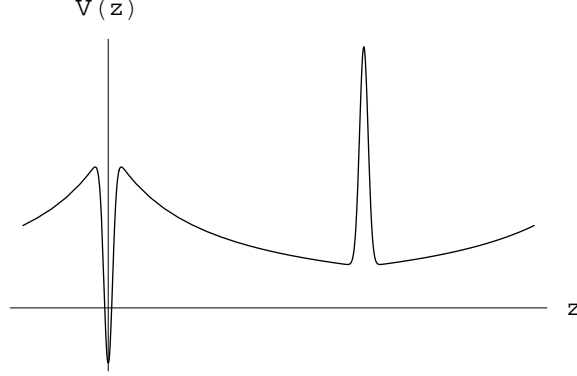


Figure 4: Plot of the scalar potential for $b < 3/2$, the + fermion potential for $c < 0$ and the - fermion potential for $c > 0$.

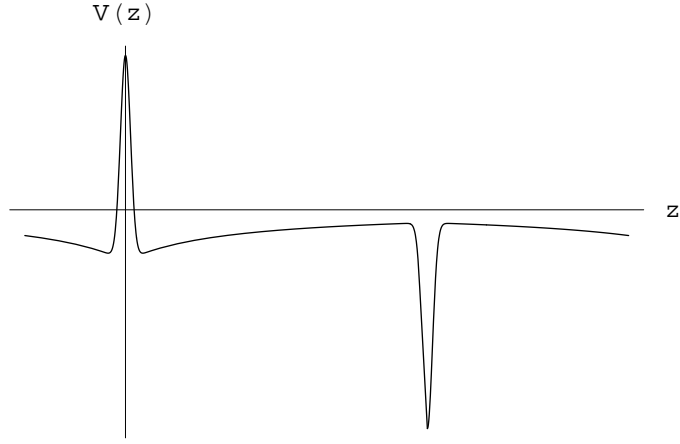


Figure 5: Plot of the scalar potential for $3/2 < b < 5/2$, the + fermion potential for $0 < c < 1$ and the - fermion potential for $-1 < c < 0$.

Noting the Bessel identity

$$J_\alpha\left(\frac{m_n}{k}e^{k\pi r}\right)Y_{\alpha\pm 1}\left(\frac{m_n}{k}e^{k\pi r}\right) - J_{\alpha\pm 1}\left(\frac{m_n}{k}e^{k\pi r}\right)Y_\alpha\left(\frac{m_n}{k}e^{k\pi r}\right) = \frac{2k}{\pi m_n e^{k\pi r}}, \quad (28)$$

we find the coupling of the massive modes to the IR brane to be (for any value of b and n)

$$f_n(\pi r) \approx \sqrt{2k}e^{k\pi r} \quad (29)$$

which is the same coupling as the massless mode! It is as if the information concerning the coupling is preserved in this Schrödinger formulation. In fact, other remarkable phenomena occur when $b = 2$, as will be discussed in the next section. Finally, for $b > 2$, we note that the massless and massive modes remain localized on the IR brane, with the massless coupling only increasing with b .

2.3 Holography

The AdS/CFT correspondence is different with regards to what is usually thought when two theories are considered equivalent. Here, there is no scattering matrix for either the AdS theory or the CFT, for example,

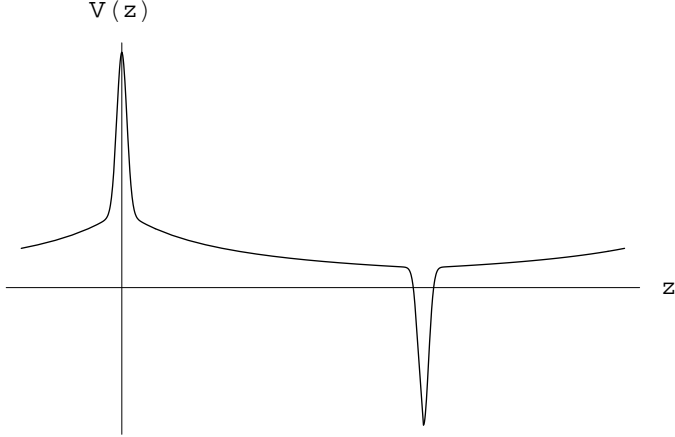


Figure 6: Plot of the scalar potential for $5/2 < b$, the + fermion potential for $c > 1$ and the - fermion potential for $c < -1$.

and so no predictions of physical phenomena can be made to compare the theories[4]. What we can do is compute the correlation functions and observe that in certain limits, the 5D theory agrees with the conformal symmetry. The equivalence is more subtle with each CFT operator \mathcal{O} corresponding to a 5D bulk field φ . The 4D boundary field φ_0 of the AdS (in the general case, taken at $y = -\infty$) acts as a source for the operator \mathcal{O} defining unique equations of motion in the bulk. For completeness, the AdS/CFT can be formulated as[3]

$$\int \mathcal{D}\varphi_{CFT} e^{-S_{CFT}[\varphi_{CFT}] - \int d^4x \varphi_0 \mathcal{O}} = \int_{\varphi_0} \mathcal{D}\varphi e^{-S_{bulk}[\varphi]} \equiv e^{iS_{eff}[\varphi_0]}, \quad (30)$$

with S_{CFT} the CFT action, φ_{CFT} the CFT fields and S_{bulk} the 5D action.

With the RS1 model, however, the extra dimension is no longer infinite, and so the holography changes from the general case. With the addition of the UV brane at $y = 0$, conformal invariance of the CFT is broken at the UV scale ($\sim M_{Pl}$), resulting in the source field φ_0 becoming dynamical. Below the UV scale, however, the theory remains conformal. Including the IR brane at $y = \pi r$ now breaks low energy ($\sim M_{Pl}e^{-k\pi r} \approx \text{TeV}$) conformal invariance, with particle bound states appearing in the CFT. With the two branes in place, the source field is elementary (that is, point-like with no additional structure) below the UV scale and the particles in the CFT are composite (containing additional, underlying structure) above the IR scale. In this regime, the holographic equivalence now takes on its familiar definition with the two theories having the same S-matrices and particle spectra[4].

From the general bulk scalar solution (Eq. (13)), we can determine the correlator $\Sigma(p)$ by taking functional derivatives of the effective boundary action S_{eff} with respect to φ_0 . $\Sigma(p)$ contains the pure CFT correlator $\langle \mathcal{O} \mathcal{O} \rangle$. The correlator is thus given by[3]

$$\Sigma(p) = \frac{k}{g_\varphi^2} \frac{pL_0(I_{\alpha\pm 1}(pL_0)K_{\alpha\pm 1}(pL_1) - I_{\alpha\pm 1}(pL_1)K_{\alpha\pm 1}(pL_0))}{I_\alpha(pL_0)K_{\alpha\pm 1}(pL_1) + I_{\alpha\pm 1}(pL_1)K_\alpha(pL_0)}, \quad (31)$$

where L_0, L_1 are the locations of the UV and IR branes, respectively, $\alpha \pm 1 = |b - 2| \pm 1$ and g_φ is a 5D expansion parameter with $\dim[1/g_\varphi^2] = 1$. By taking appropriate limits of $\Sigma(p)$, we can learn about the CFT correlator $\langle \mathcal{O} \mathcal{O} \rangle$. Taking the IR brane to infinity ($L_1 \rightarrow \infty$), we note from the holography that conformal symmetry breaking is negligible at the IR brane because the effective energy on that brane is zero. Then, the leading non-analytic term of $\Sigma(p)$ (containing Γ -functions or logarithms) is interpreted as the CFT correlator $\langle \mathcal{O} \mathcal{O} \rangle$. Because $\Sigma(p)$ and $\langle \mathcal{O} \mathcal{O} \rangle$ differ in only analytic terms, the poles of each coincide and thus the poles of the correlator $\Sigma(p)$ correspond to the KK particle spectrum.

The analytic terms are also of interest since they are not subtracted away as would be the case with an unbounded energy scale. With the finite cutoff due to the UV brane, these analytic terms are interpreted as kinetic or mass terms of the dynamic source field φ_0 . In this section, we analyze two branches, $b < 2$ and $b > 2$, in which the zero mode is localized on the UV and IR branes, respectively, as well as studying the correlator and its consequences.

2.3.1 $b < 2$ branch

We first study the KK modes in the bulk. The massless particle in the dual theory is elementary for $b \ll 2$ as the zero mode f_0 is both weakly coupled to the IR brane and localized on the UV brane. Even with $0 < b < 2$, where the bulk massless mode is localized on the IR brane, the massless particle in the dual theory remains elementary, however, strong mixing between the elementary and composite dual pictures exists for b near 2. Returning to the Schrödinger picture, we note that irrelevant mixing (elementary interpretation) occurs when the $\sim 1/z^2$ well is positive. Strong mixing occurs when the $\sim 1/z^2$ well is negative as it is a weak well in comparison to the δ -barrier on the UV brane (Fig. 5). The massless mode dual remains elementary in this branch as the coupling to the IR brane is always weaker than the massive modes.

Examining the correlator in the limit that $L_0 \rightarrow 0$ and $L_1 \rightarrow \infty$ results in the expression

$$\Sigma(p) \simeq -\frac{2k}{g_\varphi^2} \left[\frac{1}{1-b} \left(\frac{pL_0}{2} \right)^2 + \left(\frac{pL_0}{2} \right)^{4-2b} \frac{\Gamma(b-1)}{\Gamma(2-b)} + \dots \right], \quad (32)$$

valid for non-integer b where the expression for integer b will contain logarithms. We see that the analytic term is quadratic in p , thus we interpret φ_0 as a massless source field. By the holography, for irrelevant mixing of the elementary and composite sectors, the zero mode is, to good approximation, dual to the source field φ_0 . From the non-analytic piece of $\Sigma(p)$ we determine $\langle \mathcal{O}\mathcal{O} \rangle$, and, interestingly, the dimension of the operator \mathcal{O} as

$$\dim \mathcal{O} = 2 + \alpha = 4 - b. \quad (33)$$

Important to note is that $\dim \mathcal{O}$ is minimized when $b = 2$ (Fig. 5), exactly where the $\sim 1/z^2$ well is minimized, providing a guide to when the mixing is strongest.

2.3.2 $b > 2$ branch

Returning again to the KK modes in the bulk, we note that the dual interpretation of the zero mode f_0 is now composite as it is both localized on the IR brane and more strongly coupled than the massive modes to the IR brane as illustrated in Fig. 3. Again, strong mixing between the elementary and composite pictures exist near $b = 2$, where the $\sim 1/z^2$ well is negative. The mixing is irrelevant when the $\sim 1/z^2$ well is positive, just as we observed in the $b < 2$ branch as there only exists a well on the IR brane (see Fig. 6). Indeed, for $b \gg 2$, the zero mode dual is composite.

The correlator in this branch in the limit that $L_0 \rightarrow 0$ and $L_1 \rightarrow \infty$ is

$$\Sigma(p) \simeq -\frac{2k}{g_\varphi^2} \left[(b-2) + \left(\frac{pL_0}{2} \right)^2 \frac{1}{b-3} + \left(\frac{pL_0}{2} \right)^{2b} \frac{\Gamma(3-b)}{\Gamma(b-2)} + \dots \right], \quad (34)$$

again valid for only non-integer b . The analytic piece now both contains a kinetic term and a mass term, thus we interpret φ_0 as a massive source field. In the low energy limit in the expansion of $\Sigma(p)$, we find a pole, indicating that the CFT contains a massless mode at low energies which is consistent with the holographic interpretation. The dimension of the operator \mathcal{O} , again determined from the non-analytic piece of $\Sigma(p)$ is

$$\dim \mathcal{O} = 2 + \alpha = b, \quad (35)$$

consistent with the $b < 2$ branch. Again, we note that when $b = 2$, $\dim \mathcal{O}$ is minimized as is the $\sim 1/z^2$ well in the Schrödinger picture.

The Schrödinger picture provides a very visceral guide to the holographic theory. We have seen that an elementary analysis, using only tools learned in an undergraduate quantum mechanics class, can yield information of the dual interpretation of the bulk massless mode.

3 Fermion Field in 5D Bulk

3.1 Kaluza-Klein Modes

We now turn our attention to a fermion field in AdS_5 ². The 5D action of a massive fermion is[6]

$$S = \int d^5x \sqrt{g} [i\bar{\Psi}\Gamma^M \nabla_M \Psi - m_\Psi \bar{\Psi}\Psi]. \quad (36)$$

In warped space, the gamma matrices are $\Gamma^M = e_A^M \gamma^A$, with e_A^M the inverse funfbien defined by $g_{MN} = e_M^A e_N^B \eta_{AB}$ and $\gamma^A = (\gamma^a, -i\gamma^5)$ the familiar Dirac gamma matrices. The covariant derivative in warped space for a free fermion is given by $\nabla_M = \partial_M + \omega_M$, where ω_M is the spin connection. The spin connection is necessary to make the kinetic term of the Lagrangian invariant under a general coordinate transformation. In the RS1 metric, the spin connection is given by $\omega_M = -i\text{sgn}(y) \frac{k}{2} e^{-k|y|} \gamma_M \gamma^5$. As the Lagrangian must be even under orbifold symmetry, because $\bar{\Psi}\Psi$ is necessarily odd, the fermion mass, m_Ψ , must too be odd which we take as[3]

$$m_\Psi = ck[\text{sgn}(y) - \text{sgn}(y - \pi r)], \quad (37)$$

with c some dimensionless constant.

To analyze the fermion, we separate it into left- and right-handed components such that $\Psi = \Psi_+ + \Psi_-$ and that $\gamma_5 \Psi_\pm = \pm \Psi_\pm$. Substituting this into Eq. (36) yields the coupled equations of motion for the components

$$ie^{k|y|} \gamma^\mu \partial_\mu \Psi_\pm \pm 2k\text{sgn}(y) \Psi_\mp \mp \partial_5 \Psi_\mp - m_\Psi \Psi_\mp = 0. \quad (38)$$

As with the scalar, we make a separation of variables ansatz with

$$\Psi_\pm(x, y) = \sum_{n=0}^{\infty} \psi_\pm^{(n)}(x) h_\pm^{(n)}(y), \quad (39)$$

where $\psi_\pm^{(n)}$ are the Kaluza-Klein modes with $i\gamma^\mu \partial_\mu \psi_\pm^{(n)} = m_n \psi_\pm^{(n)}$ and the $h_\pm^{(n)}$ is the profile of the Kaluza-Klein modes in the bulk. We can then decouple the equations of motion, resulting in second order differential equations for the $-$ and $+$ components. While not discussed further here, the bulk solutions are discussed in greater detail in [3, 6, 7, 8].

3.2 Schrödinger Equation Formulation

From the coupled equations of motion, we again change variables from y to z , with z defined as in (17) to find the Schrödinger equation for fermions:

$$\left(-\frac{1}{2} \partial_z^2 + \frac{2k^2 c(c \pm 1)}{(k|z| + 1)^2} \mp ck \left[\delta(z) - \frac{1}{k|z^*| + 1} \delta(z - z^*) \right] \right) h_\mp^{(n)} = \frac{m_n^2}{2} h_\mp^{(n)}, \quad (40)$$

where z^* is defined as before and, in an abuse of notation, $h_\pm^{(n)}(y) = h_\pm^{(n)}(z)$. The corresponding potential for fermions is

$$V_\mp(z) = \frac{2k^2 c(c \pm 1)}{(k|z| + 1)^2} \mp ck \left[\delta(z) - \frac{1}{k|z^*| + 1} \delta(z - z^*) \right]. \quad (41)$$

The potential is plotted for both the $-$ and $+$ fermion for various values of c in Figs. 4-6. Of note is that the behavior of the potential for the $-$ and $+$ fermion is symmetric about $c = 0$, that is $V_+(z)|_c = V_-(z)|_{-c}$. Both potentials vanish when $c = 0$, and the $\sim 1/z^2$ piece assumes its minimum value at $\pm 1/2$ for the $+$ and $-$ fermion, respectively, which has important consequences when considering the holography for fermions. Solving (40) for the bulk zero mode, we find that

$$h_\mp^{(0)} \propto (k|z| + 1)^{\mp c}, \quad (42)$$

²So that the holography analysis is the same as [6], we change our metric to be positive in the time component, rather than negative.

which produces the correct localization of the mode as would be expected from the location of the δ wells of the potentials. As discussed in the next section, the Schrödinger formulation is useful for analyzing fermion holography, which is much richer, and perhaps more relevant for phenomenology, than that discussed for scalars.

3.3 Holography

We follow the holographic analysis of [6] and note that from the action (36) because it only contains a first derivative, we are only able to fix one of Ψ_- , Ψ_+ on the UV brane, but not both. We follow their lead, fixing Ψ_- on the UV brane with $\Psi_-|_{y=0} \equiv \Psi_-^0$. Then, Ψ_-^0 is the source field for an operator \mathcal{O}_+ as discussed in the scalar holography section. The case where Ψ_+ is fixed is considered in [6] and a simple correspondence exists between the two cases. Thus we will not discuss it here. With this choice of Ψ_- fixed, the variational principle requires that another term must be added to the action to eliminate the UV boundary term containing $\delta\Psi_+$, which is not zero. The effective action can be computed, from which we determine the correlator $\Sigma(p)$. The correlator for the fermion case with a Ψ_-^0 source is

$$\Sigma(p) = \frac{k}{g_\Psi^2 L_0} \frac{p}{\not{p}} \frac{J_{\alpha-1}(pL_0)Y_\beta(pL_1) - J_\beta(pL_1)Y_{\alpha-1}(pL_0)}{J_\alpha(pL_0)Y_\beta(pL_1) - J_\beta(pL_1)Y_\alpha(pL_0)}, \quad (43)$$

where $\alpha = c + 1/2$ for the fermion case. The value of β is dependent on the IR brane boundary condition; for the Dirichlet condition on Ψ_- (Ψ_+) on the IR brane, $\beta = \alpha$ ($\beta = \alpha - 1$). Again, the non-analytic piece of $\Sigma(p)$ is interpreted as the pure CFT correlator $\langle \mathcal{O}_+ \mathcal{O}_+ \rangle$ and the poles of $\Sigma(p)$ and $\langle \mathcal{O}_+ \mathcal{O}_+ \rangle$ coincide as the two functions only vary by analytic terms.

Returning to the action, we note that the cancellation of the boundary term in the KK approach is accomplished by Dirichlet conditions on either the $-$ or $+$ fermion on the UV brane. The conditions, $\Psi_-|_{UV} = 0$ or $\Psi_+|_{UV} = 0$, correspond to odd or even parity of the Ψ_- fermion about the UV brane. The choice of Ψ_-^0 as the source field corresponds to having an even Ψ_- in the KK approach. This choice is arbitrary since the added boundary term in the action destroys any necessary constraint on the parity of Ψ_- . While not important for our analysis, if instead we desire the dual description of Ψ_- odd, we must add a term to the UV brane Lagrangian containing a Lagrange multiplier constraint which happens to be an extra $+$ fermion[6]. In the Schrödinger formulation, Dirichlet conditions ($\Psi_\pm = 0$) on the branes represent the elimination of the corresponding δ potential so the boundary conditions are met. Consideration of the parity of the fermions at both boundaries is important for the AdS/CFT holographic interpretation and existence of massless bound states in the CFT. We now turn our attention to this, first discussing the region where $c \geq 1/2$.

3.3.1 $c \geq 1/2$

The holographic Lagrangian consists of the CFT Lagrangian, the UV boundary Lagrangian and the dynamical source field coupled to the strongly interacting $+$ CFT operator. The CFT chiral operator, \mathcal{O}_+ has dimension[3, 6]

$$\dim \mathcal{O}_+ = 3/2 + |c + 1/2|, \quad (44)$$

which we note, consistent with the result for the scalar, is minimized when the $-$ fermion potential³ is also minimized at $c = -1/2$. From the Lagrangian, we can see that the coupling between the source field Ψ_-^0 and the CFT operator is irrelevant for $c > 1/2$ and marginal for $c = 1/2$. Again, this is consistent with the Schrödinger formulation, as, for $c \geq 1/2$, the $+$ fermion potential contains a δ well at the IR brane and thus the $+$ massless mode necessarily is localized there.

We can also consider two possible parity cases on the UV and IR branes for the Ψ_- and Ψ_+ and study the CFT massless mode for each case. As discussed in [6], Ψ_- odd on the UV brane corresponds to the source Ψ_-^0 frozen and acting as a classical source coupled to the CFT. For Ψ_- odd at both boundaries (Ψ_+ even),

³We take the $-$ fermion potential as it is the source of the operator \mathcal{O}_+ .

the CFT contains a massless bound state as the equivalence just noted suggests. The quantum mechanical picture is consistent, as the $-$ potential contains no δ wells (as they are eliminated by the parity of Ψ_-) and hence no massless KK mode while the $+$ potential has a δ well on the IR brane corresponding to a $+$ massless CFT mode as the KK zero mode is localized on the IR brane. If instead we take Ψ_- to be even at both boundaries (Ψ_+ odd) no massless CFT mode exists, which is again consistent with the quantum mechanical formulation. The $+$ potential contains no δ wells and the $-$ potential only has a δ well on the UV brane, consistent with an elementary source field Ψ_-^0 .

3.3.2 $-1/2 < c < 1/2$

In this region, the analysis of the previous section applies here as well, with the massless CFT mode still $+$. The coupling of the source and the $+$ CFT operator is relevant, hence the mixing of Ψ_-^0 and the CFT is always important. Strong mixing between the elementary and composite pictures of the dual interpretation of the KK modes exists, consistent with the potentials of the $-$ and $+$ fermions both negative in this region. As with the scalar, the negative potential warns us that the interpretation of the holography from the quantum mechanical picture is not as simple as the other regions.

3.3.3 $c \leq -1/2$

The holography in this realm is quite different than the holography for the previous cases. Taking the limit that $L_0 \rightarrow 0$ and $L_1 \rightarrow \infty$ and expanding in Euclidean momenta, the correlator becomes[6]

$$\Sigma(p) \simeq i\psi \frac{k}{g_\Psi^2} \left[\frac{2|\alpha|}{(pL_0)^2} + \frac{1}{2(|\alpha|-1)} - \frac{(pL_0)^2}{8(|\alpha|-2)(|\alpha|-1)^2} + 2^{2\alpha+1}(pL_0)^{(2|\alpha|-2)} \frac{\Gamma(1+\alpha)}{\Gamma(-\alpha)} + \dots \right]. \quad (45)$$

The pole in this expansion is a non-analytic term, and cannot be cancelled by the inclusion of some counterterm, nor can it be ascribed to the exchange of a massless bound state in the CFT as conformal symmetry has been restored with $L_1 \rightarrow \infty$. Thus, the holographic interpretation of the correlator in the expansion above must consist of some extra elementary degree of freedom. This new field (χ_+) couples to Ψ_-^0 and both become massive, playing a similar role to the field added to make Ψ_-^0 odd as both forbid the source from propagating at low energies.

We again take the same parity assignments of Ψ_- and Ψ_+ to consider the massless spectrum of the holography. As before, with the $-$ fermion odd at both branes, we expect a $+$ massless mode, however, this mode is not a CFT bound state but rather the new field χ_+ . The CFT is not chiral and there is no massless bound state, as is anticipated from the quantum mechanical picture, as the $-$ potential contains no δ wells and the $+$ potential only has a δ well on the UV brane. The elementary field here is the new field χ_+ , and not the CFT source Ψ_-^0 .

We now consider Ψ_-^0 even at both branes. Decoupling χ_+ from the CFT by taking the low energy limit sending first $L_0 \rightarrow 0$, a massless pole is observed in the correlator corresponding to the $-$ fermion with even parity at both branes. In the Schrödinger formulation, now the $+$ potential contains no δ wells while the $-$ potential contains a δ well on the IR brane, corresponding to the $-$ massless CFT bound state.

As a final discussion of fermion holography, we consider Yukawa couplings of Standard Model fermions. In the bulk, Standard Model fermions are identified as the massless mode of one of the $+$ or $-$ components of the corresponding 5D Dirac spinor Ψ [3], say Ψ_- . 4D Standard Model Yukawa interactions are then promoted to 5D interactions in the bulk⁴. For each Standard Model fermion, values of c correspond to 4D Yukawa couplings; for light fermions $c > 0$ and for heavy fermions $c < 0$. In the case of the electron, $c \simeq 0.64$, and so the KK zero mode is localized on the UV brane, giving the electron an elementary interpretation in the dual picture. The Schrödinger potential for $c = 0.64$ is consistent for the $-$ component of Ψ for the electron as the δ well is located on the UV brane. For the top quark, $c \simeq -0.5$, and thus the KK zero mode is localized on the IR brane, with the $-$ top quark a composite state in the holography. The δ well for the $-$ potential with

⁴Or wherever the Higgs is located.

this value of c is located on the IR brane, as we expect from the localization of the KK zero mode. However, as the bulk potential well is minimized at $c = -1/2$, the dual interpretation of the top quark would be part elementary, part composite. The + case is the opposite, with the massless KK modes localized on the IR and UV branes for the electron and top quark, respectively, as compared to the - case. The other fermions then have c values between the top quark and electron. This interpretation of the Yukawa couplings in the AdS theory reduces the fermion mass problem to determining the values of c , which are all of order unity as compared to the 4D Yukawa coupling which may be as small as 10^{-6} for the electron and as large as 1 for the top quark⁵.

4 Conclusion

The Schrödinger formulation is a surprisingly effective tool for determining important holographic features of the AdS/CFT correspondence. Here, we presented another “entry” into the “dictionary” of the correspondence which is simply considering the quantum mechanical potential of the field. The results found here for both the scalar and fermion fields in the bulk can be extended to gauge bosons and the graviton, the latter of which is considered in [2]. As expected, the potentials for these fields exhibit the exact same behavior as witnessed for the scalar and fermion. This observation indicates just how rich the correspondence is.

Acknowledgements

I would like to thank Brian Batell who suggested the project and who provided invaluable guidance throughout the summer; Tony Gherghetta, my faculty advisor on the project, for his helpful discussions; Serge Rudaz and Wendy Tschampl for their hard work at making this a wonderful REU experience; and the National Science Foundation grant NSF/PHY-0139099 which sponsored my research.

References

- [1] L. Randall and R. Sundrum, *Phys. Rev. Lett.* **83**, 3370 (1999) [arXiv:hep-ph/9905221].
- [2] L. Randall and R. Sundrum, *Phys. Rev. Lett.* **83**, 4690 (1999) [arXiv:hep-th/9906064].
- [3] T. Gherghetta, arXiv:hep-ph/0601213.
- [4] N. Arkani-Hamed, M. Poratti, L. Randall, *JHEP* **0108**, 017 (2001) [arXiv:hep-th/0012148].
- [5] W. Goldberger and M. Wise, *Phys. Rev. D* **60**, 107505 (1999) [arXiv:hep-ph/9907218].
- [6] R. Contino and A. Pomarol, *JHEP* **0411**, 058 (2004) [arXiv:hep-th/0406257]
- [7] Y. Grossman and M. Neubert, *Phys. Lett. B* **474**, 361 (2000) [arXiv:hep-ph/9912408]
- [8] T. Gherghetta and A. Pomarol, *Nucl. Phys. B* **586**, 141 (2000) [arXiv:hep-ph/0003129]

⁵The 5D AdS theory has also been shown to produce small Dirac masses for neutrinos, consistent with current measurements[3, 7].

Nuclear Recoil Band Definitions and CDMS Simulations

Undergraduate Student

Katrina Legursky
Benedictine College
Atchison, KS

Advisor

Professor Priscilla Cushman
University of Minnesota
Minneapolis, MN

Nuclear Recoil Band Definitions and CDMS Simulations

Katrina Legursky
Benedictine College, Atchison, KS

Advisor: Priscilla Cushman
University of Minnesota, Minneapolis, MN

Abstract

The CDMS project is a collaboration experiment that is actively searching for dark matter candidates called WIMPs, or Weakly Interacting Massive Particles. My part in this project has been twofold. My primary task was to define a data cut using calibration data that defines the range in which WIMPs are expected to interact. We have two separate calibration data runs, and I determined that it was feasible to combine the data to define the nuclear recoil bands. These bands are important to distinguish between gamma and electron recoil background from neutron and WIMP interactions. I also worked on a simulation that is trying to reproduce results from the CDMS runs at the Stanford Underground Facility(SUF) to check the simulation run for the deeper Soudan site. My primary task with the simulation was to extract information from multiple data sets as they were produced while we tried to get the simulation to work properly.

Background about the Experiment

Most people think of the universe only in terms of what is visible. However, evidence from the Big Bang theory and Newtonian physics suggests that the visible universe accounts for only a small portion of the universe. Some of the earliest observational evidence that suggests the existence of dark matter comes from the motion of galaxies. Galaxies mostly appear as thin disks of stars and dust that rotate about the galactic core. Stars farthest from the galactic core are moving much faster than classical theory allows. In order for this to occur, there has to be much more mass than what is visible, suggesting a dark matter halo around galaxies with the visible matter concentrated in a disk in the center. If this is true, the Earth would always be passing through a flux of dark matter particles.

This so-called dark matter has not yet been directly detected, and there are several candidates for what a dark matter particle would be like. The one we are looking for in the CDMS experiment is non-baryonic cold dark

interacting massive particle. A particle similar to this is also predicted by super symmetric theory, which postulates that every particle has a superparticle. These superparticles break down into other superparticles, so there must be a lightest superparticle. This might be the WIMP particle. Its weakly interacting nature allows it to be detected through its interactions with ordinary matter. The CDMS experiment was designed to measure the recoil energy of an interaction with germanium and silicon crystals.

The CDMS detectors are located 2341 feet underground at the Soudan mine in northern Minnesota. This location greatly decreases cosmic ray induced muon flux coming into the detectors which would produce neutrons that can be confused with the WIMP particle. Currently there are five towers of six detectors each, and the experiment has just begun a new run, Run 123. The detectors, called Z-sensitive ionization and phonon detectors, or ZIPs, are made up of either silicon or germanium. They collect two pieces of data from incident particles

matter, also known as the WIMP, a weakly

REU 2006 Page 65

that interact with the crystals. The first, the phonon energy, is the vibrational energy produced by a collision of an incident particle with a nucleus in the crystal lattice. The second is the ionization energy which is caused by the freeing of electrons after a collision. On each detector, there is a charged plate and a grounded plate, so that there is an electric field in the crystal lattice. The electrons move toward the electrode and produce the ionization signal.

In order for the ZIPs to detect these tiny interactions, they must be kept very cold. This is done through the use of a dilution refrigerator, or cryostat. The dilution refrigerator itself cools down to a temperature of 20mK. Its outside layer is a liquid nitrogen shield, which takes the apparatus down to 77K. Inside that there is a layer of vacuum, then a liquid helium bath (4K). This can be pumped on with vacuum pumps to decrease the pressure, and therefore the temperature. Inside the liquid helium bath, there is another layer of vacuum, then the 1K pot. Inside the 1K pot, liquid helium exists as a superfluid. Inside this there is a mixing chamber, where ^3He and ^4He exists much like oil and water. The ^3He is pumped out, which disturbs the equilibrium of the mixture. More ^4He is pumped in, and it creates more ^3He to restore equilibrium. This process takes heat, so the more ^3He that is pumped out, the colder it gets. The fridge is connected to the icebox and keeps the detectors at 40mK.

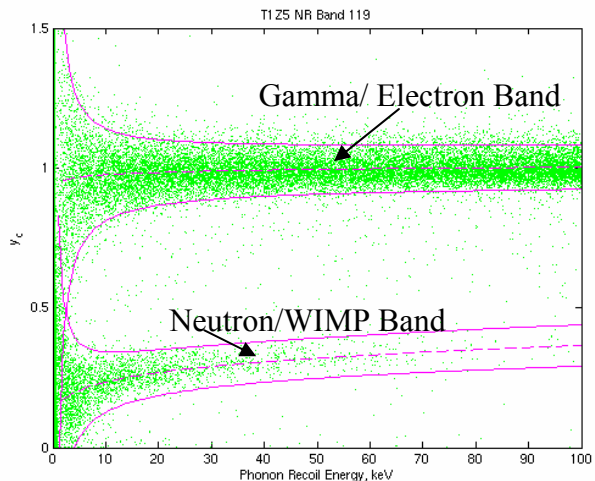
The detectors themselves are located within many layers of shielding. The outermost layer is composed of veto panels. These panels have plastic scintillator inside so when a particle deposits a certain amount of energy in a veto, the event itself is vetoed. Being vetoed means that for a certain small amount of time after a vetoed event, the data can be thrown out. Inside the veto panels there is a layer of polyethylene, then a few layers of lead. Inside the lead there is another layer of polyethylene, and finally some copper then the detectors. This shielding helps get rid of the particles the veto misses.

Nuclear Recoil Band Definitions

In order to effectively search for the WIMP particle, we must know first where to look for it. To the left is a plot of the phonon recoil energy v. the charge yield, which is the two signals we get from the detectors. WIMPs are chargeless particles, so we expect them to interact very similarly to neutrons in the detectors.

By plotting the phonon energy against the charge yield, we can find out where we need to look for these particles. The charge yield is the total charge signal for an event divided by its recoil energy. Because the WIMP particles and neutrons have no charge, we don't expect a large ionization signal from them, so this ratio is smaller. Electrons and gammas, however, should have nearly equal ionization and phonon signals, which puts their ratio at about 1. We place bands around the gamma/electron and neutron/WIMP events so that the electron background can be subtracted and we have a more specific area in which to look for the WIMP particle.

To define the bands, we use calibration data from the two CDMS runs, 118 and 119, in which radioactive Cf-252 and Ba-133 sources



shoot neutrons and gammas at the detectors. The first step in defining the bands is to break up the gamma and neutron events into energy bins from which we can see a Gaussian distribution of each and determine the mean. I

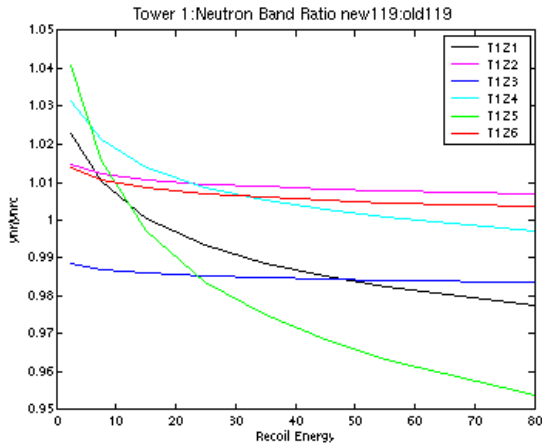
used energy bins of [5 10 20 30 40 50 60 100] keV. Once we have a mean from each energy bin, we put them all together and fit a function that goes through each mean. The following are the functions that define the mean and band width:

$$\text{mean} = a * (Er)^b / Er$$

$$\text{bandwidth} = \text{sigma} = c * Er + d$$

Where Er is the phonon recoil energy and a , b , c , and d are the variables determined to fit the data.

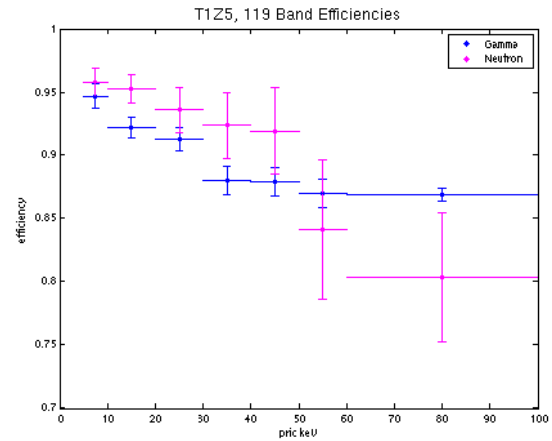
Once the cut is defined, it was necessary to do many comparisons of the results in order to see if they made sense and if it would be possible to combine the calibration data from run 118 and run 119. The first comparison I made was of my new bands to some previously calculated bands to see how they lined up. Overall, the new bands were fairly consistent with the previous bands with a few exceptions. The gamma bands from T1Z1 changed significantly in both the 118 and 119 recalculation. Also, in run118, the direction of T1Z5's neutron band has shifted with the band reanalysis.



After visual inspection, I make this comparison analytically by taking the ratio of the mean of my new bands to the mean of the existing bands. I attained this ratio by dividing the array into 8 Energy bins(2.5, 7.5, 15, ...keV), and taking the ratio of the means at each point

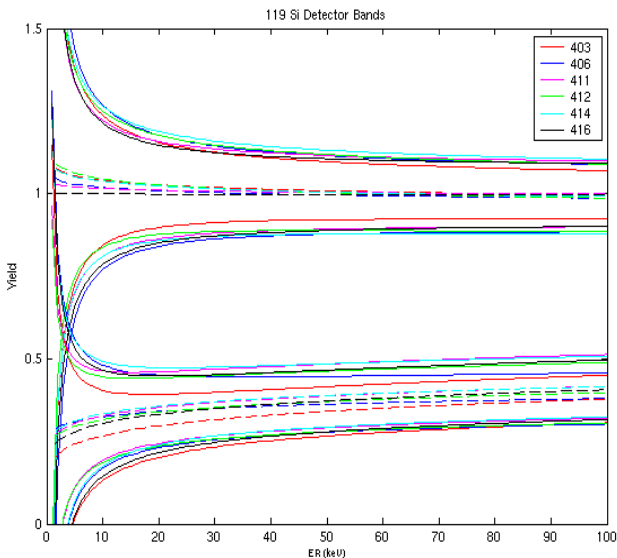
in the array calculated from the old 119 mean and the new 119 mean. Most of the means were within 2% of one another. In the figure above, the means are within 4% of one another.

One important part of creating data cuts is to know how efficient they are, so after a number of cuts are applied, their total efficiency of the data can be known. The efficiency of the band is defined as the number of events within



the bands divided by the number of total events. This allows you to see the percentage of events that are kept within the band. To calculate the efficiencies of the new cuts, first I apply the same data cuts that were originally made when the cuts were defined. I used a different set of data(background data) to calculate the efficiencies to get a better idea of how the cut is actually working. When the cuts were defined, the neutron and gamma events were selected separately, so when I go to calculate the efficiencies I define the neutron and gamma events in the same way. I am then able to apply the bands and determine how many events remain after the bands are applied. It is also necessary to find the uncertainty in this efficiency, which is derived from the Poisson distribution as $\sqrt{(i*t - i^2)/t^3}$, i is the number of events included within the band cut, and t is the total number of events to which the cut is being applied. The uncertainty in the efficiency of the nuclear recoil band is much greater than that of the gamma band at higher energies because there are much fewer neutron events at the

higher energies.



The final check was to plot the bands from all the germanium detectors on one axis and the silicon detectors on another. In principle, the mean of the bands should line up the same for detectors made of the same crystal. For the most part they do, especially at the higher energies.

All of these comparisons and checks I have talked about were repeated for the combined data cut, C89. The whole idea of my little project was to determine whether it was possible to define one cut for both 118 and 119, so when using the bands one does not have to make four separate cuts, it is only necessary to make two. After visual and analytic inspection, I determined that it was safe to combine the data from 118 and 119 to define nuclear recoil bands.

SUF Background Simulation

When one tries to perform a rare event search, it is necessary to take a background count to see how much cosmic radiation must be subtracted from the results. CDMS is one of these experiments, however, it is very well shielded from cosmic radiation. Therefore, it would need much larger periods of background counting than are feasible in order to obtain a good background count. A background count

would not really even work because the whole idea of the project is to identify a new particle, so in a background count, one might be detected and appear as part of the background. One way to obtain a good background count is to run simulations that throw cosmic particles through the rock at the detector setup and see how many events occur and what kind of particles are detected.

A simulation has already been run for the deep Soudan site, but we are now going back and trying to reproduce the results of that simulation. The first CDMS runs were done in a tunnel underneath Stanford's campus with one tower of detectors. Because it is such a shallow site, there is a large neutron background. So we are currently trying to design a Geant4 simulation that will match the Stanford data so we can benchmark the existing Soudan simulation.

The simulation throws muons at a cavern that is surrounded by ten meters of rock. The particles then travel into the experiment assembly and are tracked through 3 separate

Particle Type	# in the cavern	# in the veto	# in the detectors
Muons	538687	57571	16
Muon Neutrinos	101111	23483	0
Electrons	93075	51945	20
Electron Neutrinos	100818	23571	0
Neutrons	75	33	0
Protons	29	27	0
Gammas	100277	29611	10
Pions	90387	51627	20

sensitive detectors. First, the simulation keeps track of how many muons enter the cavern. Then there are 12 veto panels that surround the detectors, and finally, the 6 detectors themselves. Each event has a track number from which one can find all kinds of information about the particle, such as what type it was,

what its kinetic energy is, its position and so forth. My part in working with the simulation was to take the data and extract key pieces of information out of it so we could tell at a glance whether it was behaving correctly or not. Some of this information is listed in the table. You can see that so far there are no neutrons in the detectors, which is due to the short livetime of the data. Once the simulation runs on multiple cpu's for a certain amount of time, the livetime will go up and we should start seeing the neutrons in the detectors. This set of data, however, tried to fix a problem with the kinetic energies of the muon coming into the cavern. In previous data sets, this number was way too high to have been correct, but it has been corrected with this data set. The average muon kinetic energy is 3.53 GeV. Once some of these basic facts are established, it is necessary to see

how many of the neutrons coming in were vetoed. From this data set, 84.6% of the neutrons in the veto panel were vetoed, and 68.2% were vetoed by the muon that produced them. This simulation is a work in progress, so there are no actual conclusions to present.

Acknowledgments

I would like to extend my gratitude to Prisca Cushman for taking me on for this project; Angie Reisetter and Long Duong for all their help and advice while I was working with the data; Sean Corum, Xinjie Qui, and Tao Qian for helping me with little things in the office; the staff at the Soudan mine for helping me while I was down there; Serge Rudaz and Wendy Tschaapl for putting on a great REU program; and the National Science Foundation for providing the funds this summer.

Looking for Signatures of Superconductivity in Laser-Processed Strontium Ruthenate

Undergraduate Student

Gustav E. Rustan
University of Minnesota
Minneapolis, MN

Advisor

Dr. Allen Goldman
University of Minnesota
Minneapolis, MN

Looking for Signatures of Superconductivity in Laser-Processed Strontium Ruthenate

Gustav E. Rustan
University of Minnesota, Morris

University of Minnesota Summer 2006 Physics REU
Advisor: Dr. Allen Goldman

Abstract

Physicists working at Naval Research Laboratory claim to have found signatures of superconductivity at high temperatures in specially processed samples of strontium ruthenate, which is a known superconductor with $T_c \approx 1.5\text{K}$. Three techniques were used to measure the critical temperature, resulting in a range for T_c of 200K to 250K. Another signature of type-II superconductivity, a butterfly curve, was also found, however it was not found directly through $M(H)$ measurements as would be typical. To verify the existence of superconductivity, samples were sent to the University of Minnesota for magnetization measurements. After a series of measurements, it was found that the butterfly cannot be taken as a signature of superconductivity; $M(T)$ data also fail to show signs of superconductivity.

I. Introduction/Background

For any material to be a superconductor, there are two characteristics that it must exhibit: zero dc resistance, and expulsion of magnetic flux, known as the Meissner effect. These characteristics will appear in the material when it has been cooled below a specific temperature, known as the critical temperature, T_c . I will give a brief description of how these important characteristics are detected, and have provided some examples and visual aids as well.

Zero dc resistance is usually measured using a four-probe technique (Fig.1). Starting at a temperature above T_c , a current is applied which runs through the sample. Because at this temperature the sample is a regular conductor, the flow of electrons will be impeded and a potential difference will occur in the sample, measured between $V\pm$. The temperature is then slowly decreased, and the voltage is monitored. For a normal conductor, the voltage (and hence resistance) should decrease linearly with temperature. However, at T_c , the voltage will go to zero very quickly. An example $R(T)$ measurement for YBCO ($T_c = 94\text{K}$) is shown in Fig.1. If zero dc resistance is detected in a material, the next step is to detect the Meissner effect.

To detect the Meissner effect, a Superconducting Quantum Interference Device, SQUID, is used to measure the magnetization of the sample as a function of temperature. The sample is first cooled to a temperature much lower than its T_c . A magnetic field is then

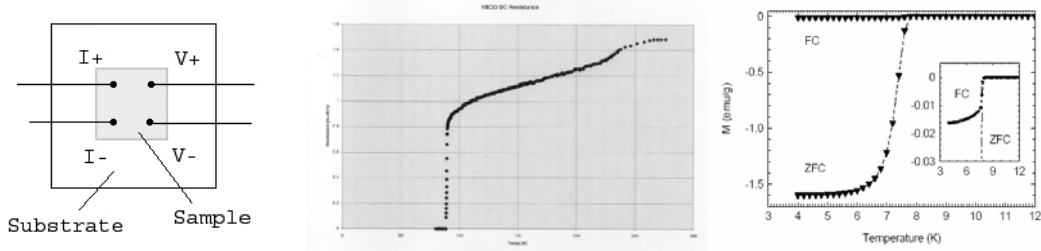


Figure 1: (left) An example of the four probe technique for measuring $R(T)$; (center) $R(T)$ curve for YBCO, $T_c = 94\text{K}$; (right) $M(T)$ curves for $\text{Li}_2\text{Pd}_3\text{B}$, $T_c = 8\text{K}$

applied (10-100 G), and the temperature is slowly increased. In the simplest case (the absence of overlapping ferromagnetism and/or paramagnetism), the magnetization of the sample will have a sign opposite to that of the applied field, indicating diamagnetism. As the temperature approaches T_c , the magnetization will go towards zero, and at temperatures above T_c the magnetization equals zero. An example $M(T)$ curve is given in Fig.1. Note that along with the zero field cooled curve, there is also a field cooled curve, which shows no change in magnetization. This is because applying the field before the sample has entered the superconducting state can result in the trapping of flux.

The $R(T)$ and $M(T)$ measurements apply to both type-I and II superconductors, however, for type-II superconductors there is an additional signature of superconductivity, the “butterfly curve”. The butterfly is a curve of magnetization as a function of applied field, $M(H)$, and can be seen from a material that is in the superconducting state (Fig.2).

The butterfly curve became the primary focus of this investigation of superconductivity in specially-processed strontium ruthenate. Before discussing the measurements and data taken at the University of Minnesota, I will summarize the work and data of the physicists at NRL in sections II and III (Gulian et al., 2005).

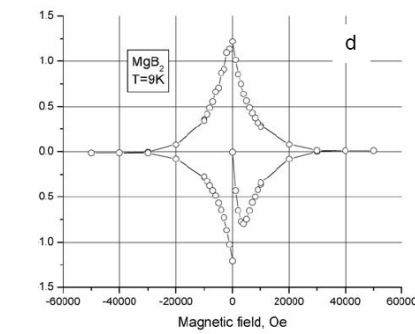


Figure 2: Butterfly curve detected in MgB_2 , $T_c = 39\text{K}$

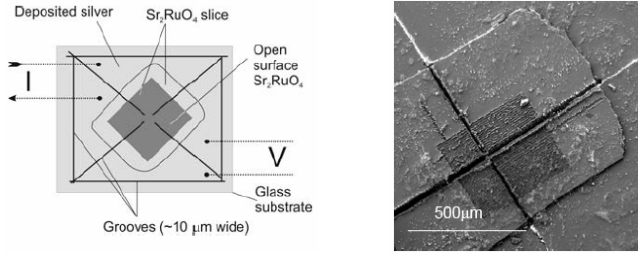


Figure 3: (left) Schematic of processed sample; (right) SEM image of processed sample

II. Preparation and Composition of the Samples

All samples were made from the same strontium ruthenate crystal, which was measured to have a T_c of 1.13K. The samples were peeled from the crystal and polished on opposing plane faces into plates $\sim 25 \mu\text{m}$ thick and 1-3 mm in lateral dimensions. The samples were then glued to a substrate (glass, strontium titanate, or sapphire), and a 3000Å thick layer of silver was deposited on the substrate and strontium ruthenate. Further processing included laser micromachining to separate the internal part of the sample from the edge and define four conductive legs extending from the edge to within 10 μm of the center, and laser ablation to remove the silver from the central part of the sample.

Energy dispersive X-ray spectroscopy was used to determine the composition of the processed samples. The average composition of the top layer of the sample, $\sim 2-4 \mu\text{m}$ thick, was found to be silver doped $\text{Sr}_2\text{RuO}_{6\pm x}$ ($x < 1$), much different than the parent crystal, Sr_2RuO_4 . Diffraction scans also revealed that the processing did not result in chaos, but rather new crystalline substances.

Element	Percent Composition			Average
Strontium	21.50	23.36	22.53	22.46
Ruthenium	10.43	11.51	10.91	10.95
Oxygen	65.98	64.75	65.86	65.53
Silver	2.09	0.38	0.70	1.06

III. Measuring T_c

The critical temperature of the superconducting transition was measured using three different methods, resulting in three different values for T_c : Resistance as a function of temperature, 200K; Magneto-optical imaging, 220K; Magnetization as a function of temperature, 250K. Of the three methods, only R(T) and M(T) have been discussed.

In Fig.4, the z.f.c., 10 G line is the most important M(T) measurement. The shape of the curve is explained as being due to the overlapping of ferromagnetism and diamagnetism. At room temperatures the ferromagnetic signal is strongest, but at 250K the diamagnetic signal

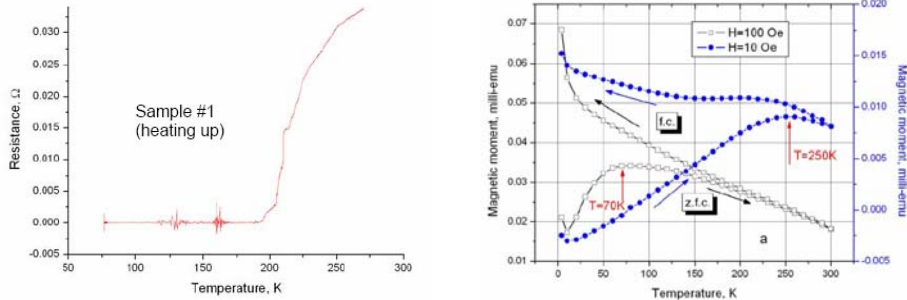


Figure 4: (left) $R(T)$ for the processed sample, $T_c \sim 200$ K; (right) $M(T)$ curves for processed sample, $T_c \sim 250$ K based on 10 G z.f.c curve.

begins to take over, and at low temperatures the diamagnetic signal dominates. With this explanation, 250K would be the onset of the Meissner effect, and thus superconductivity.

The most discussed signature of superconductivity that was found was the butterfly curve, a magnetization vs. applied field curve, which is typical of type-II superconductors within the superconducting state. However, the manner in which the butterfly was produced came under some scrutiny. The butterfly was produced by subtracting the 300K $M(H)$ data, background paramagnetism (see Fig.5), and 4K ferromagnetism from the 4K $M(H)$ data. The reason for the subtractions was that, because of the special processing of the samples, multiple types of magnetism are present and mask the diamagnetism that would indicate superconductivity.

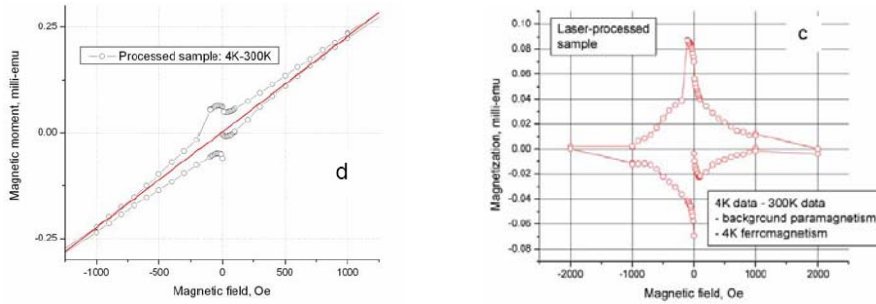


Figure 5: (left) Background paramagnetism; (right) Butterfly curve with all overlapping ferromagnetism and paramagnetism removed

IV. Attempting to Duplicate Measurements

A. Butterfly Curve

The first task was to duplicate the butterfly curve. The following butterfly and two substrates, strontium titanate and glass with a silver layer (without the processed sample), were received from NRL for $M(H)$ measurements. This butterfly was produced simply by subtracting the 200K $M(H)$ data from the 100K $M(H)$ data; in this case the processed sample was on a strontium titanate substrate.

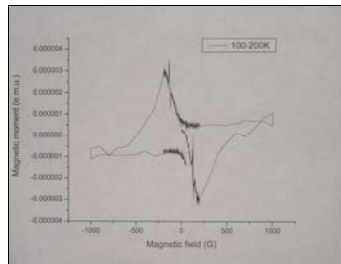


Figure 6: Butterfly produced by subtracting the 200K M(H) curve from the 100K M(H) curve.

M(H) curves were taken for the ordinary substrates to make sure that the butterfly was a result of the processed sample, and not the substrates themselves. Subtractions for the strontium titanate and glass samples clearly do not reproduce the butterfly, as can be seen in Fig.7. When M(H) data was taken for one of the processed samples, however, the 100-200K subtraction clearly does reproduce the butterfly.

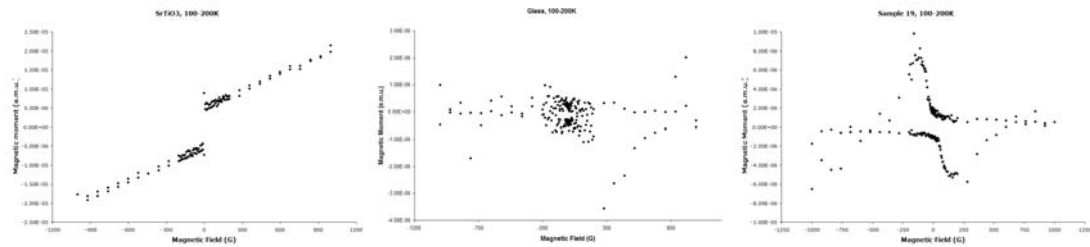


Figure 7: 100-200K M(H) subtraction curves for (left) strontium titanate; (center) glass with silver layer; (right) processed sample #19

After reproducing the initial butterfly, we proceeded to take M(H) measurements at 220 through 300K, in increments of 20K. We then subtracted the 300K data from each of the 220K through 280K data. The idea was that if the butterfly was actually a signature of superconductivity, then it should stop appearing at temperatures above 250K, so as to be consistent with M(T) data. However, as can be seen in Fig.8, the butterfly is still present at 280K. This would suggest that the butterfly does not represent superconductivity.

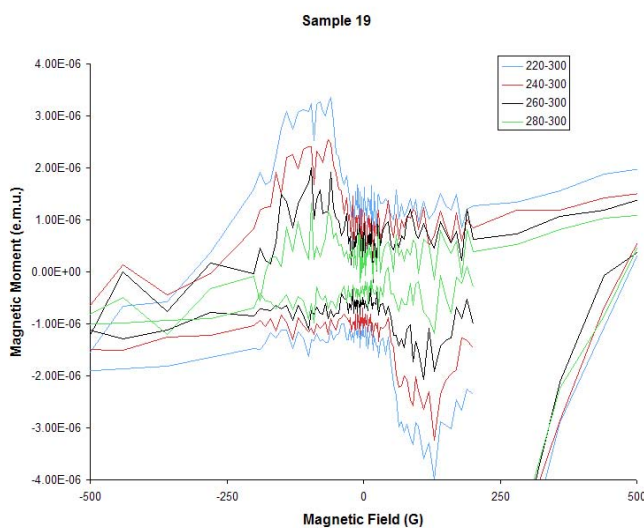


Figure 8: Composite plot of M(H) subtractions for processed sample #19

B. M(T) Measurements

Magnetization vs. temperature measurements were taken for two separate processed samples. In both cases, the zero-field cooled, 10 G measurements showed either no dependence on temperature, or failed to get above the noise level. Several measurements were taken, but all failed to reproduce the curve shown in Fig.4.

C. Scanning Tunneling Microscopy

Another method used to test the sample for superconductivity, and one which had not been done previously, was to examine the I(V) characteristics of the sample using STM. With the STM needle placed over a single spot above the sample surface, the tunneling current is measured as a function of the applied voltage. This is done at a series of temperatures. If I(V) is linear throughout all measurements, then the sample is a normal conductor. However, if below a particular temperature I(V) becomes nonlinear, it is possible that the sample has made a transition into an altered state of conductivity. Studying the curve of dI/dV can then shed more light on the conductive properties of the material.

Preliminary results have shown there to be nonlinear I(V) characteristics at 80K and 140K (Fig.9), however more measurements are needed to verify whether or not the nonlinear I(V) curve is a result of the decreased temperature, and then to determine if the nonlinearity is indicating an altered state of conductivity. Measuring I(V) with the STM has proven difficult, as from the point of view of the STM the sample surface is very dirty and uneven due to the silver deposition and laser ablation.

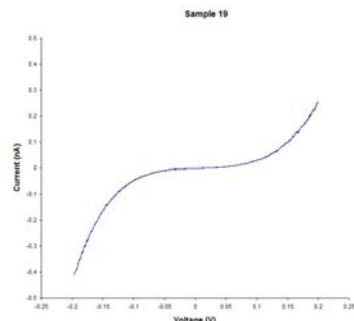


Figure 8: I(V) curve taken at 80K for processed sample #19.

Conclusions

Specially-processed samples of strontium ruthenate were thought to become superconducting at temperatures in the range of 200K to 250 K, based on R(T), M(T), and magneto-optical imaging data. Another signature of superconductivity, the butterfly curve, was also found by subtracting the overlapping ferromagnetism and paramagnetism through a series of M(H) measurements.

In attempting to reproduce and verify the initial data, it was found that the butterfly could not be used as a signature of superconductivity because it persists at temperatures up to 280K using the subtraction techniques. Further measurements also failed to reproduce the z.f.c., 10 G M(T) curve, which was thought to be indicative of the Meissner effect with an onset temperature of 250K.

While preliminary STM data has revealed nonlinear I(V) characteristics at temperatures of 80K and 140K, further measurements are needed to determine whether the nonlinearity indicates a transition in conductivity. It is also unclear what type of transition may be occurring, or if the results are even real, as the sample surface has proven difficult to analyze using STM.

With this new information at hand, the last measurement which must be discussed is the R(T) measurement. While the new magnetization data may be able to argue against superconductivity, the question of how there could be zero resistance in the sample must be answered. One possibility is that the processing of the sample has allowed for large amounts of current to leak off through unexpected regions of the sample or substrate, causing the potential difference across the voltage probes to go to zero without the onset of superconductivity.

The M(T) and M(H)-subtraction data have shown that there are inconsistencies in the arguments made for the case of superconductivity, while further analysis of the I(V) characteristics is needed before conclusions can be drawn. Although it will require further testing to definitively prove or disprove the claim, it would appear as though the chances of the processed samples being a new high-temperature superconductor are slim.

Acknowledgements

I would like to thank my advisor, Dr. Allen Goldman, for providing me with this interesting project. I would also like to thank Masaya Nishioka, Yu Chen, and Yeon Lee for all of their help in the lab. Finally, I would like to thank Serge Rudaz and Wendy Tschaapl for organizing the REU program, made possible through the National Science Foundation grant NSF/PHY-0139099.

References

- A.M. Gulian, K.S. Wood, D. Van Vechten, J. Claassen, R.J. Soulen, Jr., S. Qadri, M. Osofsky, A. Lucarelli, G. Lüpke, G.R. Badalyan, V.S. Kuzanyan, A.S. Kuzanyan, and V.R. Nikoghosyan,
Evidence for High-Temperature Superconductivity in Doped Laser-Processed Sr-Ru-O
<http://www.arxiv.org/abs/cond-mat/0509313>

Measuring Noble Gases in Coma Samples from Comet Wild 2

Undergraduate Student

Jacob Simones

Minnesota State University, Mankato
Mankato MN

Advisors

Dr. Russell Palma

Minnesota State University, Mankato
Mankato MN,
University of Minnesota
Minneapolis MN

Dr. Robert Pepin

University of Minnesota
Minneapolis MN

Measuring Noble Gases in Coma Samples from Comet Wild 2

Jacob Simones

MINNESOTA STATE UNIVERSITY, MANKATO

*Advisors: Dr. Russell Palma & Dr. Robert Pepin
University of Minnesota Physics REU, Summer 2006*

ABSTRACT

Since comets are relics of the early solar system, the formation of the solar system can be better understood through compositional analysis of cometary material. In 2004, NASA's Stardust spacecraft used aerogel (a low density, silicon-based material) to collect coma samples from comet Wild 2 that were then returned to earth for analysis in 2006. Aerogel not from the spacecraft with no embedded cometary material was investigated initially to determine the possibility of measuring noble gases in Stardust samples. Non-flight aerogel samples were heated and the evolved gases measured using a mass spectrometer. The helium and neon levels observed were low enough that measuring helium and neon in Stardust samples using the same method is viable. The first Stardust samples are currently being examined.

1. INTRODUCTION

Material not incorporated into the sun formed a protoplanetary disk from which the planets and other solar system bodies condensed. The compositions of these bodies should be similar to that of the sun under the assumption that solar and disk material came from a common source. However, the compositions of bodies throughout the solar system are known to be wildly different from one another. These differences are attributed to physical and chemical processes, but the exact sequence of events that occurred to form the solar system remains unknown.

Studying the evolution of the solar system requires knowing what the early solar system was like compositionally. Elemental abundances and isotopic compositions from sources such as planets have been well studied, so constraints can be put on current formation theories by comparison with information from early solar system materials. Noble gases are of particular interest because they do not readily react, making them good indicators of elemental and isotopic

mass fractionations caused by chemical and physical processing.[1]

Characterizing noble gases in the protoplanetary disk requires finding a source of material that has remained unchanged since early times. Comets are an important resource in that they are artifacts from the formation of the solar system, and were the focus of NASA's Stardust mission. This mission was designed mainly to collect samples of cometary material from comet Wild 2 and return them to earth for analysis. Far from the sublimating effect of solar radiation, comet Wild 2 has spent most of its life well-preserved in the outer region of the solar system. A recent interaction with Jupiter decreased Wild 2's perihelion distance, conveniently bringing the comet closer to earth for study.

In January 2004, the Stardust spacecraft encountered the nucleus of comet Wild 2 to collect samples of coma gas and dust by impact into aerogel (a very low density, silicon-based material that has been shown to be effective at stopping and preserving high velocity particles). The comet samples were safely returned in January 2006, and are currently

under investigation by science teams worldwide. Due to their relative importance as tracers of fractionation and transportation, our lab is focused on the measurement of noble gas elements and isotopes in Stardust samples using high-sensitivity mass spectrometry.

2. EXPERIMENT

The proposed method for obtaining trapped gases from flight samples was to pyrolyze the aerogel. Volatiles from the flight aerogel may be separated into two populations: coma gas from Wild 2, and gas from any other source. It is thought that coma gas may have been trapped within bubbles formed as the cometary particles melted the aerogel along the entry path. Extrinsic gases may lie on the aerogel surface or may also be trapped within the aerogel. The advantage of heating is that the amount of outgassing in the

compete with the coma gas in the high-sensitivity mass spectrometer. Heating has been effective in measuring gas from interplanetary dust particles, but it was unknown whether or not noble gas concentrations in non-flight, or blank, aerogel would be low enough to permit detection of gases at the levels anticipated in flight samples.

The feasibility of this technique was first investigated by making rough measurements of the volatile composition of aerogel block E226-5B with a residual gas analyzer (RGA). This non-flight aerogel was identical to that flown on the Stardust spacecraft. The first sample cut from block E226-5B had an area of roughly 0.5 cm^2 and was enclosed in a platinum envelope attached to two wire leads on a flange. The flange was attached to a vacuum system and the sample was heated from 50°C to about 1000°C in eleven steps, each step lasting for one hour. Gas measurements were taken periodically throughout each step with the RGA set to scan over a range of 1 to 50u .

The results from each temperature step were superimposed on a plot of partial pressure versus mass, as displayed in Figure 1. The partial pressures of He, Ne, and Ar in the system never exceeded 10^{-8} Torr at any time

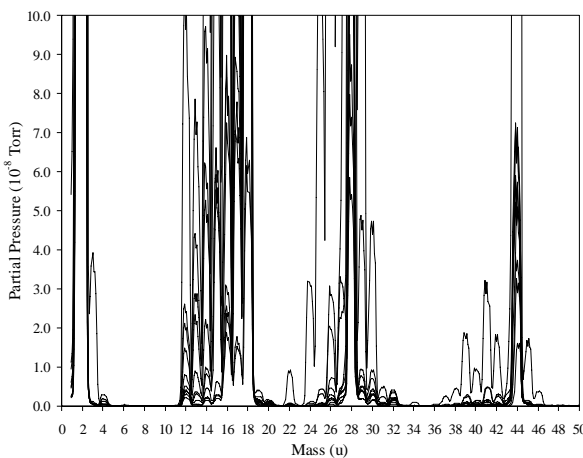


Figure 1: A composite plot of the partial pressures of gas components in blank aerogel within a mass range of 1 to 50 u measured in 10^{-8} Torr for eleven temperature steps from 50 to 1000°C . The He, Ne and Ar peaks (masses 4, 20, and 40) were very small, mainly in comparison to H_2 (2 u), H_2O (18 u), CO (28 u), and CO_2 (44 u). The pressure scale was chosen to demonstrate the relatively small sizes of the He, Ne, and Ar peaks, and caused the dominant peaks to go off scale.

sample is temperature controlled; more tightly held volatiles are released at higher temperatures. This insinuated a two-phase approach for processing the flight samples: an initial, low temperature heating phase (no more than about 200°C) to release surface gases, and a high temperature phase (upwards of 1000°C) for the release of coma gas. The low temperature phase was important as a means of discarding large amounts of contaminating gas that would otherwise

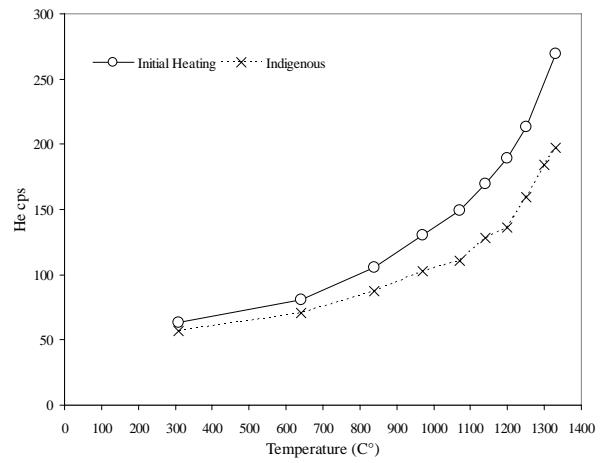


Figure 2: Comparison of the cumulative ${}^4\text{He}$ counts obtained from the initial heating and system background plotted against temperature. Statistically, the amount of ${}^4\text{He}$ from the initial heating was not greater than background for lower temperatures. The difference between the curves at 1330°C gives an upper limit to the ${}^4\text{He}$ contribution from aerogel of roughly 70 counts.

during measurement. This amount is negligible relative to the maximum amounts observed for H_2O and CO_2 , which were above 10^{-7} Torr, and H_2 and CO, which exceeded 10^{-5} Torr. These results showed that as long as the dominant peaks could be reduced,

heating to outgas Stardust samples was worth pursuing on a higher sensitivity system.

A second sample was cut from block E226-5B in order to accurately investigate the release of He and Ne from aerogel during the heating process. The sample had an approximate area of 1.5 mm^2 and was loaded into a platinum envelope and attached to a vacuum system in the same manner as the first sample. To reduce the amounts of H_2 , H_2O , CO , and CO_2 , the system was fitted with cartridges of gas-adsorbing alloys called getters, and liquid nitrogen-cooled charcoal. In addition to the adsorption of heavy components, these materials also adsorb Ar. The possibility of isolating Ar from the charcoal and getters exists, but the task would have been too difficult for the very small chance of detecting Ar from the sample. Therefore, only He and Ne compositions were evaluated for this sample.

The sample was heated to 310°C for 15 seconds, and the evolved gas was purified by the getters and charcoal for 10 minutes. After purification, the gas was analyzed for individual counts of He, Ne, ^{40}Ar , CO_2 and H_2O using a high-sensitivity mass spectrometer. The detection sensitivities of our instrument for ^4He and ^{20}Ne are $4.4 \times 10^{-13} \text{ ccSTP/cps}$ and $1.2 \times 10^{-12} \text{ ccSTP/cps}$ respectively. Eight more steps were performed for temperatures of 640, 840, 970, 1070, 1140, 1200, 1250, and 1330°C . The gas acquired at each step was allowed to accumulate in the system such that every measurement taken was of a

cumulative amount. To determine the amount of indigenous gas in the system that contributed to these measurements, the same piece of aerogel was reheated using the same procedure.

The cumulative amount of He in counts per second (cps) for the heat and reheat runs is plotted as a function of temperature in Figure 2. The amount of He detected during the initial heating was not statistically different from the background (reheat run) for lower temperatures. At 1330°C , approximately 270 and 200 He counts per second were observed from the heat and background runs respectively. By subtracting the indigenous amount from the initial acquisition, the He contribution from the aerogel sample was found to be near 70 counts per second, suggesting aerogel has an intrinsic background concentration of He that must be considered when analyzing Stardust samples.

The amount of ^{20}Ne measured at each step was corrected for contributions from H_2^{18}O and doubly ionized ^{40}Ar using the ratios $\text{H}_2^{18}\text{O}/\text{H}_2^{16}\text{O} = 2.06 \times 10^{-3}$ and $^{40}\text{Ar}^{++}/^{40}\text{Ar}^+ = 8.24 \times 10^{-2}$. The water contribution comes from the atmospheric oxygen isotope ratio $^{18}\text{O}/^{16}\text{O}$. The correction for doubly ionized ^{40}Ar was predetermined experimentally for the instrument. Cumulative Ne counts are plotted against temperature in Figure 3. The amount of Ne from the initial heating was not statistically different from the background suggesting aerogel does not have an intrinsic Ne concentration.

Keystone CO44, our first Stardust sample, was a triangular piece of aerogel with a volume of approximately 1.5 mm^3 . The sample was initially heated to 200°C for 20 seconds with 10 minutes exposure of the gas to the getters and charcoal before measurement of the Ne isotopic composition, followed by the same analysis for He. Again, this initial, low temperature heating

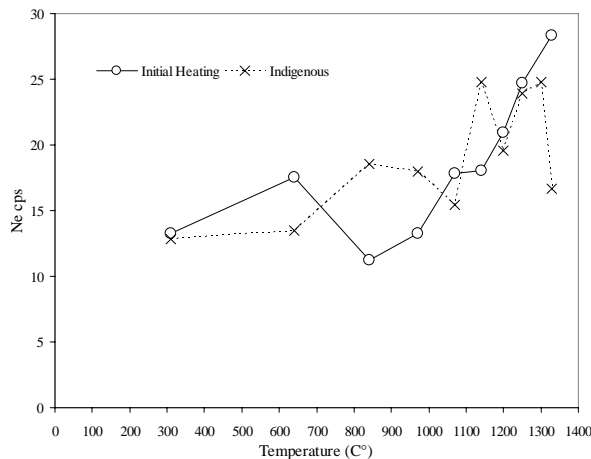


Figure 3: Cumulative ^{20}Ne counts versus temperature for the initial heating and system background. For every temperature step, the amount of ^{20}Ne obtained from the initial heating was not statistically different from the background amount.

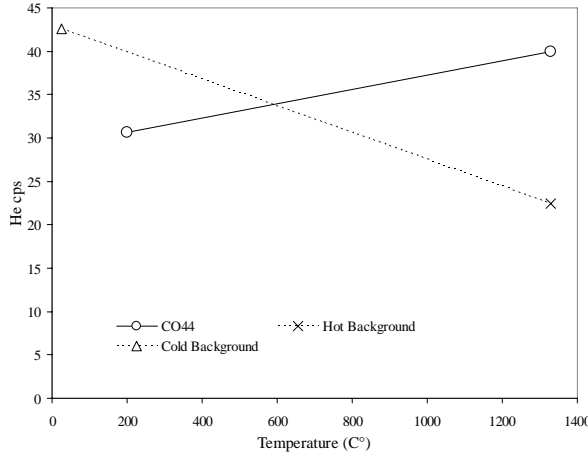


Figure 4: The amounts of ^4He measured from keystone CO44 for the high and low temperature phases, compared with hot and cold background levels. There is no significant difference between ^4He from the keystone and background. The CO44 data was not corrected for ^4He from blank aerogel.

was done to release contamination loosely trapped in the sample or sample holder. The sample gas was liberated in three 15 second heating steps, 1140, 1250, and 1330 °C with a 10 minute purification time after each step. Cumulative gas measurements were taken after the final heating step, in the same order as the low temperature heating. The measurement order is worth noting because of the interplay between H₂ and ^3He . The level of H₂ tends to decrease with getter exposure, which is desirable because H₂ interferes with the measurement of ^3He . By making Ne measurements first, the getters had a longer period of time to reduce H₂ levels, improving the analysis accuracy of ^3He in CO44.

The keystone was reheated using the exact same procedure to obtain a system blank. Before reheating, however, a calibration was run that introduced a large amount of gas into the system. This produced a memory effect that was observed as a He buildup in the mass spectrometer. Test runs of the system were done over the course of several days until the memory effect had decreased to an acceptable level. Keystone CO44 was reheated a second time, but there were no Ne data acquired using the measurement program designed for Ne isotopes. Also, only the high temperature phase was repeated. The low temperature phase was replaced by one of the test runs from after the calibration. There was no heating involved in the test run, so measurements were taken at room temperature, approximately 25 °C.

Figure 4 shows the amount of He measured in keystone CO44 from the 200 °C step and the cumulative amount from the high temperature steps, compared with hot and cold background levels. As the He concentration in aerogel is not yet well known, no corrections were made for He contributions from blank aerogel. Even though the amount of He from keystone CO44 shown in Figure 4 is not

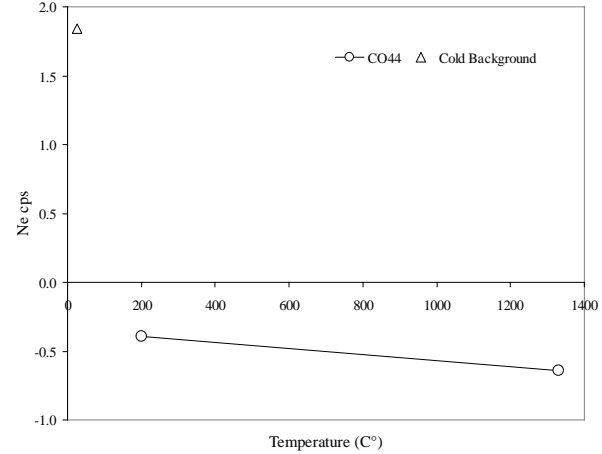


Figure 5: ^{20}Ne released from keystone CO44 during the high and low temperature phases compared to the cold background measurement. After correcting for H₂¹⁸O, the ^{20}Ne from CO44 was found to be negative, consistent with no Ne background. No correction was made for blank aerogel.

statistically different from the background, it is considered an upper limit. The keystone-to-background comparison for Ne is displayed in Figure 5. As before, corrections were made for H₂¹⁸O using the ratio H₂¹⁸O / H₂¹⁶O = 2.06 x 10⁻³. Like with the He data in Figure 4, there was no aerogel correction applied to the Ne data. Even though there is no definitive background value to compare it to, the negative amount of ^{20}Ne observed for CO44 means that any Ne released was well within background. This indicates that if cometary Ne is indeed trapped within the aerogel, it should be possible to detect it.

3. DISCUSSION

It is not yet clear to us what the blank aerogel contribution is to the background based on the results in Figures 2 and 3 alone. Preliminary results by Marty et al. suggest that blank aerogel does not contain He and Ne amounts detectable above their instrument's background.[2] Looking at Figure 2, it seems possible that there is a small amount of He in aerogel. The areas of Marty's aerogel samples were 0.42 and 0.06 mm². Our samples were larger, but Marty et al. have found no correlation between sample size and He and Ne yields from blank aerogel, so we did not necessarily have more gas available for measurement. It is worth considering that the sensitivity of our instrument is greater than the capabilities of the instrument used by Marty by about a factor of 10. As a result, it is possible that we have in fact measured excess He and Ne in aerogel, though only repeated analysis of blank aerogel will resolve this issue.

Marty et al.'s observation of He and Ne above background in samples from Stardust is an exciting result. The sample areas were 0.30 and 0.26 mm². They also report a slightly elevated ²⁰Ne/²²Ne ratio, compared to earth's atmosphere. Given the greater sensitivity of our instrument, if we are able to obtain samples with similar concentrations of He and Ne, it should be possible to more accurately determine the isotopic compositions of those gases in Comet Wild 2. This result may have profound implications for theories of early solar system evolution.

4. ACKNOWLEDGMENTS

Very special thanks goes out to my advisor, Dr. Russell Palma, for his continual support and guidance, academic and otherwise. I would also like to thank Dr. Robert Pepin and Dennis Schlutter for being such great guys every day, and Serge Rudaz and Wendy Tschaapl for organizing a great summer REU program. Thank you to my parents and Annie Cody for putting up with me this summer. I owe this wonderful experience to the National Science Foundation for their funding by grant number NSF/PHY-0139099. To my fellow REU compatriots, I will truly miss you all.

5. REFERENCES

1. Pepin, Robert O., *Atmospheres on the Terrestrial Planets: Clues to Origin and Evolution*. Submitted to Earth and Planetary Science Letters, August 2006, preprint
2. Marty, B., L. Zimmermann, P. Burnard, R. Pik, *Analysis of Bulbous Particle Tracks in Stardust Aerogel : A Search for Cometary Volatiles*. Report from Marty, Zimmermann, Burnard, and Pik of Centre National de la Recherche Scientifique, Centre de Recherches Petrographiques et Geochimiques to the Stardust Science Team, August 2006

Research and Development of Magnetic Tunnel Junctions

Undergraduate Student

Jonathan Sperling
University of Wisconsin-Madison
Madison, WI

Advisor

Professor E. Dan Dahlberg
University of Minnesota
Minneapolis, MN

Research and Development of Magnetic Tunnel Junctions

Jonathan Sperling
University of Wisconsin-Madison

Advisor: E. Dan Dahlberg
Magnetic Microscopy Center (MMC), University of Minnesota-Twin Cities

Magnetic tunnel junctions (MTJs) belong to a class of “spintronics” (spin transport electronics) devices that may soon have important technological applications; for example, as components of nonvolatile magneto-resistive random access memory (MRAM) and magnetic sensors. By taking advantage of spin-dependent tunneling, MTJs exhibit a phenomenon known as tunneling magnetoresistance, in which the probability of tunneling across an insulator between two ferromagnets is dependent on their relative magnetizations. In this article, I will explore the theory behind MTJs, their fabrication, and their application in MRAM.

Spin-Dependent Tunneling (SDT)

SDT is a quantum mechanical phenomenon, in which there exists an imbalance in current carried by up- and down-spin electrons. This property is present in tunneling devices that incorporate ferromagnets, which, due to exchange splitting, possess unequal density of states for up- and down-spin electrons at the Fermi level. Because the density of states at the Fermi level affects tunneling probability, conductances across an insulating barrier are not equivalent for different spins, leading to spin-polarized currents.

Such spin-polarized currents were first studied by Tedrow and Meservey in the early 1970s in ferromagnet-insulator-superconductor junctions, in which sharp peaks in the superconductor density of states allowed for detection of spin-polarization (Tsymbal *et al.*, 2003). It was not until the late 1980s, however, that Slonczewski developed an accurate theoretical model to explain SDT. Slonczewski considered ferromagnet-insulator-ferromagnet junctions, and, after accounting for exchange splitting and electron wavefunction decay into the

insulating barrier, solved the Schrödinger equation to determine how tunneling conductance varied according to the angle between the magnetizations of two insulated ferromagnetic layers:

$$G = G_0 \left(1 + P^2 \cos \theta \right) \quad (1)$$

In the above equation, G is the tunneling conductance and P is the effective spin polarization of the tunneling electrons. The effective spin-polarization is dependent on the constant of decay of the wavefunction, which is, in turn, dependent on the Fermi energy and the potential barrier, according to the following equations:

$$P = \left(\frac{k_\uparrow - k_\downarrow}{k_\uparrow + k_\downarrow} \right) \left(\frac{\kappa^2 - k_\uparrow k_\downarrow}{\kappa^2 + k_\uparrow k_\downarrow} \right) \quad (2)$$

$$\kappa = \sqrt{\frac{2m}{\hbar^2} (U - E_F)} \quad (3)$$

In the above equations, U is the barrier potential energy, E_F is the Fermi energy, κ is the constant of decay, and k is the Fermi wavevector (for the various spins).

A more simplistic, intuitive picture of SDT's dependence on the relative magnetization of the two ferromagnetic layers may be painted in the following way. As electron density increases, partial overlap of occupied orbitals causes the Coulomb repulsion to become more significant; thus, it becomes more energetically favorable for electrons to spread out. Such a distribution allows the electrons in outer orbitals to possess parallel spins, thereby contributing to a net magnetic moment, without violating Pauli's exclusion principle.

In actuality, the spins may be either parallel or antiparallel, depending on the nature of the exchange interaction. For close interactions, such as those between electrons in Fe, the dominant exchange interaction is called direct exchange and is dependent on the radius of the 3d subshell. An exchange integral determines the nature of the exchange interaction: for ferromagnets, the exchange integral is positive, corresponding to parallel spins; whereas, for antiferromagnets, the exchange integral is negative, corresponding to antiparallel spins. Figure 1 is a Bethe-Slater curve that shows the sign and magnitude of the exchange integral for Fe, Co, Ni, and Mn (Dutson, JD).

If we now extend this picture to two ferromagnets separated by an insulating barrier, it becomes apparent why antiparallel magnetizations result in lower tunneling probabilities. In order for tunneling to occur, an electron must possess an energy that is equal to or within $k_B T$ of the energy of the unoccupied quantum state that it hopes to occupy. In an oppositely magnetized ferromagnetic layer, however, the

Coulomb repulsion and the direct exchange interaction discussed earlier

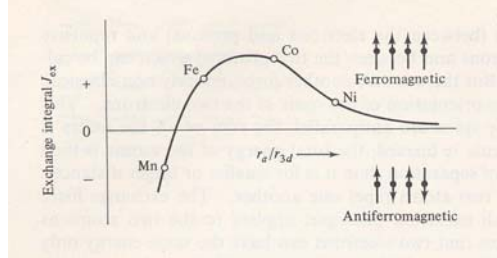


Figure 1. The Bethe-Slater curve showing the variation of the exchange integral with 3d orbital radius. The integral is negative when the 3d orbital radius, r_{3d} , is large relative to the atomic radius, r_a . (This image was taken from Dutson, JD, at <http://www-users.york.ac.uk/~jdd103/>)

make this an energetically unfavorable transition, corresponding to increased tunneling resistance. No such difficulty occurs when the magnetizations are parallel, for then the direct exchange interaction is more favorable.

Magnetic Tunnel Junctions

The phenomenon described above, in which electron tunneling is dependent on the relative magnetization directions in ferromagnet-insulator-ferromagnet structures, is called tunneling magnetic resistance (TMR). In this next section, I will explain how structures called magnetic tunnel junctions (MTJs), which exhibit TMR, are being fabricated in our lab to study the mean free path of electrons in a ferromagnet.

Figure 2 gives a rough a) cross-sectional and b) top-down sketch of a typical MTJ. (In fact, there are two magnetic tunnel junctions in the figure.) The seven layers present are thin films of antiferromagnetic (AFM), ferromagnetic (FM), or insulating materials, ranging from 4 to 500 angstroms in thickness. The entire MTJ is itself only just over 100 nanometers

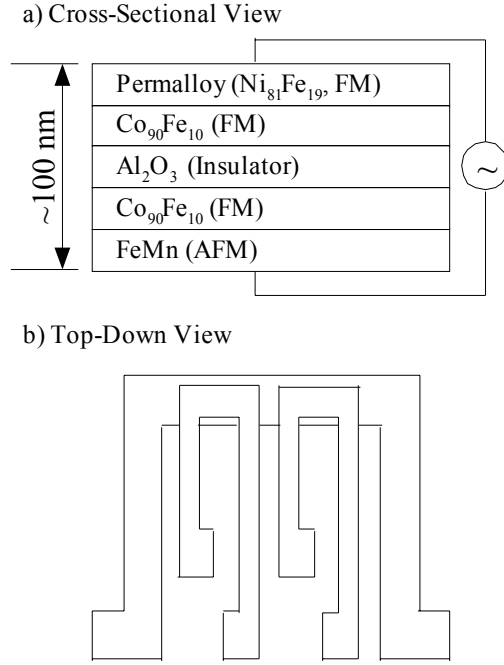


Figure 2. A cross-sectional (a) and top-down (b) sketch of a magnetic tunnel junction. The larger, bottom layers consist of a ferromagnet and antiferromagnet. The top layers, which are simple ferromagnets, are separated from the bottom layers by an insulator.

thick, and rests upon a silicon wafer coated with silicon nitride (Si_3N_4).

Each layer is separately lain down by a process called sputtering, in which atoms are individually propelled from sputtering targets onto the substrate. This is accomplished in a high-vacuum sputtering chamber, which has a base pressure of approximately 5×10^{-8} Torr. Within the chamber, an argon gas is made into a plasma by applying a very high voltage, as well as by confinement in a magnetic field that is perpendicular to a sputtering target. The magnetic confinement decreases the mean free path of the argon atoms, resulting in collisions that further contribute to ionization in the target vicinity. This also increases the likelihood that an argon ion will collide with the sputtering target to eject an atom. The atoms ejected from the sputtering target find

their way to the substrate, which is positioned directly overhead, and become part of the deposited layer.

By covering the substrate with shadow masks, it is possible to precisely control the shape of each deposited layer. The shape of the tunnel junction is very important in determining the axis of spontaneous magnetization in the ferromagnetic layers. It is also crucial that the ferromagnetic layers be properly insulated from one another, for otherwise there is a possibility that the junction will short-circuit. The four masks that we currently use are shown in Figure 3.

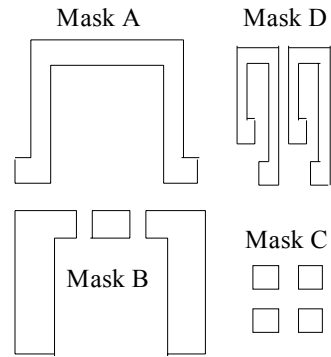


Figure 3. The four shadow masks used to control the shape of the sputtered MTJ layers.

The long, skinny shapes of masks A and D determine the axis of spontaneous magnetization in the ferromagnetic layers. To understand this, assume that the magnetizations are uniform throughout, i.e.,

$$\nabla \cdot \mathbf{M} = 0 \quad (4)$$

Furthermore, assume that there is no free current. Then the differential form of Ampère's Law in matter tells us that

$$\nabla \times \mathbf{H} = 0 \quad , \quad \mathbf{H} = -\nabla \Phi_M \quad (5)$$

From equations (4) and (5), and results

from electrostatics in matter, one can formulate a scalar magnetic potential:

$$\Phi_M = \frac{1}{4\pi} \oint \frac{\mathbf{M} \cdot \hat{n}}{|\mathbf{r} - \mathbf{r}'|} d^3 r' \quad (6)$$

The key feature of equations (5) and (6) is the correspondence between the electrostatic field, $\epsilon_0 \mathbf{E}$, and the magnetic intensity, \mathbf{H} . In particular, one can see by way of analogy that $\mathbf{M} \cdot \hat{n}$ corresponds to an effective surface “magnetic charge.” Now reconsider the long, skinny shape of masks A and D. It is apparent that, were the magnetization vector to point parallel to the long axis, the effective surface magnetic charge would be minimal, and hence the corresponding \mathbf{H} field would also be minimal. By energy considerations, this is the most stable configuration.

Having discussed the mask shapes, I will now briefly outline the seven layers that are sputtered in a typical MTJ. Using mask A, we sputter three layers, the first of which is an FeMn antiferromagnet that is 100 Å thick. The second layer, Co₉₀Fe₁₀, which is ferromagnetic, is sputtered directly on top of the antiferromagnetic layer, with a thickness of approximately 100 Å. The third layer is an oxidized aluminum tunneling barrier, which is approximately 4 to 12 Å thick. Masks B and C are used to sputter thick (~ 100 Å) insulating material, Al₂O₃, in order to prevent unwanted tunneling short-circuits. Finally, mask D is used to sputter the last two layers, consisting of 10 Å Co₉₀Fe₁₀ and approximately 500 Å thick permalloy (Ni₈₁Fe₁₉).

Making MTJ Fabrication More Consistent

There are five different sputtering targets within the sputtering chamber, each composed of different materials. Thus, when growing the different layers that make up the tunnel junction, the substrate must be moved to various targets. This is currently done by manually rotating a long arm, on which the substrate rests, from target to target. While effective, this practice may result in slight variations in the position of the substrate relative to the target.

In order to improve the accuracy of substrate positioning, there is an ongoing project to incorporate a stepper motor into the sputtering system, which will allow the process to be computer-controlled. Currently, the program to control the motor has been written, and we are in the process of obtaining the motor. When the motor is finally installed, it is hoped that MTJ fabrication will be more consistent.

Random Exchange Coupling, Magnetic Exchange Bias, and Crystalline Anisotropy

It is important at this point to discuss the purposes of the various non-insulating layers; especially, the roles of the antiferromagnetic FeMn layer and the ferromagnetic permalloy layer. These materials are used to influence the coercivity, or coercive field, of the Co₉₀Fe₁₀ layers. (Recall that, in ferromagnets, there is a remanent magnetization that persists even after the applied magnetic field has been removed. The coercive field is the diametrically applied magnetic field necessary to

eliminate the remanence magnetization. See Figure 4.)

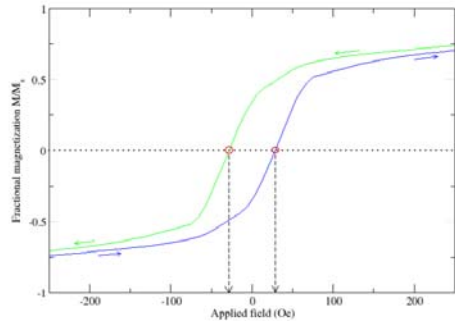


Figure 4. Coercivity is the diametrically opposed applied field necessary to eliminate all residual magnetization. Above is a hysteresis loop, with coercivity marked on the bottom axis at approximately ± 30 Oe. (This image was obtained from <http://en.wikipedia.org/wiki/Coercivity>, and was originally created by Alison Chaiken.

The antiferromagnetic FeMn layer interacts with the adjacent ferromagnetic $\text{Co}_{90}\text{Fe}_{10}$ layer by random exchange coupling, in which antiferromagnetic domains cause an increased coercivity of the interfacial spins (Stöhr). The net effect of these surface interactions is an increase in the coercive field of the entire ferromagnetic layer.

I now digress to discuss a phenomenon called magnetic exchange bias, which, while not necessarily applicable to MTJ fabrication, is nonetheless well worth noting. (In some MRAM applications, MTJs are in fact made to exhibit magnetic exchange bias.) At this point in the production process, the hysteresis loop of the antiferromagnet-ferromagnet is still symmetric; however, there is an interesting effect when one heats the sample beyond the Néel temperature, followed by cooling in a strong magnetic

field. Beyond the Néel temperature, the antiferromagnetic layer transitions to its paramagnetic state, allowing for its magnetic moments to be aligned in a magnetic field. If one then cools the sample, antiferromagnetism is reestablished. Now, however, there exist highly ordered planes of magnetization, due to the previous alignment in the paramagnetic phase. As a result, random exchange coupling has been replaced by a phenomenon called magnetic exchange bias, in which there exists a preferred direction—not just a preferred axis—of magnetization. This process is called “pinning,” because it effectively pins the magnetization in one direction.

Figure 5 presents a cartoon diagram that highlights the difference between random exchange couplings, which simply increase the coercivity of the ferromagnet, and the more ordered phenomenon, exchange bias. Note the difference in the ordering of the antiferromagnetic layer. It must be stated that the reasons presented here are intended only as very rough sketches, being that they are still hotly debated. Actual explanations for these two phenomena are highly active areas of current research in condensed matter physics.

Returning to the MTJs, let's examine the other side of the tunneling barrier, where the ferromagnetic permalloy layer has an opposite effect on its neighboring $\text{Co}_{90}\text{Fe}_{10}$ layer. The relationship between coercivity and crystalline anisotropy is given by

$$H_C = \frac{2K}{M} \quad (7)$$

where, H_C is the coercivity, K is the crystalline anisotropy, and M is the total magnetic moment. Due to its low

crystalline anisotropy, the coercive field of permalloy is very low. To understand this correlation, imagine the opposite case of high crystalline anisotropy, which would correspond to strongly preferred directions of magnetization. Such strong preferences would make intermediate magnetization directions far less favorable, necessitating strong magnetic fields in order for appreciable magnetization reversals to occur. Permalloy, with its low crystalline anisotropy, therefore has a very low coercive field. This effectively lowers the coercive field of the adjacent $\text{Co}_{90}\text{Fe}_{10}$ layer via ferromagnet-ferromagnet surface interactions: when one layer flips, it becomes more energetically favorable for the neighboring layer to flip, for the same reason that one direction is more favorable than the other in the case of magnetic exchange bias.

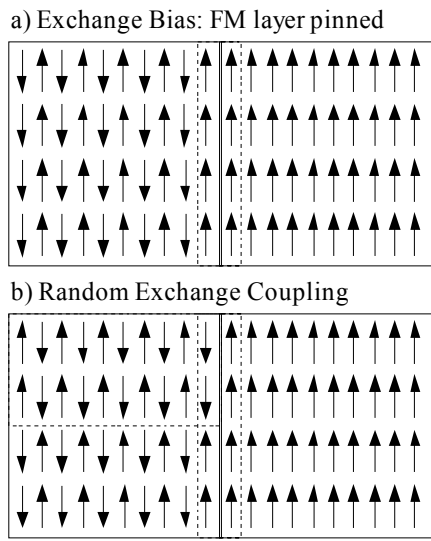


Figure 5. In the case of magnetic exchange bias (a), antiferromagnetic planes are ordered, which makes one direction of magnetization more favorable than the other. In random exchange coupling (b), domains are not so ordered, resulting instead in an increased coercivity.

To sum up the effects of the FeMn and permalloy layers, the magnetic tunnel junction essentially consists of two $\text{Co}_{90}\text{Fe}_{10}$ ferromagnetic layers with different coercive fields, separated by a thin insulating barrier. In a sweeping magnetic field, the permalloy-coupled $\text{Co}_{90}\text{Fe}_{10}$ magnetization would flip before the FeMn-coupled $\text{Co}_{90}\text{Fe}_{10}$ magnetization; so, at any instance, the magnetizations of the two $\text{Co}_{90}\text{Fe}_{10}$ layers may lie either parallel or antiparallel to one another, depending on both the strength and history of the applied external magnetic field. This is exemplified in Figure 6, which shows several hysteresis loops taken at various sweep rates for a related spintronics device called a spin valve. (The hysteresis loops for a magnetic tunnel junction would be very similar.) The ability to switch between parallel (low resistance) and antiparallel (high resistance) magnetizations is particularly important for magnetic tunnel junctions that are to be used as components of MRAM, which is discussed later. Before discussing MRAM, however, I will explain how TMR is actually measured in MTJs.

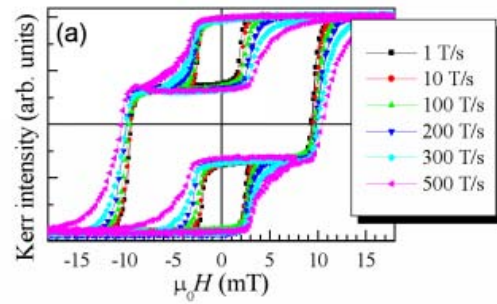


Figure 6. Hysteresis loops for a spin valve. Magnetic tunnel junctions exhibit the same overall pattern due to the difference in ferromagnet coercive fields. (This image was taken from Pennec Y, et al., at <http://lab-neel.grenoble.cnrs.fr/themes/dichro/orangepeel-en.html>.)

Measurement of TMR

To measure magnetoresistance (R_{MTJ}), we use a special circuit consisting of a variable resistor (R_{var}), four large resistors of equal resistance (R), an ammeter, and a voltmeter; the schematic for which is depicted in Figure 7. The advantage of this setup is that, for $R \gg R_{MTJ}$, the correlation between voltage and MTJ resistance is nearly linear, which allows us to use the relationship $\Delta V = I \Delta R_{MTJ}$. Additionally, when R_{MTJ} and R_{var} are identical, the voltmeter reads zero voltage. The MTJ is connected to the circuit with small bits of indium, which are highly malleable and thus convenient for soldering.

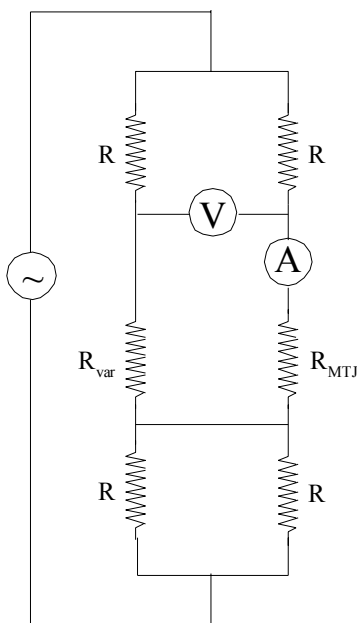


Figure 7. A simplified circuit diagram, depicting the setup for TMR measurement.

To test how TMR varies with applied magnetic field, we use an electromagnet, which sweeps between magnetic fields of roughly -250 to 250 Gauss. Current and voltage measurements are outputted to various

circuitry before finally being read as resistance, V/I , from a lock-in amplifier. This data is then plotted as magnetoresistance versus applied magnetic field.

Sample TMR data from an MTJ is shown in Figure 8, courtesy of Gregory McKusky. Note the two large peaks at -20 and 20 Oersteds, corresponding to a change in magnetoresistance of roughly 11%. In comparison, some labs have reported changes in magnetoresistance that are as high as 100%. Samples with such strong TMR were not prepared by sputtering, but, rather, by growing iron epitaxially on a magnesium oxide insulating barrier.

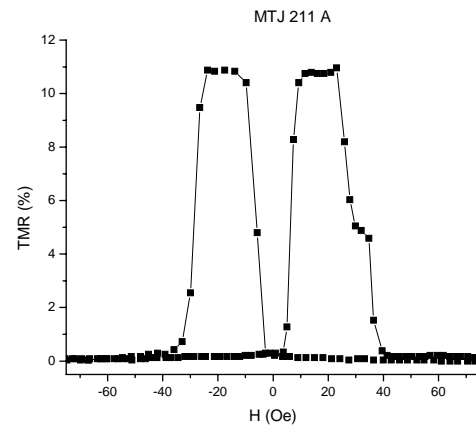


Figure 8. %TMR in one of our lab's MTJs, courtesy of Gregory McKusky. Here, TMR is defined as follows:

$$TMR = (R - R_{\text{baseline}})/R_{\text{baseline}}$$

Improving TMR Measurement

The lock-in amplifier and gaussmeter are connected to a computer via a National Instruments Data Acquisition (NI-DAQ) board. By bypassing the sweep generator with analog output sent from the NI-DAQ board, it was possible to write a program in LabVIEW that simultaneously

averaged the lock-in readings and fully automated the magnetic field sweep cycle. This made the magnetic field-sweep more consistent between measurements and more convenient to execute.

Magneto-Resistive Random Access Memory

At this point, I will consider a particular application of MTJs, namely, their use as components of MRAM. Information storage with MRAM is fundamentally different from storage with other forms of RAM, such as static RAM (SRAM) and dynamic RAM (DRAM). Whereas SRAM and DRAM encode information by current flow and capacitor charge, respectively, MRAM encodes information in the magneto-resistance of the bit, with 0 and 1 represented by the two relative ferromagnet magnetizations, corresponding to states of low and high magnetoresistance.

This form of memory is nonvolatile, whereas SRAM and DRAM respectively require persistent currents and refresher circuits. Moreover, MRAM is high-speed, has nearly limitless read/write endurance, allows for very dense information storage, and—this being of particular importance for defense applications—is radiation hard. MRAM's versatility makes it particularly suited to applications that currently require varied memory types, which are costly to integrate.

Conclusion

A general overview of the theory underlying MTJs has been given, as well as a description of the fabrication process and potential applications in

MRAM. The fabrication process will be further refined until samples exhibit stronger TMR. It is hoped that, in the near future, it will be possible to use these MTJs to study the mean free path of electrons in ferromagnets.

Acknowledgements

I would first like to thank my supervisor, Professor E. Dan Dahlberg, for affording me the opportunity to work in his lab, and for giving me a project that I could call my own. Special thanks go to Gregory McKusky, who patiently answered all my questions, taught me everything I know about magnetic tunnel junctions, and was otherwise a constant help whenever help was needed. I would also like to thank Hyuk-Jae Jang, Tanner Schulz, and the rest of the Dahlberg lab for making my laboratory experience so enjoyable.

For making this program possible, I would like to thank the National Science Foundation, which supported this research experience with grant NSF/PHY-0139099. For their hard work in putting this program together, I would like to thank Professor Serge Rudaz, Wendy Tschaapl, and Jennifer Docktor. I would also like to thank Professor William Zimmerman for his liquid helium demonstration, Jon Kilgore and Roger Olson for their machine shop class, Professor Benjamin Bayman for his GRE preparatory class, Professor Jim Kakalios for his lecture on the physics of superheros, and, for their research seminars, Professor Kenneth Heller, Professor Vincent Noireaux, Professor Allen Goldman, and Professor Paul Crowell.

Last but not least, I would like to thank all of my fellow physics REU participants for making this program such a wonderful experience.

Bibliography

- Tsymbal E, Mryasov O, and LeClair PR. January 2003. Spin-Dependent Tunneling in Magnetic Tunnel Junctions. *J. Phys: Condens. Matter*, 15: R109-R142.
- Dutson, JD. Characterisation of Perpendicular Recording Media. <http://www-users.york.ac.uk/~jdd103/>. Viewed July 26, 2006.
- Joachim Stöhr. Magnetic Exchange Bias. <http://www-ssrl.slac.stanford.edu/stohr/magneticexchange.htm>. Viewed July 26, 2006.
- Pennec Y, et al. Switching-Mode-Dependent Magnetic Interlayer Coupling Strengths in Spin Valves and Magnetic Tunnel Junctions. <http://lab-neel.grenoble.cnrs.fr/themes/dichro/orangepeel-en.html>. Viewed July 27, 2006.

Neutrino Oscillations

Undergraduate Student

Alexander Tenenbaum

Connecticut College
New London, CT

Advisor

Professor Daniel Cronin-Hennessy

University of Minnesota
Minneapolis, MN

NEUTRINO OSCILLATIONS

Alexander Tenenbaum
Connecticut College

Advisor: Prof. Daniel Cronin-Hennessy

Abstract

The NO ν A (Neutrino Oscillation ν_e Appearance Experiment) project is a second generation neutrino oscillation experiment utilizing the NuMI neutrino beam at Fermilab. The detection of neutrino oscillations has necessitated the attainment of certain physical observables and the fulfillment of NOvA is critical to gaining a clearer understanding of these particles. The detector is designed to primarily track ν_e events based on the oscillation of ($\nu_\mu \rightarrow \nu_e$) at peak probability. Fundamental and longterm objectives include but are not limited to the following: the measurement of final mixing angle θ_{13} , Δm^2 , and the CP-violation phase factor. The detector is presently in the design phase and a multitude of projects are currently active, which includes the development and prototype construction of a wavelength shifting fiber spooling machine. The machine will thread thousands of kilometers off fragile wavelength shifting fiber through each of the 32 cells for each of the 23,000 extrusions that make up the bulk of the detector.

1 NOvA

1.1 Overview

NOvA is a second generation neutrino oscillation experiment utilizing the NuMI neutrino beam at Fermilab. The detector is designed primarily to track ν_e events based on the oscillation of $\nu_\mu \rightarrow \nu_e$. The experiment utilizes two detectors: a near detector identical in structure but much smaller than a second, far detector, located approximately 810km from Fermilab and 12km off-axis from the NuMI beam. The far detector will be positioned above ground but but shielded with a 3 meter layer of rock. The objective is to measure the mixing angle of θ_{13} and Δm^2_{12} with a magnitude increase in sensitivity and accuracy compared with previous experiments.

The detector will be a long baseline 30kt liquid scintillator constructed entirely of extrusions using PVC material. The extrusions will be placed in an alternating horizontal-vertical arrangement and each extrusion will be segmented into 32 cells. A looped wavelength shifting fiber will run along the length of each cell which will then be threaded through a manifold and connected to one pixel of an APD (Avalanche Photo Diode). The dimensions are currently 15.6m x 15.6m x 132m, making it significantly larger than the first generation MINOS detector located on-axis at the Soudan Mine. The application of a liquid scintillator has the added benefit of encompassing a totally active design (80%) increasing the number of detectable neutrino events.

1.2 Physics of NOvA

1.2.1 The Standard Model

Presently the Standard Model is the most comprehensive model available describing the most fundamental particles and interactions known; incorporating both fermionic (half-integer spin) particles and their corresponding bosonic (integer spin) force-carrying mediators. Although the Standard Model is the most comprehensive it is in no regards complete. The omission of gravity from the model is one insufficiency observable within its framework. In addition advances in high-energy particle physics, dominated by empirical research, have forced revisions to the Standard Model and provided a firm foundation on which to formulate new physics. Irrespective of these shortcomings the Standard Model still provides a wealth of

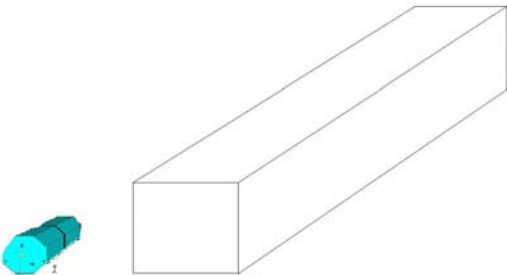


Figure 1: A scale drawing of the NOvA detector as compared to the first generation MINOS detector

scientific information and is the critical baseline for the growing understanding of neutrinos and neutrino oscillations.

The Standard Model partitions fundamental particles into two sectors—the quarks and leptons—each comprising three generations of particles. The leptonic sector contains three integral-charged particles; the electron, the muon, and the tau denoted by e^- , μ , and τ respectively. The τ and μ are generically heavier versions e^- . Each of these charged lepton flavors is coupled with neutral lepton flavors identified generally as neutrinos. The neutrino flavors are designated as ν_e , ν_τ , and ν_μ . The Standard Model limits interactions for neutrinos to the weak force mediators(acting over very small distances); the Z^0 and W^\pm bosons and, if massive, gravity. Consequently neutrinos interact very rarely with matter.

As postulated by Wolfgang Pauli neutrinos were first considered to be mass-less particles however continuing research has provided strong counter-evidence to this initial supposition and has subsequently been supplanted. The new supposition of massive neutrinos was first catalyzed by the “solar neutrino problem,” as neutrino oscillations provided a unique and plausible solution which will be the focus of discussion in the subsequent sections.

Solar theories suggest the fusion reactions of the sun’s core should create a large flux of electron neutrinos. More specifically the theories quantify this flux, predicting an approximate number of observable neutrinos. An experimental-theoretical discrepancy developed, resulting from the first neutrino-detecting experiments¹. The data revealed roughly 1/3 to 1/2 of the expected neutrinos were absent. A discrepancy this large demanded attention motivating, among others, two possible explanations (experimental error was also a serious consideration); either a flawed or inadequate solar theory or the existence of neutrino oscillations. Further empirical data has since, reinforced the latter.

1.2.2 Neutrino Oscillations

As, stated above, there are three generations which can be analyzed by an examination of their weak eigenstates (ν_e , ν_μ , ν_τ) and their mass eigenstates (ν_1 , ν_2 , ν_3). The weak eigenstates are a superposition of all three mass eigenstates which propagate through space and time at dissimilar frequencies and are characterized by a definite mass; more massive particles will propagate slower through space relative to the less massive particles. The transformation from one basis to another is achieved using the unitary “neutrino mixing matrix”. The initial treatment will involve only two flavors, this simplification is primarily motivated to minimize mathematical complexity while preserving the essential concepts that are easily extendable to three flavor neutrino oscillations.

¹The Homestake or Davis Experiment (1960s) provided the first controversial evidence.

The ν_μ and ν_e weak eigenstates are a superposition of the two mass eigenstates ν_1 and ν_2 or equivalently linear combination of the two. The linear combination can be written using a two-neutrino unitary mixing matrix.

$$\begin{pmatrix} \nu_\mu \\ \nu_e \end{pmatrix} = \begin{vmatrix} \cos\theta & \sin\theta \\ -\sin\theta & \cos\theta \end{vmatrix} \begin{pmatrix} \nu_1 \\ \nu_2 \end{pmatrix} \quad (1)$$

This is simply a rotation matrix but in the current context has no spatial meaning. The weak eigenstates can be written as linear combination of the mass eigenstates.

$$\nu_\mu = \nu_1 \cos\theta + \nu_2 \sin\theta \quad (2)$$

$$\nu_e = -\nu_1 \sin\theta + \nu_2 \cos\theta \quad (3)$$

The mass eigenstates propagate through space. Applying Schrödinger's equation to produce the following:

$$\nu_\mu(t) = \nu_\mu(0)e^{-iE_1 t} \quad (4)$$

$$\nu_e(t) = \nu_e(0)e^{-iE_2 t} \quad (5)$$

The corresponding neutrino energy must be treated relativistically $E_i^2 = p^2 + m_i^2$ or $E_i = \sqrt{p^2 + m_i^2}$.

$$E_i = \sqrt{p^2 + m_i^2} \approx p + \frac{m_i^2}{2p} \quad (6)$$

Let's assume at time $t = 0$ all neutrinos are of type μ , hence $\nu_\mu(0) = 1$ and $\nu_e(0) = 0$ ². The application of these constraints in conjunction with algebraic manipulation generates the following:

$$\nu_\mu(0) = \nu_1(0)\cos\theta + \nu_2(0)\sin\theta \quad (7)$$

$$\nu_1(0)\sin\theta = \nu_2(0)\cos\theta \quad (8)$$

Rearranging...

$$\nu_1(0) = \nu_\mu(0)\sin\theta \quad (9)$$

$$\nu_2(0) = \nu_\mu(0)\cos\theta \quad (10)$$

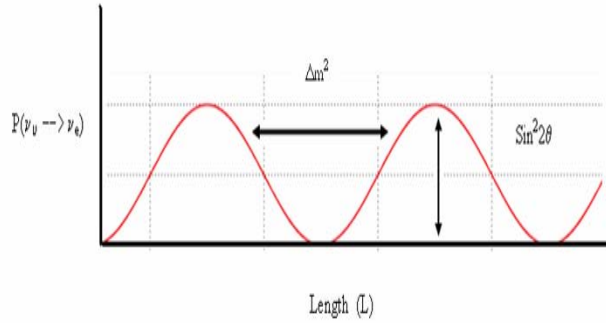
The amplitude of ν_μ is maximized at $t = 0$. The amplitude is normalized (A_μ) to the value of 1 corresponding to this time.

$$A_\mu = \frac{\nu_\mu(t)}{\nu_\mu(0)} = \frac{\cos(\theta)\nu_1(0)e^{-iE_1 t} + \sin(\theta)\nu_2(0)e^{-iE_2 t}}{\cos(\theta)\nu_1(0) + \sin(\theta)\nu_2(0)} \quad (11)$$

Using ?? and ??:

$$A_\mu = \frac{\cos^2(\theta)\nu_\mu(0)e^{-iE_1 t} + \sin^2(\theta)\nu_\mu(0)e^{-iE_2 t}}{\nu_\mu} \quad (12)$$

²for experimental purposes it is important to accurately calculate the number of each flavour neutrino at $t = 0$: this is the purpose of the NO ν A near detector



$$A_\mu = \cos^2(\theta)e^{-iE_1 t} + \sin^2(\theta)e^{-iE_2 t} \quad (13)$$

In accordance with the general quantum mechanical wave functions, the equation is multiplied by its complex conjugate, defining its probability.

$$\begin{aligned} \psi * \bar{\psi} &= [\cos^2(\theta)e^{-iE_1 t} + \sin^2(\theta)e^{-iE_2 t}] \cdot [\cos^2(\theta)e^{-iE_1 t} + \sin^2(\theta)e^{-iE_2 t}] \\ P(\nu_\mu \rightarrow \nu_\mu) &= 1 - \sin^2 2\theta \sin^2 \left(\frac{(E_2 - E_1)t}{2} \right) \end{aligned} \quad (14)$$

Using the standard form \hbar and c are replaced and $(\Delta m^2 = m_2^2 - m_1^2)$. Strategic experimental quantities rely on the baseline length parameter and thus length is used instead of time.

$$P(\nu_\mu \rightarrow \nu_\mu) = 1 - \sin^2 2\theta \sin^2 \left(\frac{1.27 \Delta m^2 L}{E} \right) \quad (15)$$

$$P(\nu_\mu \rightarrow \nu_e) = 1 - P(\nu_\mu \rightarrow \nu_\mu) = \sin^2 2\theta \sin^2 \left(\frac{1.27 \Delta m^2 L}{E} \right) \quad (16)$$

The probability function is dependent upon four quantities; Δm^2 , E (energy of the neutrinos), L (distance traveled by the neutrinos) and θ (the mixing angle). Of these four quantities, two are controllable by the NO ν A experiment (E and L). The ability to control these quantities provides access to specific values for the mixing angle and Δm^2 ; both of which are defined by nature.³ It is conceptually beneficial to graphically analyze the above equation as it applies to NO ν A. NO ν A is searching for $\nu_\mu \rightarrow \nu_e$ which is understood as a subdominant oscillation mode. The dominant oscillation mode is $\nu_\mu \rightarrow \nu_\tau$.

The probability that an oscillation will occur is given by the y-axis and it is dependent on the x-axis defined as the base length L . The oscillation probabilities are plotted for a given energy level (GeV). The amplitude of the sinusoidal function is dependent on the mixing angle θ . While the period of oscillation is easily seen to be controlled by the Δm^2 . The ratio of $\frac{L}{E}$ is usually defined as $\frac{500 \text{ km}}{\text{GeV}}$.⁴ At a maximal mixing angle $((n + \frac{1}{2})\pi)$ there is a peak (given L and E where pure ν_j neutrinos will transition to purely ν_i neutrinos). Conversely non-maximal mixing angles will have lower corresponding transition probabilities. It is also worth noting that for small values for Δm^2 the probabilities will oscillate slower. This relationship also provides the mathematical description for the characterization of neutrino mass due to oscillatory behavior.

³Presently there are no verified theoretical predictions defining these values. The unavailability of such predictions is one of the major motivations for observing and setting limits on these quantities experimentally.

⁴The NuMI beam utilized by NO ν A will be approximately 1 GeV.

If Δm^2 were zero neutrino transitions would not exist, thus a small non-zero Δm^2 value demands a non-zero mass for at least one neutrino.

As discussed earlier the three neutrino mixing analysis is an extension of the two-neutrino case, however the three-by-three unitary matrix is prohibitively complex and will not be discussed in detail in this paper. There are a few characteristics that should be noted. First as would be expected there are three mixing angles (θ_{12} , θ_{23} and θ_{13} ⁵) However an unexpected phase factor, CP-violation phase factor, is also included and thus the three flavor case involves four parameters. The CP-violation phase factor is result of neutrino/anti-neutrino asymmetry to be discussed in the following section.

1.3 CP-violation in the Lepton Sector

1.3.1 CP-violation

One significant question is the origin of the excess matter observed in the universe. To probe this question physicists search for CP-violation processes. The operation C, represents charge conjugation (replacing a particle with its antiparticle) and P represent parity ($\vec{r} \rightarrow -\vec{r}$) A neutral kaon (K_L^0) participates primarily in two decay modes: $K_L^0 \rightarrow \pi^+ e^- \bar{\nu}_e$ or $K_L^0 \rightarrow \pi^- e^+ \nu_e$. Applying charge and parity conjugation to either of the decay modes will result in the other. If CP was conserved there should be an equal probability for either decay mode to occur. However experimental results present evidence that one decay mode occurs with a significantly greater probability than the other, hence an observable CP-violation

While a rarity in nature CP-violations have been confirmed in the quark sector, although it is not of sufficient size to explain the matter anti-matter asymmetry in its entirety. Consequently other occurrences of this violation are needed and the lack of any thus far has posed a serious problem to physicists. Although no CP-violation has been discovered in the Lepton sector, it may exist within the neutrino generations and the potentiality for its existence could significantly increase the collective understanding of nature at its most fundamental level. NO ν A will search for CP-violations utilizing transition probabilities for neutrinos and anti-neutrinos.

Similarly, the neutrino probabilities apply to both neutrino and anti-neutrino oscillations. If CP was conserved the probabilities would be the equal $P(\nu_\mu \rightarrow \nu_e) = P(\bar{\nu}_\mu \rightarrow \bar{\nu}_e)$ and the CP-violation phase factor would be 0. However the rise of an inequality in the above expression would dictate a CP violation. Since NO ν A can detect both transitions it will be able to measure the phase value⁶. Again this may provide solutions to the matter asymmetry.

The oscillation probability $P(\nu_\mu \rightarrow \nu_e)$ formulation varies slightly from the two-flavor example above and is given by $P_{vac}(\nu_\mu \rightarrow \nu_e) = \sin^2 \theta_{23} \sin^2 2\theta_{12} \sin^2 \left(\frac{1.27 \Delta m_{32}^2 L}{E} \right)$. The detector location is critical to maximizing the effectiveness of the NO ν A project and the preceding equation is applied for the determination baseline length (i.e. the distance from the initial neutrino flux) where the probability of ν_e transitions is maximal⁷.

1.3.2 Matter Effects

The N μ MI beam travels through the earth's crust, exposing the propagating neutrinos to dense matter. The baseline length, the mass and electron densities along the beamline do have appreciable effects on the transition probabilities and must be corrected for in the idealized vacuum equation giving:

$$P_{mat}(\nu_\mu \rightarrow \nu_e) = \left(1 \pm 2 \frac{E}{E_R} \right) P_{vac}(\nu_\mu \rightarrow \nu_e) \quad (17)$$

where E_R is the matter resonanc energy dependent on the electron number density , Δm^2 , and earth matter density.

⁵primary parameter to be measured by NO ν A

⁶While it would be advantageous to perform this experiment in vacuum, NO ν A will operate in the presence of matter affecting the measurement of anti-neutrino events. This fact necessitates certain adjustments to accurately measure the phase factor.

⁷NO ν A will be located at the first peak of the probability function.

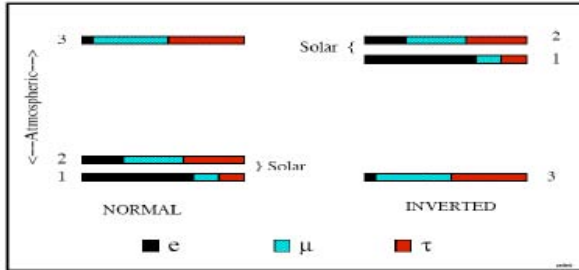


Fig. 3.1: The two allowed three-neutrino mass squared spectra that account for the oscillations of solar and atmospheric neutrinos. The normal spectrum has $\Delta m_{32}^2 > 0$ and the inverted has $\Delta m_{32}^2 < 0$. The ν_e fraction of each mass eigenstate is indicated by the black solid region, whereas the ν_μ (ν_τ) fraction is indicated by the blue-green right-leaning (red left-leaning) hatching.

These mass effects are significant to correctly analyze the CP-Violation and to distinguish the two possible mass hierarchy states of the three neutrino masses, defined arbitrarily as the normal and inverted hierarchies. The exact proportion of each flavor is not precisely defined in the figure, but are approximations and projections given the available data.

Matter effects inversely affect the neutrino and anti-neutrino transition probabilities; enhancing neutrino transitions and suppressing anti-neutrino transitions and thus experimental results may be able to distinguish the sign of Δm^2 establishing the correct mass hierarchy. NO ν A will be the only future generation neutrino experiment capable of resolving these matter effects with any degree of certainty. The two competing projects will have insufficient baselines, approximately 1/4 NO ν A's baseline, to measure this parameter.

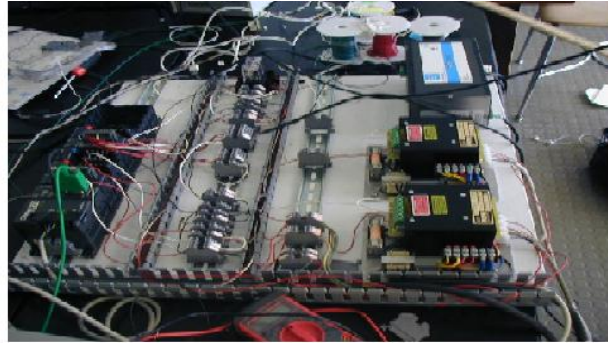
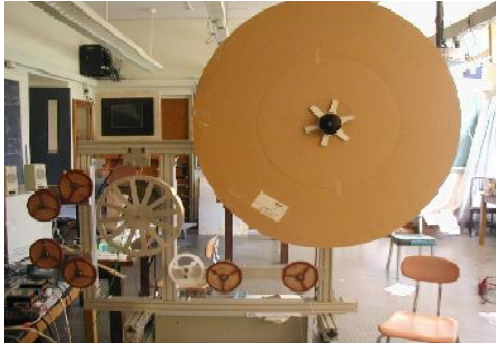
2 Wavelength Shifting Fiber Spooling Machine

The detector is presently in the design and testing phase and a multitude of projects are currently active. One project, the focus of this section, is the development and prototype construction of a wavelength shifting fiber spooling machine. The machine will thread thousands of kilometers of fragile wavelength shifting fiber through each of the 32 cells for each of the 23,000 extrusions that make up the bulk of the detector.

The WLS is a fiber capable of shifting incident electromagnetic radiation into longer wavelengths (green light). In the NO ν A detector the photons produced will be converted into an electronic signal using the Avalanche Photo diodes or APDs. The fiber has been tested resulting in defined constraints on the fiber's maximum tension and bend radius. Both were considerable factors accounted for in the development of this device.

Most neutrinos incident on the detector will simply pass right through it without interaction. Neutrinos participate in two types of weak interactions, neutral current (NC) and charged current (CC) interactions. The neutral current interactions are mediated by neutral the Z^0 boson prohibiting any charge exchange. The neutrinos will simple transfer momentum to some other particle. The CC event will transfer charge from one particle to another producing a charged lepton that deposits energy in the detector and is detected through scintillation light collected by WLS fiber. The production of a charged lepton (μ or e) provides a distinctive feature for CC selection.

The primary machine operation involves the automated controlled spooling of the fiber to a number of predefined lengths (according to the position of the cell in the extrusion) and unwinding as the fiber is vacuum-pulled down the length of the approximately 15.6 m long cells. Specific tension needs to be maintained during all phases of operation including phases of sharp acceleration and deceleration of the fiber



spools.

Motion control is implemented using high resistance reversible AC inductor torque motors specifically designed to provide constant torque while operating in stall. These motors along with torsion and linear potentiometer tension sensors and quadrature encoders regulate the spooling motion and control tension within a specified range. A touch-screen operator screen interfaces the automated processes and the operator allowing a limited input selection for various tasks.

The automated operations are processed by a programmable logic controller (PLC), which is an isolated microprocessor, typical in automated tasks, designed to input and output various AC and DC digital and analog signals as well as execute internal mathematical operations executing Relay Ladder Logic (or RLL). The PLC is advantageous due to its reliability, stability, and stand-alone capabilities. Once programmed the PLC will run independently and indefinitely.

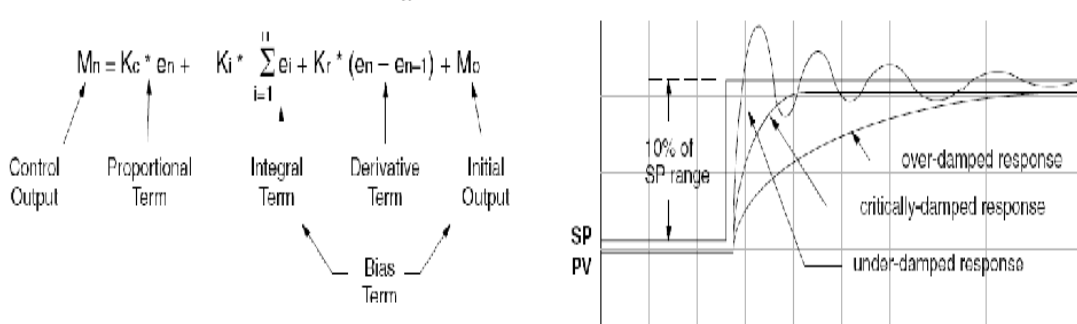
The machine is designed to thread thousands of kilometers of expensive fiber. The inevitability of time budgets as well as the fiber constraints already discussed create dynamic obstacles to the machine design. The calculated acceleration and deceleration times due to these constraints require operating linear spooling spooling speeds of 3 m/s and accelerations/decelerations between $1 \frac{m}{s^2}$ and $2 \frac{m}{s^2}$. Control algorithms, specifically PID loops (Proportional-Integral-Derivative) provide the necessary logic to stay within the boundaries of these constraints.

The particular loop employed is based on the position form of the PID algorithm. PID loops are often used to correct for system instabilities that result in uncontrolled oscillations. The current position defined as the present value or PV may deviate from its set point (or SP) value. The size of this difference is the error term. The proportionality constant is thus proportional to the size of the error. The algorithm will use the information from the PV and SP values to generate an output that will hopefully decrease the system error. In most control processes there is a time lag and the integral term evaluates the timespan or lag of the error and sets to correct (decrease) the error, integration over some length of time. The derivative control attempts to “predict” future error terms by taking the time derivative of the error term, the rate of change of the error, and is controlled by a derivative constant. While there are various position PID forms for a myriad of applications the follow form was used.

This incremental method for process control does not guarantee a system’s stability; choosing “incorrect” PID constants may result in instability beyond that of the uncontrolled system. The bias term in the above figure represents the sum of the initial output and the integral term and is essential to the constant portion of the output. The oscillation of the output around its bias value is similar to the PV oscillation around its SP value.

Depending on the application an overdamped or underdamped system may be acceptable. However the required precision and speed of the spooling machine puts very strict limits on the level of over/under damped behavior and for the majority of stages requires critically damped behavior over an extremely short time interval typically requiring accelerations to speeds of 3 m/s in less than a second and a deceleration from the same speed to full stop within a fifth of a centimeter.

The exact specifications of the the design have not been finalized nor have the exact requirements for



its operation time scale but significant progress has been made to meet the anticipated constraints. Currently the machine is in operation, able to perform the key automated events of the final production (at a level of performance below optimal levels), In its current state it serves as a testing bed for future design considerations as defining possible limitations on final production-ready machine performance.

Acknowledgements

Thank you to Professor Daniel Cronin-Hennessy, Jim Grudzinski, Serge Rudaz, Ken Heller and the University of Minnesota Physics Department.

Magnetic Reconnection and Its Effect On Earth's Aurora

Undergraduate Student

Pamela Vo
Baylor University
Waco TX

Advisor

Professor Cynthia Cattell
University of Minnesota
Minneapolis MN

Magnetic Reconnection and Its Effect on Earth's Aurora

Pamela Vo
Baylor University, Waco TX

Advisor: Cynthia Cattell
University of Minnesota, Minneapolis MN

Abstract:

When reconnection occurs in Earth's magnetotail, an explosive substorm can result. Substorms are associated with dynamic changes in the aurora, and magnetic field data and ion flow data from Cluster were used in correlation with IMAGE picture data to compare the timing of the reconnection process and the changes in the aurora. During reconnection, energy in the form of Poynting flux and particle energy flux flows toward the earth. Data from Cluster (in the reconnection region) and Polar (on magnetic field lines closer to the earth but well above the auroral acceleration region) were analyzed to see if the energy source could be determined and to look for evidence of energy conversion.

I. Introduction

Magnetotail reconnection can lead to magnetospheric substorms, which are associated with dynamic changes in the aurora. The relative timing of the reconnection process and the changes in the aurora are important to understand.

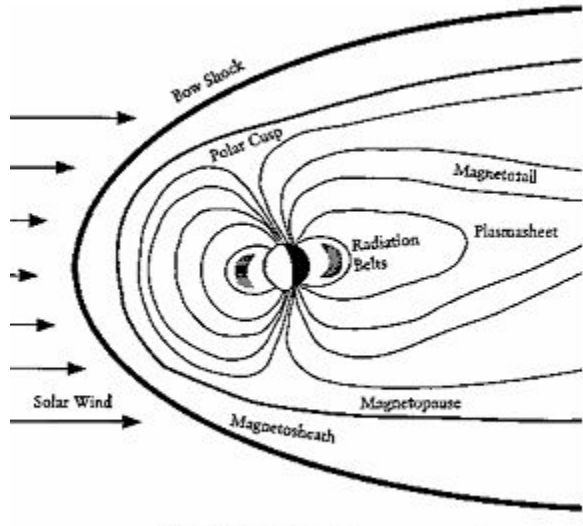
The process of reconnection also converts energy that is stored in the magnetic field into kinetic energy (particle acceleration) and wave energy (Poynting flux). This energy flows toward the earth and can ultimately result in the acceleration of electrons that excite oxygen and nitrogen in the atmosphere, creating the aurora. By looking at satellite data at the reconnection event, at intermediate distances, and at the site of aurora on Earth, the questions of timing and energy flow can be examined.

II. Background

The entire solar system is permeated by the solar wind, which originates from the Sun's expanding corona. The solar wind has a speed of about 400 km/s and is of low density, about seven ions per cubic centimeter at 1 AU from the Sun in the ecliptic plane [Paschmann *et al.*, 2003]. It is mainly composed of H⁺, with a small component of helium nuclei and traces of heavier ions [Paschmann *et al.*, 2003].

Strong magnetic fields in the solar corona, coupled with the high conductivity of the solar wind, result in an interplanetary magnetic field (IMF) carried by the solar wind; the IMF has a field strength of a few to several tens of nanoteslas at 1 AU [Paschmann *et al.*, 2003]. The earth's dipole magnetic field and the solar wind interact to form Earth's magnetosphere (Figure 1), the region of space to which the earth's

magnetic field is confined by the solar wind. The nightward side of the magnetosphere is stretched out into a long magnetotail, and the natural boundary between the earth's magnetic field and the solar wind is called the magnetopause (located at a distance of $\sim 10 R_E$ on the dayside [Cowley, 1996]).



THE MAGNETOSPHERE

Figure 1. Diagram of the magnetosphere from the University of Minnesota.

The magnetotail has both “open” field lines, which have one part closing through Earth’s core and the other part closing through the Sun, and “closed” field lines, which close only through the Earth. Open field lines are found in the tail lobes while closed field lines are found in the plasma sheet.

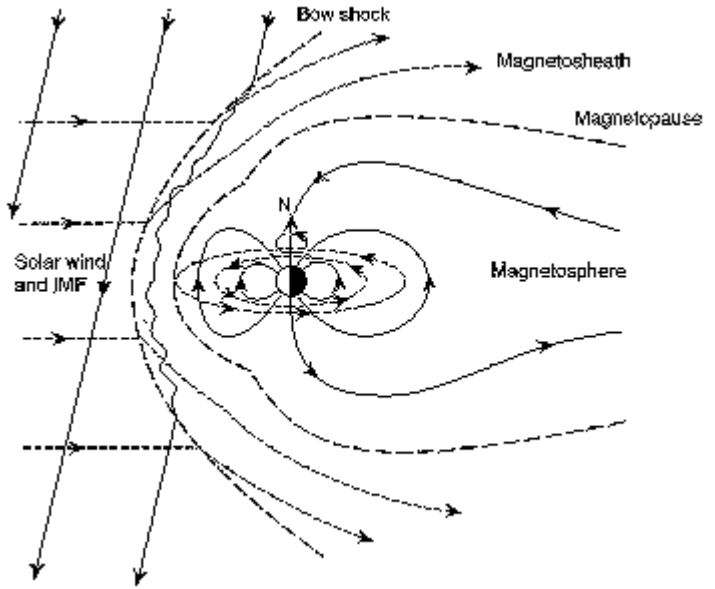


Figure 2. Interaction of the solar wind with the earth's magnetic field. Diagram from Cowley, 1996.

During periods when the IMF points south, opposite of the earth's magnetic field (Figure 2), reconnection occurs between the IMF and Earth's magnetic field, leading to open field lines. This allows solar wind plasma to enter the magnetosphere and sets up a magnetohydrodynamic (MHD) generator, which uses the motion of the plasma to generate currents that generate electrical energy.

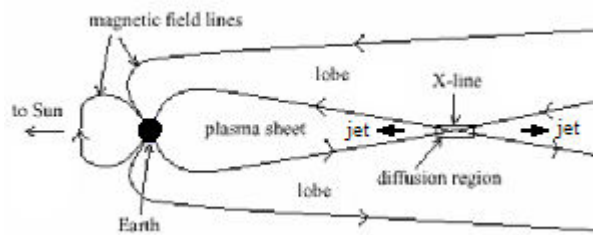


Figure 3. A diagram of closed and open field lines, also showing the reconnection x-line. Oeierset *et al.*, 2001

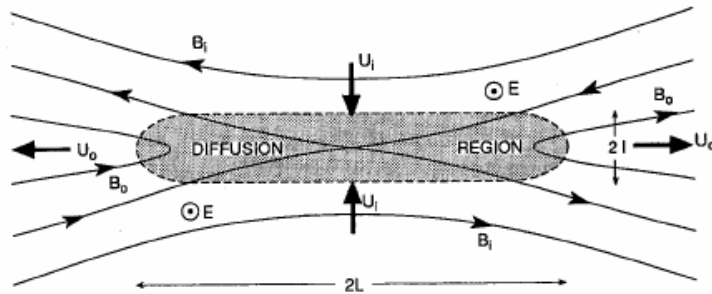


Figure 4. After reconnection, plasma jets away from the reconnection line, toward Earth and the magnetotail. Kivelson and Russell, 1995.

The plasma flow in the magnetosheath carries the open field lines to the tail, where reconnection occurs once again. If reconnection occurs more quickly at the magnetopause than in the magnetotail, magnetic fields build up in the tail lobes, precipitating a magnetic substorm. Reconnection in the magnetotail then occurs close to the earth ($\sim 20 R_E$).

Upon magnetotail reconnection, earthward-bound closed field lines accelerate the solar wind plasma toward the earth. These electrons and ions attain speeds of ~ 1000 km/s. At lower altitudes, the energy flow associated with reconnection can generate electric fields that accelerate the electrons to energies of tens of keV. These electrons are guided to the polar regions by Earth's magnetic field, where they excite oxygen and nitrogen in the atmosphere, producing the aurora. The dominant green color in the aurora is from the excitation of atomic oxygen, while the red lower borders of active arcs comes from molecular nitrogen [Stenbaek-Nielsen *et al.*, 1999].

III. Spacecraft Overview

Cluster was launched by the European Space Agency in 2000. It consists of four spacecraft arranged in a tetrahedral formation, which allows for both the

differentiation of spatial and temporal variations and the determination of the velocity of structures. Cluster follows an elliptical orbit of $4 R_E \times 19 R_E$.

The Imager for Magnetopause-to-Aurora Global Exploration, or IMAGE, satellite was the first spacecraft dedicated to imaging the earth's magnetosphere. Its Wideband Imaging Camera provided images of Earth's aurora in ultraviolet wavelengths.

NASA launched the Polar satellite in a highly elliptical orbit in 1996. Polar measures particle, electric field, and magnetic field data below $9 R_E$. It also images the aurora.

IV. Method of Data Analysis

The primary data set was a list of events where Cluster had observed the signatures of reconnection occurring in the earth's magnetotail. The times of these events were used to examine IMAGE data to see if "good" IMAGE picture data (i.e., that with most of the auroral zone covered for the complete event time) was also available during the same time intervals. Only one event had images of the entire auroral zone throughout the period of reconnection (before and after the ion flows), so that event was concentrated upon for the analysis of

the relative timing of the reconnection process and the dynamic changes in the aurora.

Polar was used to look at intermediate distances (between the x-line and Earth) so that the question of energy flow from the reconnection region could be investigated. The Poynting flux from both Cluster and Polar were inspected.

To do this, magnetic and electric field data from SDT, a data decommutator software package for these satellites, were exported and read into IDL, which was then used to de-trend the data. This removed the underlying lower frequencies so that variations in the higher frequencies could be seen.

Because the electric and magnetic fields were sampled at different data rates, both sets were first resampled to the same data rate. The data rate of the magnetic field values was used because the magnetic field had the slower rate, and by resampling both sets of data to the slower data rate, no new data points would need to be extrapolated

from the existing ones (though the excess ones would have to be dropped). After both sets of data were at the same sample rate, the data was de-trended using an IDL module written by John Dombeck. The de-trended data was then fed into another IDL module (also by John Dombeck) for the calculation of the Poynting flux.

The Cluster electric and magnetic field data were in the GSM (Geocentric Solar Magnetospheric) coordinate system, with the x-axis along the line between the earth and the Sun, the y-axis perpendicular to the earth's magnetic dipole, and the positive z-axis in the direction of the northern magnetic pole. The Poynting flux was calculated in the x-direction to show the flux toward or away from the earth.

Polar data was in field-aligned coordinates (FAC), where Z is along the local model magnetic field, Y is perpendicular to the model field and eastward, and X is perpendicular to the model field and completes the right-handed system.

V. Timing of Reconnection and Auroral Features: 2001/08/17 Event

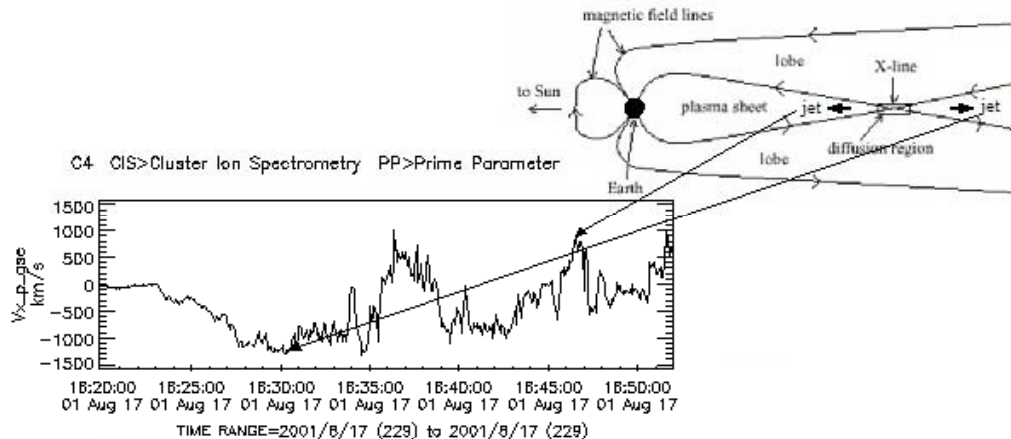


Figure 5. Illustration of the plasma jets moving away from the x-line. Diagram from Oeierset *et al.*, 2001. Ion data from CDAWeb and H. Reme.

The signature of reconnection in the Cluster data is tailward and then earthward flow of plasma, with a coordinated switch from southward to northward B_z . While reconnection occurs, B_z and V_x are negative tailward of the x-line and positive earthward of the x-line. The ion flow data (Figure 6a)

shows that there is tailward flow initially, so Cluster is tailward of the x-line when reconnection begins. The flow changes to earthward flow when the x-line crosses the satellite (so that the satellite is earthward of the x-line).

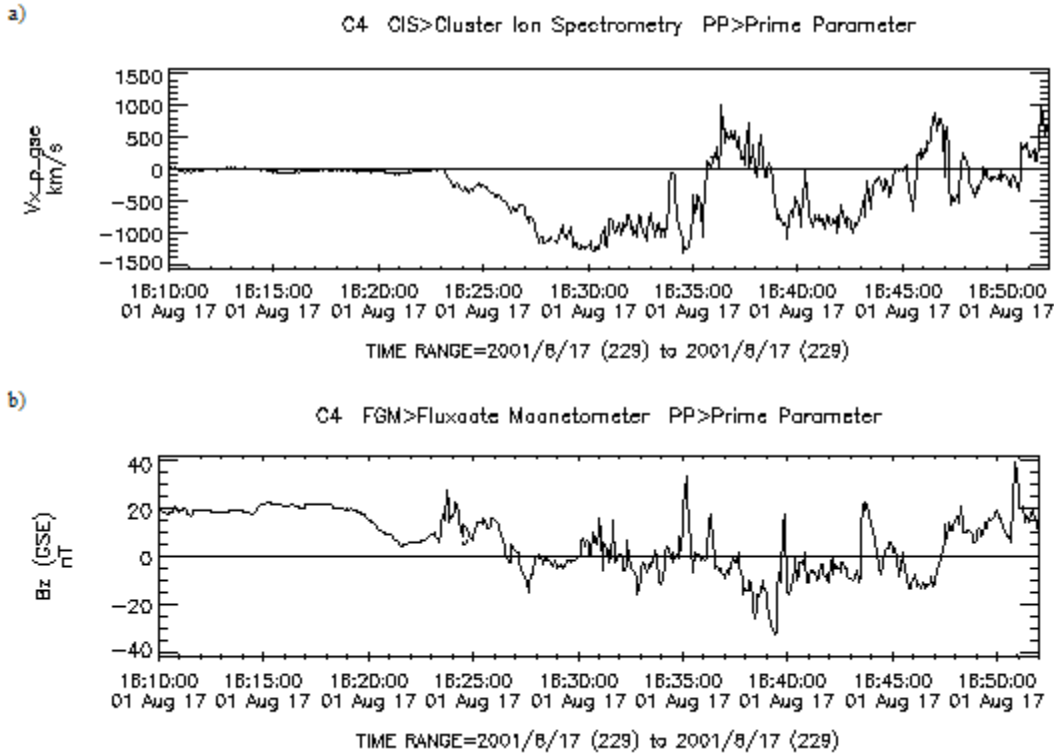


Figure 6. Cluster Spacecraft 4 data from CDAWeb. (a) Proton bulk velocity. Data provided by H. Reme. (b) DC magnetic field. Data provided by A. Balogh.

The Cluster data was compared with the available IMAGE data to examine the dynamic changes in the aurora (Figure 7). When the ion flow detected at Cluster is around zero, before reconnection happens, the aurora is relatively quiet. At 16:23, tailward flow begins (in the negative x-direction), and brightening starts to occur in

the auroral oval. The ion flow away from Earth has just peaked before 16:31, and the most equatorward arc brightens and expands toward the pole. The oval continues to expand as ion flow continues, and as the ion flow slowly returns to zero and reconnection ceases, the aurora becomes less intense again.

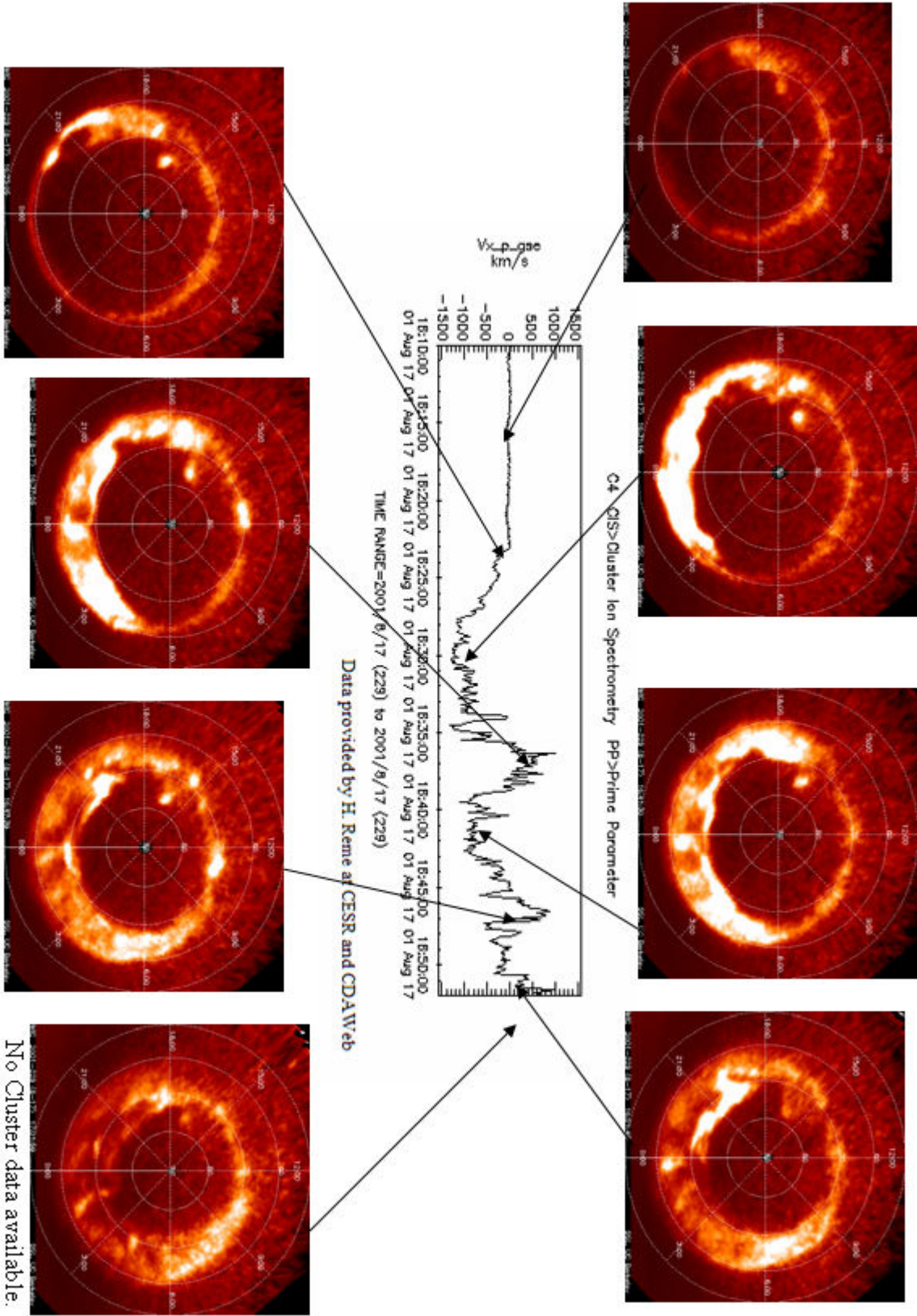


Figure 7. Cluster and IMAGE data during reconnection.

VII. Energy Flow: 2002/08/21 Event

Once again, the sign of reconnection is tailward and then earthward flow of plasma,

along with a switch from southward to northward B_z .

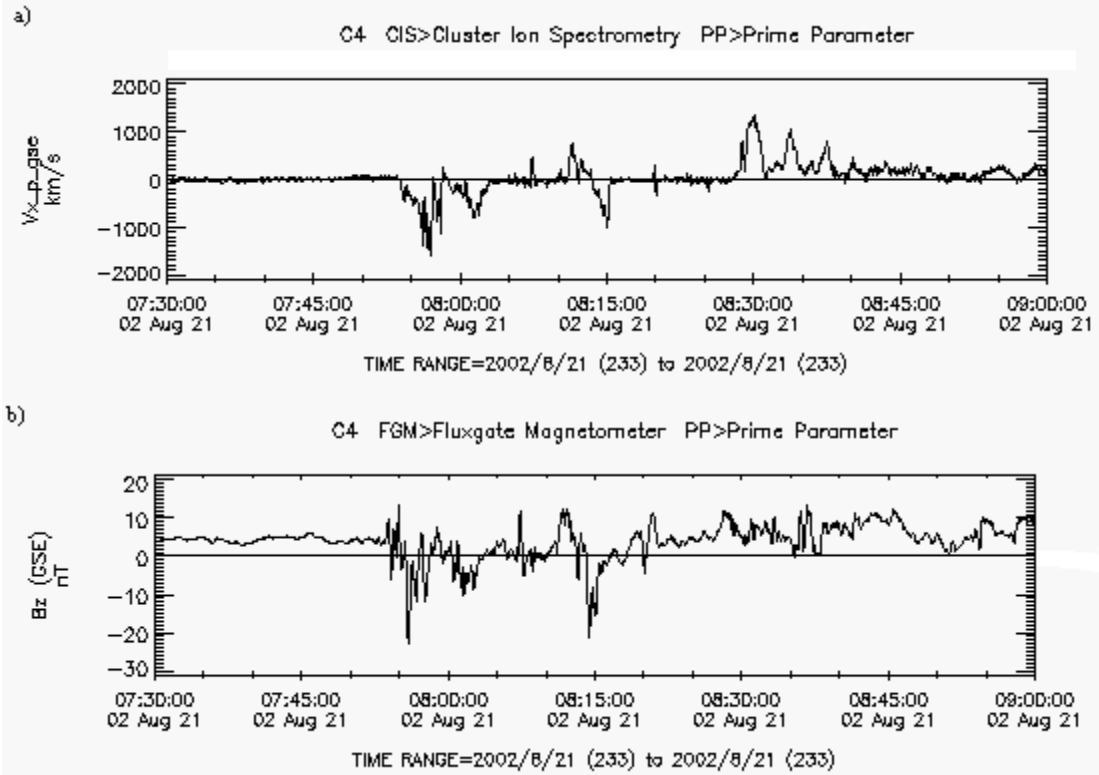


Figure 8. Cluster Spacecraft 4 data from CDAWeb. (a) Proton bulk velocity. Data provided by H. Reme. (b) DC magnetic field. Data provided by A. Balogh.

To look at the Poynting flux in the waves, the electric and magnetic field data was de-trended and then the flux was calculated (Figure 9). Waves are seen in the de-trended electric and magnetic fields at the time that reconnection occurs at Cluster. The E/B

ratios are ~ 1200 km/s, less than but comparable to the Alfvén speed of ~ 2700 km/s, suggesting that the waves may be Alfvén waves. These waves carry the Poynting flux primarily tailward when Cluster is tailward of the x-line.

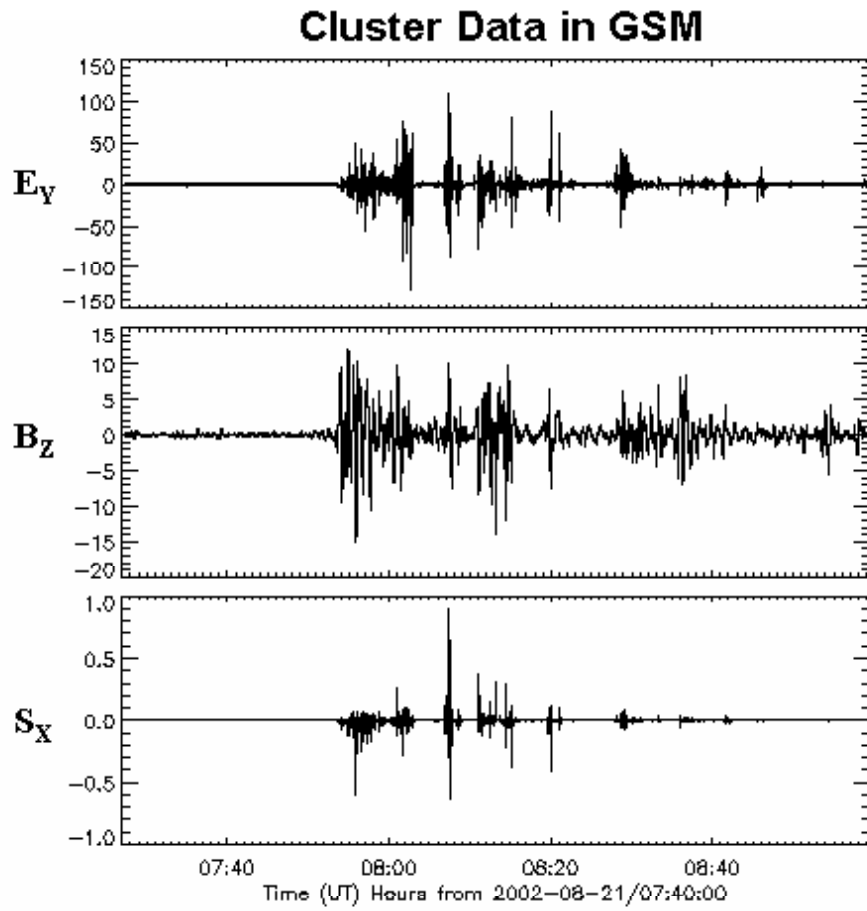
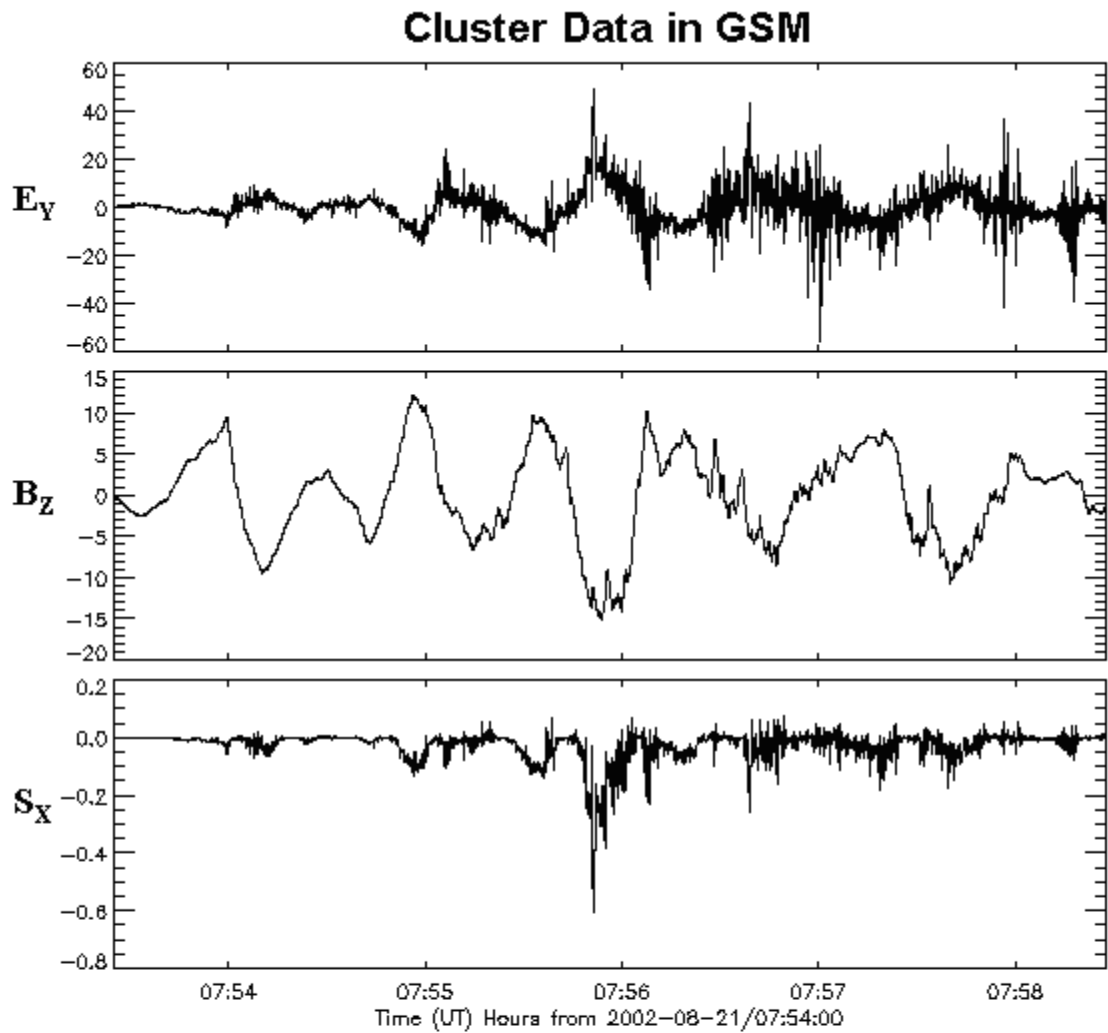


Figure 9. Graph of Poynting flux in the x-direction from Cluster data in GSM coordinates.

Looking at a close-up of the Cluster data used to calculate S_x (Figure 10), the coordinated waves in the electric and

magnetic fields can be seen, though they are out of phase with each other.

a)



b)

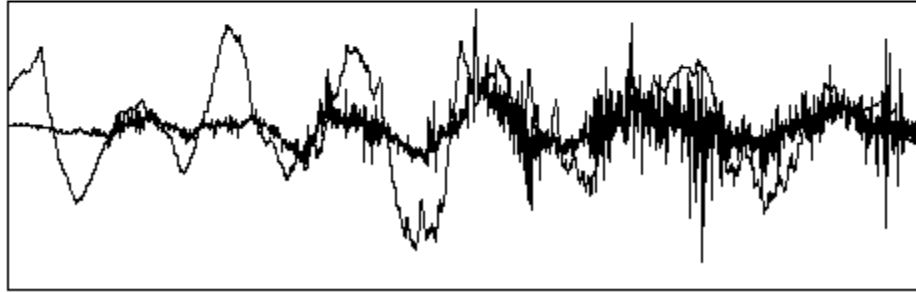


Figure 10. (a) Close-up of Cluster data, showing the waves found in the electric and magnetic fields. (b) Superimposed electric and magnetic field data, illustrating the correlated E and B.

When reconnection begins at Cluster, Polar encounters the plasma sheet boundary ($\sim 8 R_E$) due to the reconnection-related large-

scale reconfiguration. Large amplitude waves are visible in the de-trended electric and magnetic fields and are associated with

Poynting flux dominantly toward the earth along the geomagnetic field, consistent with energy flow from the x-line (Figure 11).

A close-up of the Polar data used to calculate S_z (Figure 12) also shows the coordinated waves in the electric and magnetic fields.

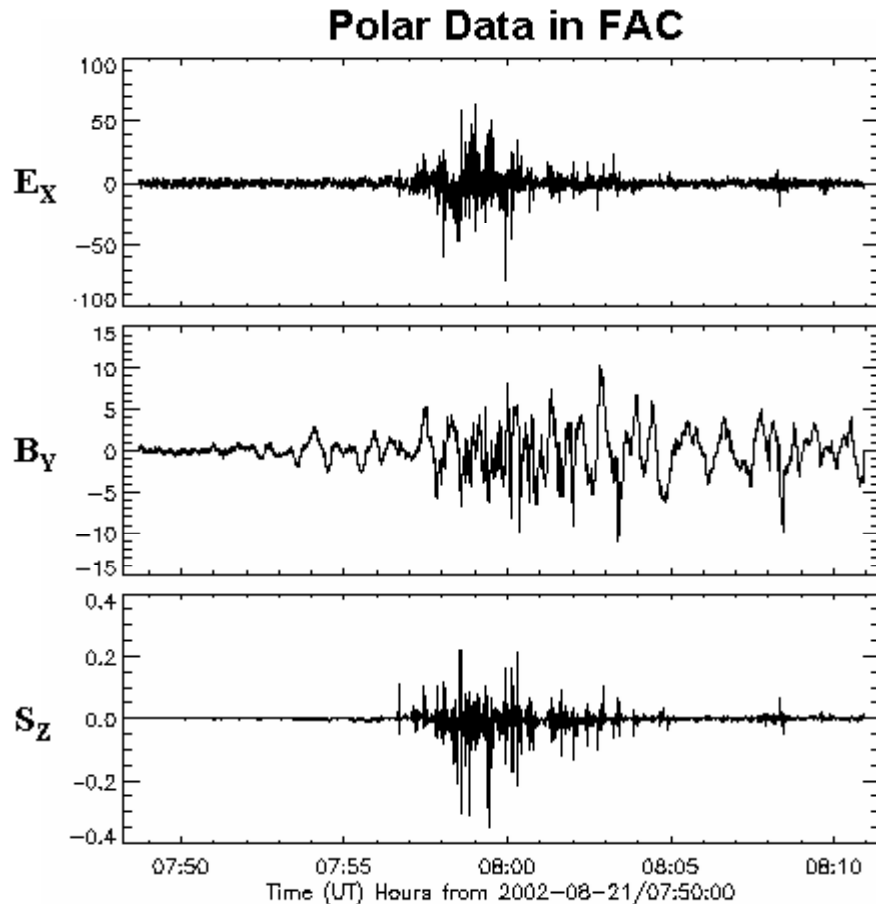
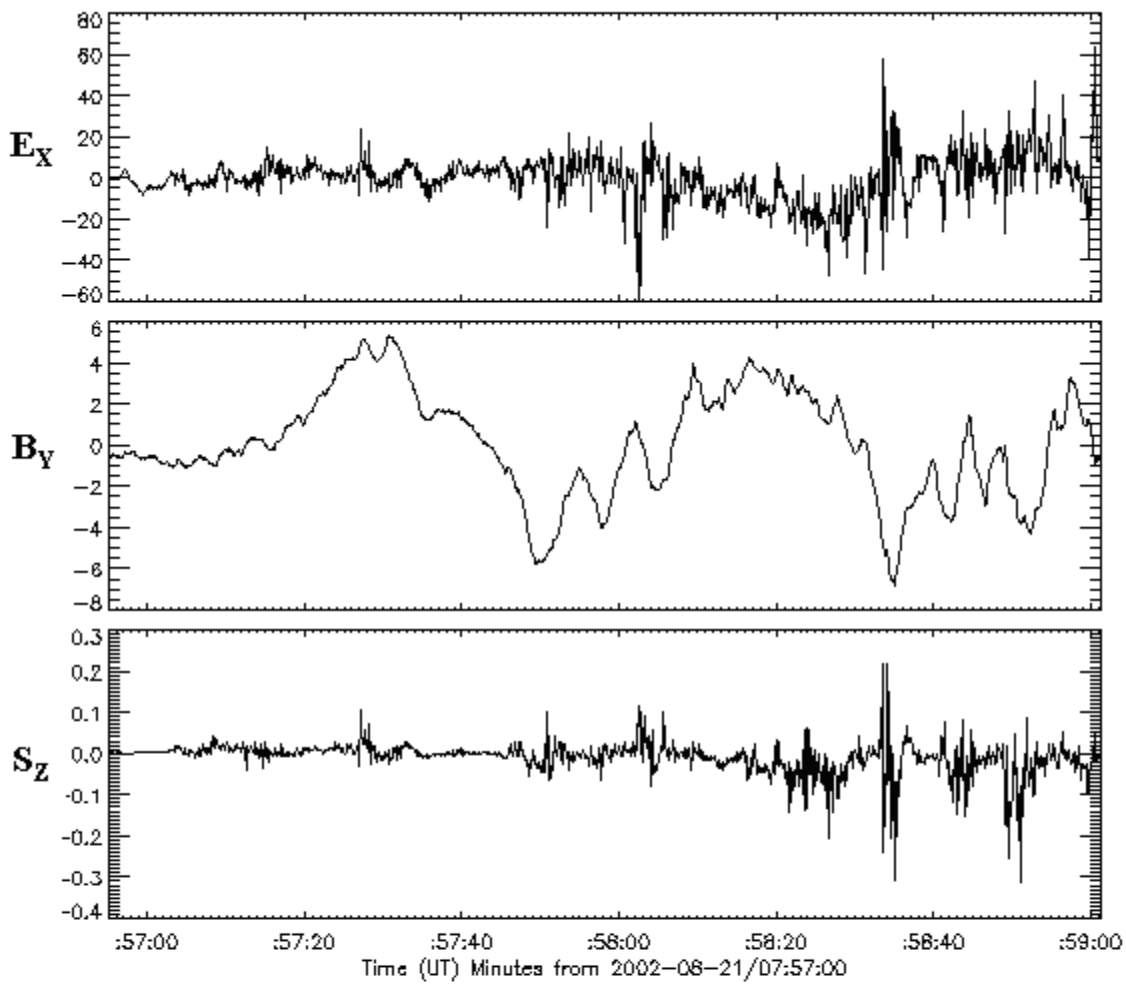


Figure 11. Graph of Poynting flux in the z-direction from Polar data in field-aligned coordinates.

a)

Polar Data in FAC



b)

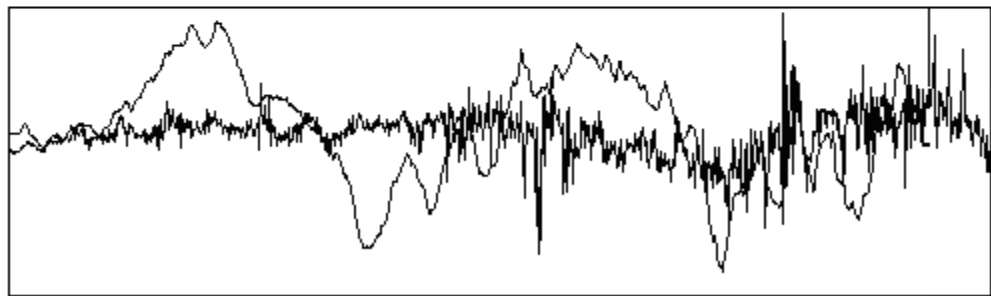


Figure 12. (a) Close-up of Polar data, showing the large amplitude waves. (b) Superimposed electric and magnetic field data, illustrating the correlated E and B .

VIII. Conclusion

Intense changes in the aurora are precipitated by the large energy flow

associated with the onset of reconnection during a substorm. The aurora is relatively quiet until the start of fast ion flows, at which point brightening begins to appear.

At the peak of ion flow, the brightening is at its maximum, and as reconnection ends and the ion flow slowly returns to zero, the aurora returns to its comparatively quiescent state.

Waves associated with Poynting flux were also seen dominantly toward the earth, in agreement with the expected flow of energy from the reconnection x-line. The E/B ratios were comparable to the expected Alfvén speed, indicating that the higher-frequency waves observed may be from Alfvén waves.

Further research would involve comparing the Poynting flux from Cluster and Polar with the energy from the aurora seen by IMAGE.

IX. Acknowledgements

A huge thank you to Cindy Cattell, my advisor, for all of her assistance over the past few weeks. Her help has been greatly appreciated. Thanks also to John Dombeck and the grad students in the space physics lab, who provided both technical support and entertainment. Much gratitude goes to Serge Rudaz, Wendy Tschaapl, and the University of Minnesota for putting together a wonderful REU program, and last but not least, many thanks to the National Science Foundation for helping to fund this research through NSF grant PHY-0139099.

X. References

Akasofu, Syun-Ichi and Louis J. Lanzerotti. The Earth's Magnetosphere. *Physics Today*, Dec 1975.

Balogh, A. et al., The Cluster magnetic field investigation: Overview of in-flight

performance and initial results, *Ann. Geophys.* 19, 1207-1217, 2001.

Burch, J. L., IMAGE Mission Overview, *Space Science Reviews*, IMAGE special issue, **91**, 1-14, January, 2000.

Cowley, Stanley W. H. A Beginner's Guide to the Earth's Magnetosphere. *Earth in Space Vol. 8*. American Geophysical Union, 1996.

Credland, J., G. Mecke and J. Ellwood, The Cluster Mission: ESAOs Spacefleet to the Magnetosphere, *Space Sci. Rev.* 79, 33-64, 1997

Gustafsson, G., Boström, R., Holback, B., Holmgren, G., Lundgren, A., Stasiewicw, K., Åhlén, L., Mozer, F. S., Pankow, D., Harvey, P., Ulrich, R., Pedersen, A., Schmidt, R., Butler, A., Fransen, A. W. C., Klinge, D., Thomsen, M., Fälthammar, C.-G., Lindqvist, P.-A., Christenson, S., Holtet, J., Lybekk, B., Sten, T. A., Tanskanen, P., Lappalainen, K., and Wygant, J: The electric field and wave experiment for the Cluster Mission, *Space Sci. Rev.*, 79, 137-156, 1997.

Harvey, P. et al., The Electric Field Instrument on the Polar Satellite, in *The Global Geospace Mission*, C.T. Russell, ed., p. 583, 1995.

Kivelson, Margaret, and Christopher T. Russell (Eds.). (1995). *Introduction to Space Physics*. Cambridge: Cambridge University Press.

Mende, S. B., et al., Far-Ultraviolet Imaging from the IMAGE Spacecraft. 2. Wideband FUV imaging, *Space Science Reviews*, IMAGE special issue, **91**, 271-285, January, 2000

Oerset, M., et al., In situ detection of

collisionless reconnection in the Earth's magnetotail, *Nature*, **412**, 414, 2001.

Res., **105**, 18,675, 2000.

Paschmann, Götz, Stein Haaland, and Rudolf Treumann (Eds.). (2003). *Auroral Plasma Physics*. Dordrecht, The Netherlands: Kluwer Academic Publishers.

Rème, H., J.M. Bosqued, J.A. Sauvaud, A. Cros, J. Dandouras, C. Aoustin, J. Bouyssou, Th. Camus, J. Cuvilo, C. Martz, J.L. Médale, H. Perrier, D. Romefort, J. Rouzaud, D. d'Uston, E. Möbius, K. Crocker, M. Granoff, L.M. Kistler, M. Popecki, D. Hovestadt, B. Klecker, G. Paschmann, M. Scholer, C.W. Carlson, D.W. Curtis, R.P. Lin, J.P. McFadden, V. Formisano, E. Amata, M.B. Bavassano-Cattaneo, P. Baldetti, G. Bellucci, R. Bruno, G. Chionchio, A. di Lellis, E.G. Shelley, A.G. Ghielmetti, W. Lennartsson, A. Korth, U. Rosenbauer, R. Lundin, S. Olsen, G.K. Parks, M. McCarthy and H. Balsiger, The Cluster Ion Spectrometry (CIS) Experiment, *Space Sci. Rev.* **79**, 303-350, 1997

Russell, C. T., *et al.*, The GGS Polar magnetic fields investigation, *Space Sci. Res.*, **21**, pp. 563-582, 1995

Scudder, J. et al., Hydra- A 3-d electron and ion hot plasma instrument for the Polar spacecraft of the GGS mission, in *The Global Geospace Mission*, C.T. Russell, ed., p. 459, 1995.

Stenbaek-Nielsen, H. C., *et al.* Why Do Auroras Look the Way They Do? American Geophysical Union, 1999.

Wygant, J. R., et al., Polar spacecraft based comparisons of intense electric fields and Poynting flux near and within the plasma sheet-tail lobe boundary to UVI images: An energy source for the aurora, *J. Geophys.*

Spin Ejection Using an External Cavity Tunable Diode Laser in Ferromagnet-Semiconductor Heterostructures

Undergraduate Student

Claire Weiss
Lawrence University
Appleton, WI

Advisor

Professor Paul Crowell
University of Minnesota
Minneapolis, MN

Spin Ejection using an External Cavity Tunable Diode Laser in Ferromagnet-Semiconductor Heterostructures

Claire Weiss
Lawrence University, Appleton, WI

Spin transport is an important area of research in physics because it could lead to a deeper understanding of fundamental processes in physics (such as electron tunneling through a barrier) and because its applications could be useful in creating new types of electronic devices in which both charge and spin could be manipulated. Spin transport of charge carriers across a potential barrier is studied here in several different samples. The samples are all ferromagnet-semiconductor heterostructures. An external cavity tunable diode laser was used to send polarized light into the heterostructures. The current through a quantum well was then measured to study the effectiveness of spin transport of the charge carriers. Although we did not observe spin ejection by these methods, we did observe electro-absorption, Zeeman splitting, and Landau diamagnetism, which indicate that spins were produced in the quantum well and this gives us hope for future spin ejection experiments.

I. Introduction

Spin transport has been an important area of research in condensed matter physics in recent years. Spin transport has been demonstrated in different types of heterostructures, including superconducting-ferromagnet heterostructures, differently doped semiconductor heterostructures, and other materials. The main focus of our research, however, has been to study spin transport in ferromagnet-semiconductor heterostructures.

Ferromagnetic and semiconductor materials are particularly interesting because of their application in electronic devices, such as computers. Ferromagnetic materials are used in computers as a way to store data, while semiconductor materials are useful for data processing. Semiconductors are used to process data because their charge can be “manipulated.” Therefore, if spin transport could be achieved in the ferromagnet-semiconductor heterostructures, one computer chip could both store and process data. These heterostructures could be useful in future electronic applications because the charge and the spin of the charge carriers could be utilized. The study of materials in which charge and spin can be manipulated is commonly referred to as “Spintronics.”

Our main goal is to demonstrate spin transport in various ferromagnet-semiconductor heterostructures. Then, we will explore the dependence of spin transport on different variables, such as different materials, magnetic fields, temperatures, and even experimental methods (such as spin injection and spin ejection). Our ultimate goal in studying spin transport in ferromagnet-semiconductor heterostructures is to gain more knowledge about the feasibility of spintronics by finding the optimal set of conditions for spin transport to take place.

In this paper, we will outline the basic theoretical background needed to understand spin transport. Then, we will go over the sample make-up and preparation. Finally, we will explain the spin ejection experiment and present and explain some of the preliminary data from that experiment.

II. Theoretical background

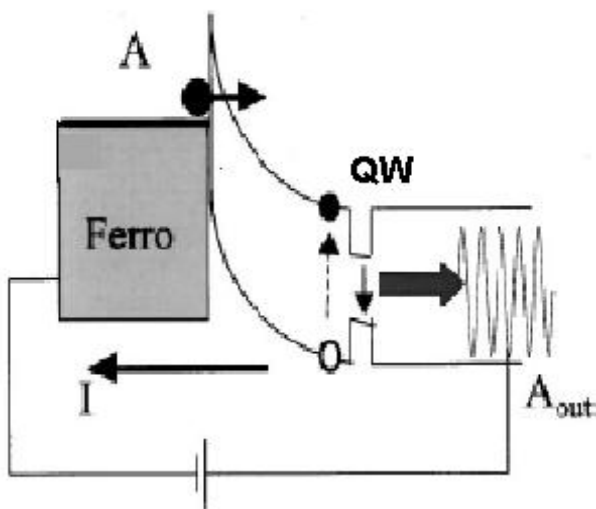


Figure 1 This cartoon [1] illustrates spin injection. We see the bias current through the quantum well, and the circularly polarized emitted light.

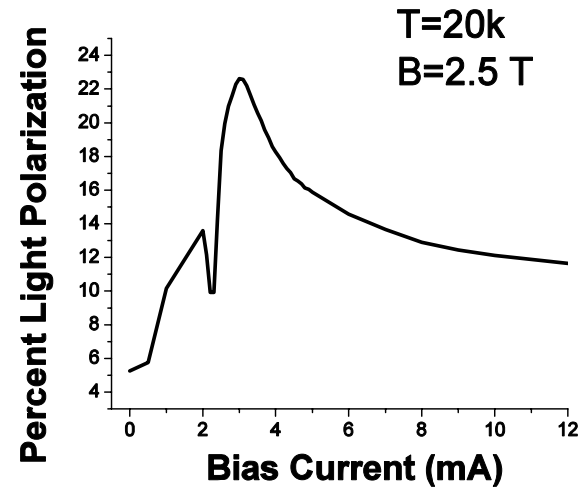


Figure 2 This plot shows the percent polarization of light output as a function of the applied bias current. This data was taken at 2.5T and 20k.

A. Spin Injection:

A few different experiments were performed to study spin transport. First we studied spin injection. Spin injection works by applying a bias current across the quantum well region in between the p and n-type semiconductor materials. This causes spin-polarized electrons to move from the ferromagnet to the semiconductor as seen in Figure 1. These moving electrons recombine with holes in the quantum well region, producing light. Then, the polarization of the light output is studied as a function of several variables, such as magnetic field, temperature, and bias current.

We have shown that spin injection works, with polarizations up to 23 percent, as shown in Fig 2. Now we are curious to see whether this process can work in reverse, and if we can get spin-polarized electrons to move from the semiconductor to the ferromagnet. This “reverse” process of spin injection is called spin ejection.

B. Schottky diodes:

In order to understand spin ejection, one must first understand Schottky photodiodes. The Schottky diode refers to a section of our samples that includes the ferromagnetic electrode, the depletion region of the diode and the semiconductor. The depletion region is formed when free electrons from the n-type material diffuse across the p-n junction, combine with holes, and create ions at the interface. The Schottky barrier refers to a metal contact with a semiconductor. The incident light is converted to

electrons and holes, and the bias voltage across the diode causes the electrons and holes to move in different directions, creating a current.

C. Spin Ejection:

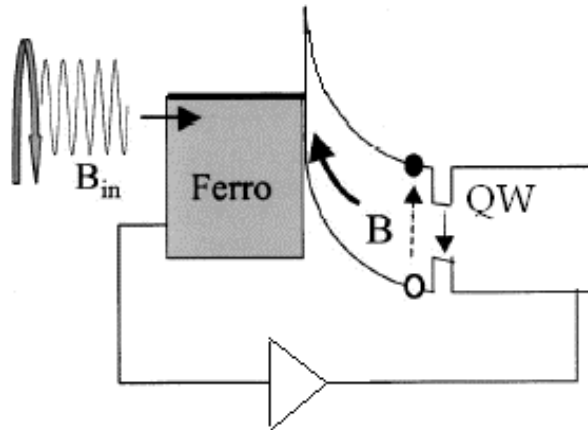
The basic idea behind spin ejection is to send light into the sample, and measure the current output. In this process, spins are first produced in the quantum well region, and then they are detected in the ferromagnetic material after tunneling through the Schottky barrier. Ferromagnetic materials can be used to detect spin-polarized current because the density of states of spin up and spin down electrons are different at the Fermi level. This difference in the density of states causes a difference in the resistance for spin up and spin down tunneling electrons. [2]

Incident light on the sample will create an electron-hole pair. This energy to excite an electron-hole pair is equal to the band-gap energy. Under the influence of an electric field, the spin-polarized electrons and holes will move in opposite directions. The electrons will move towards the electrode, and the holes will move toward the substrate. This movement of charge carriers produces an electric current, which we can measure. With polarized light, the electrons produced will be spin-polarized. This process involves a transfer of angular momentum from the polarized light to the spin-polarized charge carriers. The circularly polarized light that is absorbed produces transitions between the conduction band and other bands, following the quantum mechanical selection rules,

$$\Delta\ell = 1, \quad \Delta m_j = \pm 1, \quad \Delta s = 0, \quad (1)$$

which describe dipole transitions. These selection rules allow for spin-polarized electrons and holes to be created in the quantum well region. [3]

The quantum well is created by putting a semiconductor material in between two other types of semiconductors (n and p-type). The quantum well material has a smaller band gap than the surrounding semiconductor material. The band gap of a material describes the gap between the conduction band and the valence band. For our quantum well, Gallium Arsenide is used because it has a direct band gap. This means that the valence and conduction bands line up in momentum space. This allows the electron and hole to recombine and emit light. The quantum well region between the two types of semiconductor material (p-type and n-type) is used for two purposes. The first purpose is to allow us to know the exact location of the electron-hole creation. (Physically, the quantum well region is very small.) The second purpose of using a quantum well is that the



current to voltage

Figure 3 This cartoon [1] illustrates spin ejection. We see the circularly polarized light coming in and the electrons and holes moving to create current.

energies of charge carriers in a quantum well can be easily found. The energies of a quantum well can be found by solving the Schrödinger equation for a one-dimensional quantum well. The energies are,

$$E = \frac{n^2 \pi^2 \hbar^2}{2ma^2}, \quad (2)$$

where n is the principal quantum number, m is the mass of the particle, and a is the depth of the well. Knowledge of these energies allows us to find the exact wavelength of light needed to excite a charge carrier to these energy levels. These wavelengths can be found by the simple relationship,

$$E = \frac{hc}{\lambda}, \quad (3)$$

where h is Planck's constant, c is the speed of light, and λ is the wavelength of light. Since we now know the exact wavelength of light needed, we can use a tunable laser in order to stimulate the transitions that we are interested in.

III. Samples

A. Semiconductors and Ferromagnets:

Aluminum (to prevent oxidation): 2.5nm
Ferromagnet (Fe): 5nm
n+ -type semiconductor (AlGaAs): 15nm
n/n+ transition layer (AlGaAs):15nm
n-type semiconductor (AlGaAs):100nm
Quantum Well (GaAs): 10nm
p-type semiconductor (AlGaAs): 450nm
Substrate (p-type GaAs)

Figure 4 This figure shows the make-up of sample CA139.

Semiconductors are useful in the world of electronics for two main reasons. The first reason is that in semiconductors, different doping techniques can change the majority carriers (those responsible for the current) from electrons (n-type) to holes (p-type). In a material with both n and p-doped semiconductors (like our samples), the electrons and the holes can both move in order to create a current. The second useful feature of semiconductors is that their band structure is such that it only takes a small amount of energy to move electrons from one state to another. In this way, one can "manipulate" the charge on a semiconductor and this can be used to process data, as discussed earlier.

The ferromagnetic material used in these samples was iron. Iron is particularly useful because it demonstrates the properties of ferromagnetism very well. That is, it has a significant magnetization and a large polarization. The large polarization is due to the difference in spin up and spin down states at the Fermi level as explained previously.

All of our samples were grown using molecular beam epitaxy (MBE) in the material science department at the University of Minnesota. [4] All of the samples are ferromagnet-semiconductor heterostructures. In semiconductor materials, spins have a relatively long lifetime. Spin relaxation occurs when the spin lifetime, τ_s , is too short for the electron and hole to recombine, and in semiconductors that spin lifetime is relatively long. The sample that we focus on in this paper is CA139. CA139 has Iron as the ferromagnet and aluminum gallium arsenide as the semiconductor. The quantum well is made of gallium arsenide, which is also a semiconductor.

However, different combinations of ferromagnetic and semiconductor materials were used to study spin transport. Although the samples consist of many differing layers, most of the samples we examined had iron as the ferromagnetic material. On top of this iron layer, a layer of aluminum was grown in order to prevent oxidation of the iron. The results presented here are from one of the most successful spin injection samples, CA139. One of the most important features of this sample is the n+/n-doped transition layer as shown in Fig. 4. The higher the n-doping (as denoted by n+), the narrower the Schottky tunnel barrier becomes. This transition layer increases tunneling by having this heavily doped section and a regularly n-doped section to ease the transition between it and the two surrounding n-doped layers of semiconductor.

With these samples, we expect to see evidence of spin ejection. We should see the same magnetic field dependence that we saw for spin injection, shown in Fig. 5. We should observe the same S-shaped curve for the normalized absorption versus magnetic field plot. This S-shape corresponds to the polarization,

$$P = \frac{\sigma_+ - \sigma_-}{\sigma_+ + \sigma_-}, \quad (4)$$

which is related to the spins, σ , (up and down) of the ejected electrons.

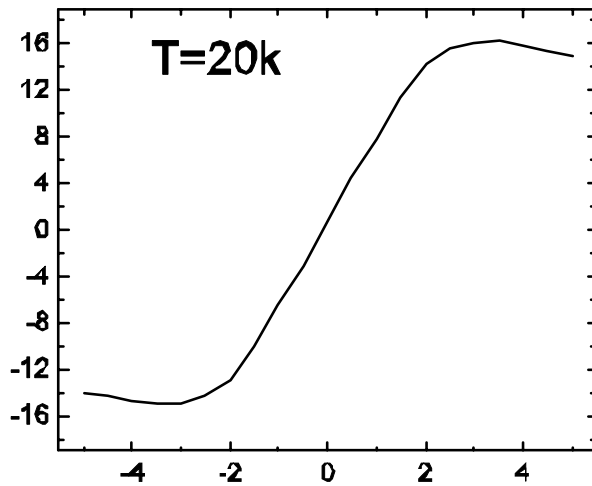


Figure 5 This figure shows the magnetic field dependence from the spin injection data for CA139. We expect to see this S-shape in our magnetic field dependence plot for spin ejection.

IV. Experimental Set-up and data acquisition

Our experimental set-up is shown in Fig. 6. In the optical set-up, a chopper wheel was used in front of the laser in order to modulate the intensity of the laser light, and a linear polarizer and photo-elastic multiplier (PEM) were used together to change the polarization of light incident on the sample. The linear polarizer was necessary in order to linearly polarize the light as it entered the PEM. The PEM consists of piezo-electric

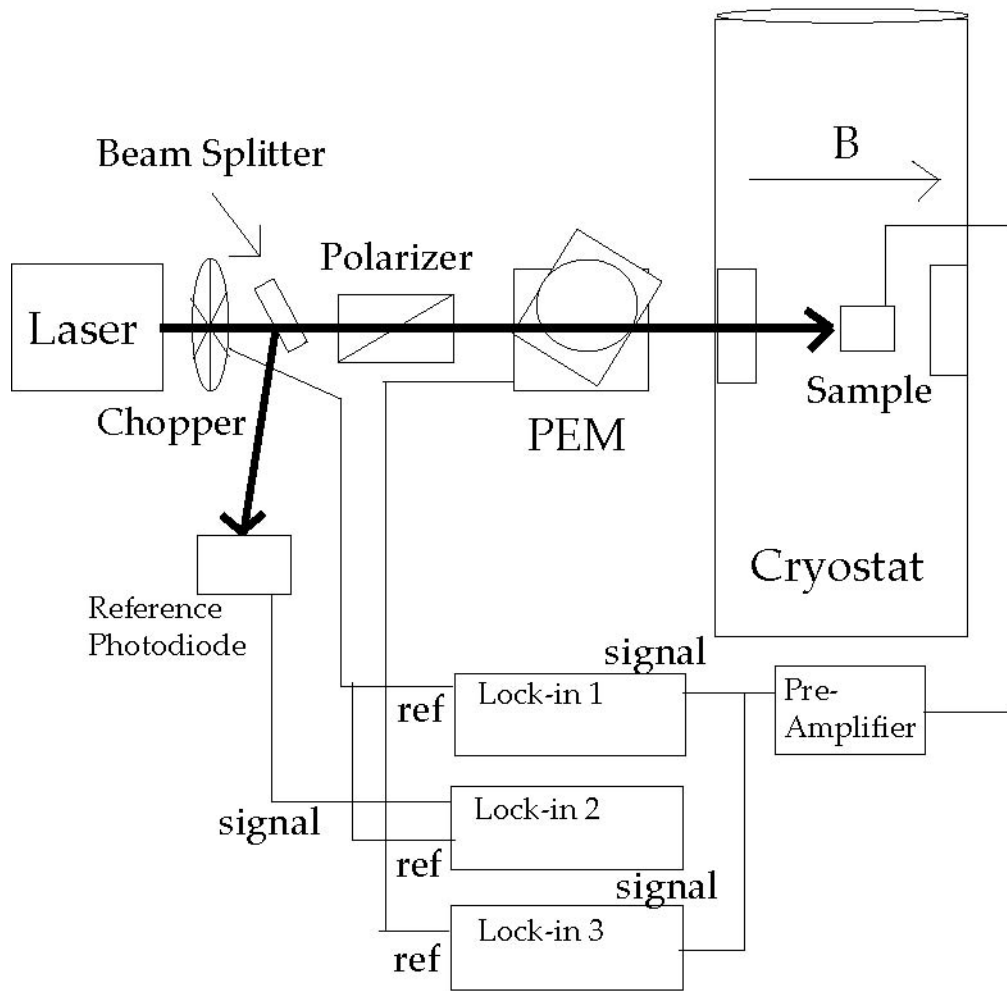


Figure 6 This schematic diagram shows both the optical and electrical elements of the experimental set-up. The laser light is shown in bold arrow. We have the basic optical elements as well as three lock-in amplifiers, which each have a reference and signal input.

elements, which modulate the output light between right and left-hand circularly polarized light. By using the PEM, we were able to measure the circular dichroism, which is how the absorption of light changes with the modulation of the circular polarization of light.

We measure the absorption in two ways. We measure both the total absorption and the spin-dependent absorption. To do this, we need three lock-in amplifiers. The total absorption is found by dividing the photocurrent (as measured with the photodiode lock-in) by the laser intensity (as measured with the chopper lock-in). The spin-dependent absorption is found by dividing the PEM signal by the photocurrent. This will give us Eq. 4.

Our samples are placed in the magneto-optical cryostat (Oxford Instruments). The cryostat contains a split-coil superconducting magnet as well as liquid helium and liquid nitrogen baths separated by vacuum chambers. By adjusting the flow of the liquid helium and the pumping power on the sample space, we were able to vary the

temperature inside the cryostat. By changing the current in the superconducting magnet, we are able to take measurements at different magnetic fields.

A magnetic field is used to align the spins of the electrons in the ferromagnet with the incident light. Faraday geometry refers to when the magnetic field is parallel to the incident light. Since the saturation magnetic field for Iron is about 2T, the field sweeps performed will scan well above 2T, to a maximum value of 5 or 6T. The application of a magnetic field also produces other effects. The energy levels in the quantum well will be split due to the Zeeman effect. The Zeeman effect causes splits in the energy level of the size

$$\Delta E = \mu_B B g m_j, \quad (5)$$

where μ_B is the Bohr magneton, B is the applied magnetic , g is the Landé g-factor, and m_j is the magnetic quantum number corresponding to the total angular momentum. We will also observe Landau diamagnetism. In this effect, the energy levels of the quantum well are not split, but instead they are shifted upward. The electrons can all be thought of using quantum mechanics as lying in the same plane, and the applied magnetic field is perpendicular to this plane. This orientation causes cyclotron motion, which can be described by,

$$\frac{mv^2}{r} = qvB, \quad (6)$$

where the left side is the centripetal force and the right side is the force caused by the magnetic field. From this equation, we see that an increase in the magnetic field, B, cause a decrease in the radius of orbit, r. This process causes a change in energy, and therefore a change in wavelength.

A. Tunable Diode Lasers:

A diode laser, like our samples, consists of many layers. The diode laser has p and n-type electrodes on the outside, with two cladding layers (again p and n-type) surrounding the “active region.” An injection current is sent through this active region in order to create a series of electrons and holes. These electrons and holes recombine, creating light that becomes the laser light.

A tunable diode laser is used in the spin ejection experiment so that we can tune to a specific wavelength corresponding to the quantum well energy transitions. We used an external cavity tunable diode laser built by Ben Pearson, UMN '06. This set-up consists of a commercially purchased diode laser (Thorlabs, L808P200) and mount pieces, which were built by Pearson. [5] Our tunable laser works by creating an external laser cavity between the reflective backing of the laser diode and the diffraction grating. The diffraction grating is used in order to send the first-order reflection of the light back into the laser. As the grating is rotated, a different wavelength of light is sent back into the laser. This feedback wavelength becomes the lasing wavelength. Therefore, our tunability is achieved through the rotation of a diffraction grating.

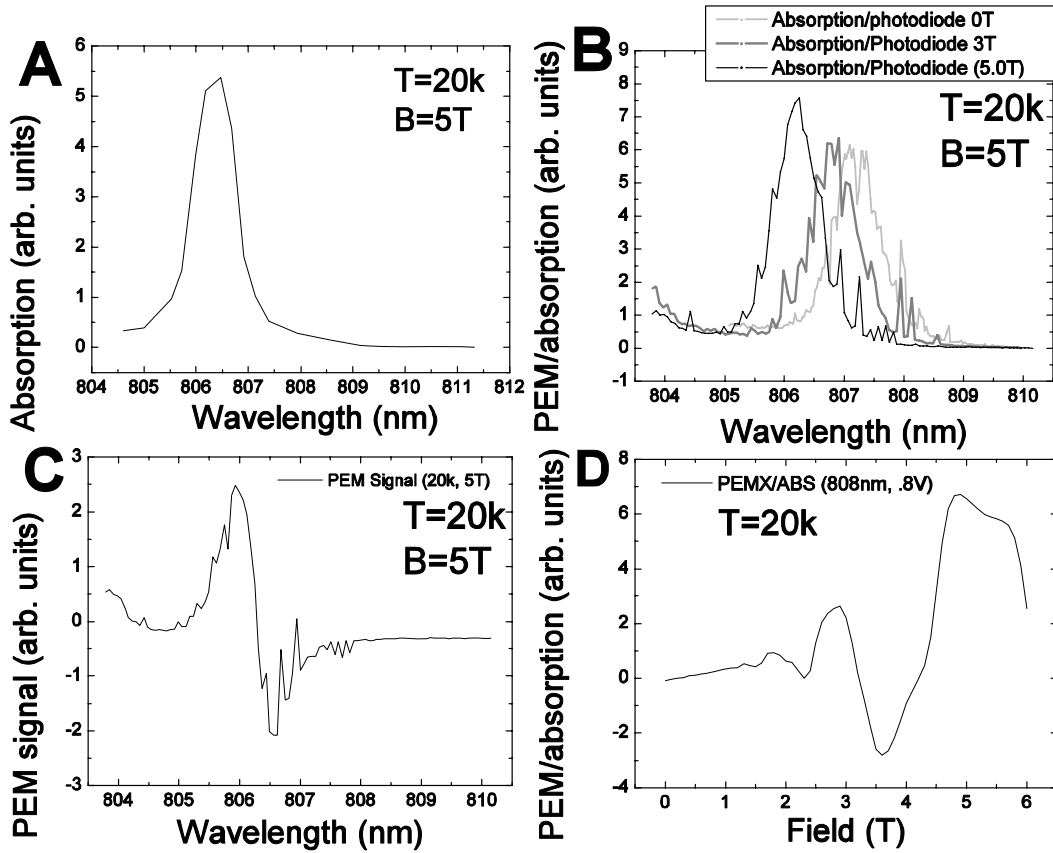


Figure 7 (A-D) These plots show the data from CA139. In the 6A, we see the absorption curve. The 6B and 6C plots show the Landau diamagnetism and the Zeeman effect. Figure 6D shows the spin ejection plot, but the characteristic S-shape field dependence that we observed in spin injection is not present.

V. Data & Discussion

Spin ejection data for sample CA-139 is given in Fig. 7, A-D. In Fig. 7A, we see that there is a peak of the absorption at a specific wavelength. This wavelength corresponds to a specific energy. Since we see the maximum electro-absorption at this energy, we know that the wavelength of our laser was tuned correctly to one of the quantum well energy transitions.

We can also see Landau diamagnetism and the Zeeman effect in Fig. 7B and Fig. 7C, respectively. In Fig. 7B, the wavelength decreases as the magnetic field is increased. This change in wavelength corresponds to a change in energy due to the applied magnetic field. Recall that this change in energy is due to the changing cyclotron motion of the electrons about the magnetic field. Fig. 7C shows evidence for the Zeeman effect. As the quantum well energies split with an applied magnetic field, each new energy level with either accept left or right-hand circularly polarized light. The concave up peak corresponds to one of the polarizations being absorbed and the concave down peak corresponds to absorption of the other. Qualitatively, the combination of the Zeeman effect and Landau diamagnetism correspond to the quantum well energies shifting up (Landau) and splitting (Zeeman). Note that these effects are due to the applied magnetic field, and they are not evidence for spin ejection. These effects do help show us,

however, that spin-polarized electrons are being created in the quantum well. We can tell this since we see both absorption (Fig. 7A) and spin-dependent absorption of light (Fig. 7C).

Although our data shows electro-absorption in the quantum well and Landau diamagnetism and the Zeeman effect, we did not observe the characteristic S-shaped curve in the normalized absorption versus magnetic field plot. Since we did not observe this characteristic field dependence, no spin ejection occurred in this sample. There are many reasons that may explain why we did not observe the characteristic polarization of spin ejection. First of all, the electron spin may be relaxing as it tunnels into the ferromagnetic material. The spin relaxation depends on the tunneling material, so if this is the problem, spin ejection may still be achieved with other ferromagnetic materials. Another possible reason for not observing spin ejection could be that the holes (and not the electrons) are dominating the current. We expect the applied voltage across the diode to cause both electrons and holes to move. However, since holes have a very short spin lifetime, a hole-dominated current would not be spin-polarized.

Recent research performed in Paul Crowell's lab suggests that spin ejection should be possible. Experiments that were set up similar to this one have demonstrated photoluminescence polarization, which is in some ways similar to spin ejection. As stated earlier, one problem may be the materials used in the sample. Our method was to find the best sample for demonstrating spin injection and then try to use it for spin ejection. However, although spin ejection can be thought of as reverse-spin injection, it is not quite that simple. Perhaps the best sample for spin ejection will be a sample that showed very little polarization in the spin injection experiment.

VI. Acknowledgements

I would like to thank my advisor, Paul Crowell, for giving me the opportunity to work in his lab. I would also like to thank everyone who works in Paul Crowell's lab, and especially Mike Erickson. I would like to thank Ben Pearson for building the external cavity tunable diode laser, and Chris Palmstrøm's group for helping prepare the samples. I would like to thank the staff of the University of Minnesota Department of Physics, especially Serge Rudaz and Wendy Tschaapl for their help with the REU program. Finally, I would like to thank the National Science Foundation who made this project possible through funding under grant number NSF/PHY-0139099.

VII. References

- [1] Isakovic, et al. *Journal of Applied Physics*, **91**, 7261 (2002).
- [2] Isakovic, Abdel. *Spin Transport in Ferromagnet-Semiconductor Heterostructures, Graduate Thesis*. University of Minnesota School of Physics and Astronomy, 2003.
- [3] Davies, John H. *The Physics of Low-Dimensional Semiconductors An Introduction*, Cambridge University Press, 1998.

[4] C. Adelmann, X. Lou, J. Strand, C. J. Palmstrøm, and P. A. Crowell, *Phys. Rev. B* **71** 121301 (2005).

[5] Pearson, Benjamin Thomas. *Design and Construction of an External Cavity Diode Laser and Saturated Spectroscopy, Undergraduate Senior Thesis*. University of Minnesota School of Physics and Astronomy, 2006.